

---


Electronic Theses and Dissertations, 2004-2019

---

2013

## Mesoscale Light-matter Interactions

Kyle Douglass  
*University of Central Florida*

 Part of the [Electromagnetics and Photonics Commons](#), and the [Optics Commons](#)  
Find similar works at: <https://stars.library.ucf.edu/etd>  
University of Central Florida Libraries <http://library.ucf.edu>

This Doctoral Dissertation (Open Access) is brought to you for free and open access by STARS. It has been accepted for inclusion in Electronic Theses and Dissertations, 2004-2019 by an authorized administrator of STARS. For more information, please contact [STARS@ucf.edu](mailto:STARS@ucf.edu).

---

### STARS Citation

Douglass, Kyle, "Mesoscale Light-matter Interactions" (2013). *Electronic Theses and Dissertations, 2004-2019*. 2863.  
<https://stars.library.ucf.edu/etd/2863>



# MESOSCALE LIGHT-MATTER INTERACTIONS

by

KYLE M. DOUGLASS

B.S. Rose-Hulman Institute of Technology, 2007

M.S. University of Central Florida, 2011

A dissertation submitted in partial fulfillment of the requirements  
for the degree of Doctor of Philosophy  
in CREOL, the College of Optics & Photonics  
at the University of Central Florida  
Orlando, Florida

Fall Term  
2013

Major Professor: Aristide Dogariu

© 2013 Kyle M. Douglass

## ABSTRACT

Mesoscale optical phenomena occur when light interacts with a number of different types of materials, such as biological and chemical systems and fabricated nanostructures. As a framework, mesoscale optics unifies the interpretations of the interaction of light with complex media when the outcome depends significantly upon the scale of the interaction. Most importantly, it guides the process of designing an optical sensing technique by focusing on the nature and amount of information that can be extracted from a measurement.

Different aspects of mesoscale optics are addressed in this dissertation which led to the solution of a number of problems in complex media. Dynamical and structural information from complex fluids—such as colloidal suspensions and biological fluids—was obtained by controlling the size of the interaction volume with low coherence interferometry. With this information, material properties such as particle sizes, optical transport coefficients, and viscoelastic characteristics of polymer solutions and blood were determined in natural, realistic conditions that are inaccessible to conventional techniques.

The same framework also enabled the development of new, scale-dependent models for several important physical and biological systems. These models were then used to explain the results of some unique measurements. For example, the transport of light in disordered photonic lattices was interpreted as a scale-dependent, diffusive process to explain the anomalous behavior of photon path length distributions through these complex structures. In addition, it was demonstrated how specialized optical measurements and models at the mesoscale enable solutions to fundamental problems in cell biology. Specifically, it was found for the first time that the nature of cell motility changes markedly with the curvature of the substrate that the cells

move on. This particular work addresses increasingly important questions concerning the nature of cellular responses to external forces and the mechanical properties of their local environment.

Besides sensing of properties and modeling behaviors of complex systems, mesoscale optics encompasses the control of material systems as a result of the light-matter interaction. Specific modifications to a material's structure can occur due to not only an exchange of energy between radiation and a material, but also due to a transfer of momentum. Based on the mechanical action of multiply scattered light on colloidal particles, an optically-controlled active medium that did not require specially tailored particles was demonstrated for the first time. The coupling between the particles and the random electromagnetic field affords new possibilities for controlling mesoscale systems and observing nonequilibrium thermodynamic phenomena.

*To the memory of my mother, who was—and continues to be—my biggest supporter, and  
to my wife Kirsten, whose energy and enthusiasm keeps me smiling.*

## **ACKNOWLEDGMENTS**

The completion of this work would not have been possible without the support of many different people. First and foremost I have my family to thank because they encouraged me to pursue my interests in school, no matter what they may have been. It was easy for my parents and grandparents to see that math and science were the subjects I was most interested in. They were kind enough to nurture this interest with gifts of books about space and physics and by taking me on many memorable trips to museums as a child, like the Kennedy Space Center. My mother especially helped to set me upon the path of becoming a scientist because it was her that first suggested that I study engineering in college. For this I am forever grateful to her for helping me find one of the greatest joys in my life.

The teachers at Edon High School and the faculty at Rose-Hulman also played important roles in my development as a young scientist because of their dedication to education. Though I am thankful to many educators, a few who I should mention by name because of the significance of the impact they have had on me include: Mr. Mark Blue, Mrs. Annette Peckham, Mrs. Robin Spangler, Mrs. Patty Curry, Dr. Mark Minster, Dr. Mike Moloney, Dr. Robert Bunch, and Dr. Sergio Granieri.

Dr. Aristide Dogariu has been the most important educator to me, both as an advisor and as a friend. No one individual has taught me the value of critical thinking and scientific reasoning better than he has. He understands the value of educating young scientists and has worked tirelessly over the last six years to ensure that I and the rest of his students graduate with the best possible abilities in scientific understanding that we can possess.

I have so many friends to thank that I cannot possibly mention them all here. My time at Rose-Hulman and at CREOL have led me to many wonderful, interesting, and genuinely good people who have all had some degree of influence over my development as a professional scientist. Matt Weed, Andrew Stroh, Woli Urbe, and Nick Switzer are just a few individuals with whom I have had conversations that I will always remember fondly.



## TABLE OF CONTENTS

LIST OF FIGURES .....	xi
LIST OF TABLES .....	xvii
LIST OF ABBREVIATIONS .....	xviii
CHAPTER 1: ELEMENTS OF OPTICS AT THE MESOSCALE .....	1
Defining Mesoscale Optics.....	1
Three Aspects of Mesoscale Optics .....	7
Why Study Mesoscale Optics? .....	13
Organization of Work .....	14
CHAPTER 2: OPTICAL SENSING IN MESOSCOPIC SYSTEMS .....	16
Low Coherence Interferometry for Probing Multiply Scattering Media .....	16
Measuring Photon Diffusion Coefficients Independently of Boundary Conditions .....	22
Low Coherence Dynamic Light Scattering.....	32
Conclusion .....	47
CHAPTER 3: MODELS FOR MESOSCOPIC OPTICS .....	49
Determining Anisotropic Cell Motility on Curved Substrates .....	49
Anomalous Transport of Light in Partially Disordered Photonic Crystals .....	60
Image Reconstruction by Polarization Multiplexing .....	67
CHAPTER 4: CONTROLLING MESOSCALE SYSTEMS WITH LIGHT .....	74

Optically Controlled Active Media .....	74
Dipole-dipole Interactions in Random Electromagnetic Fields .....	81
CHAPTER 5: CONCLUSIONS AND OUTLOOK.....	93
A Summary of the Past and Present.....	93
APPENDIX A: FUNDAMENTALS OF DYNAMIC LIGHT SCATTERING .....	98
Useful Quantities in Dynamic Light Scattering .....	99
The Siegert Relation .....	101
Derivation of the LC-DLS Autocorrelation Functions .....	103
On the Use of Multimode Fibers for Heterodyne Measurements .....	106
DLS Measurements of Non-ergodic Materials .....	114
APPENDIX B: TRACER PARTICLE MICRORHEOLOGY USING DYNAMIC LIGHT SCATTERING.....	115
Measuring the Viscoelasticity of Complex Fluids.....	116
APPENDIX C: DIFFERENCE IMAGING AND VARIANCE-TIME PLOTS.....	124
Determining a Preferred Direction of Motion using Difference Imaging .....	125
APPENDIX D: DETERMINATION OF A DISORDERED PHOTONIC CRYSTAL'S DENSITY OF STATES.....	134
The Density of States for Ordered and Disordered Photonic Crystals .....	135
The Brillouin-Zone Representation of an FCC Lattice .....	135

APPENDIX E: THEORY OF DEGENERATE IMAGE MIXING AND SPARSE RECONSTRUCTION .....	141
Theory of Degenerate Image Mixing .....	142
APPENDIX F: OPTICALLY-CONTROLLED ACTIVE MEDIA.....	147
Realizing an Optically-Controlled Active Medium.....	148
Diffusion of Particles in a 3D Speckle: Analytics .....	150
Diffusion of Particles in a 3D Speckle: Numerics .....	153
Generating a Spatiotemporal Volume Speckle Field .....	155
APPENDIX G: DERIVATION OF THE DIPOLE INTERACTION FORCE .....	161
LIST OF PUBLICATIONS .....	165
LIST OF PRESENTATIONS.....	166
LIST OF REFERENCES .....	168

## LIST OF FIGURES

<b>Figure 1</b> A mesoscale system probed by some incident radiation. The number of components (black dots) within the volume of the light-matter interaction (encircled by the dotted line) and the coupling between the components of this system (represented by springs joining the particles) determines the nature of the scattered and re-emitted light. ....	5
<b>Figure 2</b> The three aspects of mesoscale optics. All three involve the exploration of a mesoscopic system with optical parameters given by a dielectric permittivity, $\epsilon$ .....	15
<b>Figure 3</b> A basic LCI setup. Light from the broadband source is split along two paths, one leading to the medium under investigation and another to a reference mirror that moves along the optical axis. Light reflected from the medium and the mirror (represented by the dashed lines) travels to the detector. ....	17
<b>Figure 4</b> A multiply scattering medium possesses many possible path lengths for a photon to take, each having a length $s_j$ . Three possible paths of differing lengths are illustrated. Conceptually, each path may be thought of as a partially reflecting mirror with reflectivity proportional to the probability of a photon traveling that distance inside the material. The distance of the mirror from some reference point is twice the distance of the corresponding path length. ....	21
<b>Figure 5</b> The diffuse intensity goes to zero at a distance $z_b$ outside of the scattering medium. This distance is known as the extrapolation length and is determined by $\ell^*$ , the refractive indexes of the two media, and the scattering anisotropy of the scatterers. ....	23
<b>Figure 6</b> A bistatic OPS setup for measuring photon path length distributions from a multiply scattering sample. The light is both injected and detected from two fibers situated directly above the sample. The inset displays the envelope of the interferogram. The outside curves are the monostatic path length distributions and the middle curve is the bistatic distribution. ....	25
<b>Figure 7</b> Measured bistatic path length distributions at different fiber separations from a colloidal suspension of 0.43 $\mu\text{m}$ diameter polystyrene spheres at 10% concentration by weight. ....	29
<b>Figure 8</b> Calculated values of the diffusion coefficient from the measurements. Path length is in units of $\ell^*$ . ....	31
<b>Figure 9</b> Average diffusion coefficients extracted from the bistatic OPS setup. Samples A, B, and C are colloidal suspensions of polystyrene spheres at 10% weight concentration and diameter 0.43 $\mu\text{m}$ , 10% and 0.33 $\mu\text{m}$ , and 5% and 0.43 $\mu\text{m}$ , respectively. A', B', and C' are the same samples with oil added on top of the suspensions. The error bars represent one standard deviation of the distribution of the values for $D$ calculated for various permutations of values from $(s, \rho)$ . ....	32

**Figure 10** The low coherence dynamic light scattering (LC-DLS) setup. Broadband light from a super luminescent light emitting diode (SLED) is injected into a fiber splitter and illuminates the sample. Backscattered light is collected by the same fiber and guided to the detector. The detector's photocurrent is digitized by a data acquisition device (DAQ) or the power spectrum is directly calculated with a spectrum analyzer. **Inset** The interaction volume probed by the light at the tip of the fiber. The longitudinal extent of the volume is determined by the coherence length of the light,  $\ell_c$ , and the transverse extent is determined by the field's mode diameter,  $d_{mode}$ . .....33

**Figure 11** Power spectral density of the intensity fluctuations from a suspension of 1  $\mu\text{m}$  diameter polystyrene spheres at different weight concentrations. The curves are characterized by an asymptotic log-log slope of -2 and a corner frequency that depends on their size. ....40

**Figure 12** Power spectral density of intensity fluctuations measured with LC-DLS from viscoelastic media. The sample is a suspension of 0.098  $\mu\text{m}$  diameter polystyrene microspheres in 100,000 molecular weight PEO solutions at 1.0% wt. concentration. The asymptotic log-log slope of the PSD is greater than -2, which indicates that the power law exponent for the particles' MSD is less than one. Compare this to the figure from reference [86]. .....41

**Figure 13** PSD of the backscattered intensity fluctuations from a 10% Pluronic L64 solution in water seeded with 1% wt., 1.0  $\mu\text{m}$  diameter polystyrene spheres. The curves represent data taken at the noted temperatures. **Inset** PSD's from suspensions of 1.0  $\mu\text{m}$  diameter polystyrene spheres in water at 1%, 5%, and 10% weight concentrations are provided as a reference. The PSD for this simple colloid is a Lorentzian whose shape is independent of temperature. ....43

**Figure 14** Analysis of the Pluronic data. a) At 25°C, 10% Pluronic L64 in water contains signatures of bulk polymer with a hydrodynamic radius of 0.13  $\mu\text{m}$ . b) At larger temperatures, the PSD experiences an initial slow decay, followed by a fast rolloff. The slope of the PSD suggests a mean squared displacement that grows with time exponent of 2.5. Since this is not physical for freely diffusing particles, some other mechanism must be causing this behavior. ....44

**Figure 15** Blood viscoelasticity vs. the activated clotting time (ACT). There is a correlation between the ACT, which is the average time it takes for an induced blood clot to form, and the viscoelastic response measured by the instrument. The loss tangent is the ratio of the imaginary part of the viscoelastic modulus to the real part. ....46

**Figure 16** Primary rat Schwann cells move on a quartz fiber. The image was taken with a phase contrast microscope. The microscope's limited depth of field and the cells' poor contrast prevents the use of single-cell tracking algorithms for extracting the statistical information about their motion. Scale bar: 100  $\mu\text{m}$ . ....51

**Figure 17** Pictorial description of the processing steps for determining preferred direction of motion. Top row: a series of images containing moving cells (yellow dots) is captured from the microscope. Middle row: successive images are subtracted from one another. Changes between the images are encoded onto the intensity values of the pixels (here marked by different colors).

Bottom row: the variance of the intensities along a row and column is determined. The behavior of this variance in time reveals characteristics about the motion of the cells. ....52

**Figure 18** Evolution of the variance for simulated cells calculated across rows (top) and columns (bottom). At each time step, simulated cells could move randomly in the x-direction with step sizes drawn from a Gaussian probability distribution function with a standard deviation of 5 pixels. In the y-direction, the step sizes were also Gaussian but with a standard deviation of 1 pixel. Because the cells move greater distances (and are more likely to move) in the x-direction, the features in the top graph, known as a variance vs. time (VT) plot, are different than the bottom one. Quantifying the differences between the two plots leads to determining the anisotropy of the motion. ....54

**Figure 19** The path length distribution of light as measured by OPS from a multiply scattering medium. Different path lengths in the signal correspond to different volumes for the light-matter interaction. ....62

**Figure 20** Light diffusing in a disordered material. In reflection, the interaction volume is equivalent to the volume that an infinitesimally short pulse of light has spread to in a finite time, which is related to the mean squared displacement of the light. Cutoff and absorption length scales,  $\xi$  and  $L_a$ , for the diffusion process exist. When the volume occupied by the energy reaches these scales, the diffusion process reverts from an anomalous one to a normal one.....64

**Figure 21** Path length distributions from the partially disordered photonic crystal at the two wavelengths indicated. The -2 log-log slope is explained by the scaling theory of localization and indicates an anomalous transport of light at  $\lambda = 1550$  nm. ....65

**Figure 22** The calculated density of states for the disordered photonic crystal. The slight depression at 1550 nm is the pseudogap responsible for the renormalization of the diffusion coefficient. ....67

**Figure 23** The polarization multiplexing/demultiplexing scheme.  $N$  images from a scene are encoded onto a single polarization state and overlapped onto an analyzer. The  $M \leq 4$  resulting mixed images are recorded by a CCD camera. A reconstruction algorithm then reproduces the  $N$  original images by applying some appropriate *a priori* information about the scenes.....69

**Figure 24** The 3x4 polarization multiplexing/demultiplexing setup. Four separate input images are encoded onto different linear polarization states (P) and then overlapped at the CCD. An analyzer (A) performs the three Stokes measurements.....70

**Figure 25** a) The original scenes of four distinct shapes obtained by blocking all but one arm of the setup in Figure 24. b) The three Stokes measurements showing the overlapped shapes. These measurements were performed with the analyzer set to 0, 45, and 90 degrees. c) The reconstructed scenes, demonstrating that each shape has been localized to its original direction. ....71

<b>Figure 26</b> a) Original, b) mixed, and c) reconstructed images of complex scenes using the polarization multiplexing/demultiplexing setup. ....	73
<b>Figure 27</b> The particles in a multiply scattering medium are subject to a three-dimensional speckle field. A mean field approximation to this situation is to analyze a single particle in a thermal bath at temperature $T$ and subject to a number of plane waves with random $k$ -vectors and phases that vary with time. ....	75
<b>Figure 28</b> (a) Theoretical power spectral densities (PSD) of the intensity fluctuations of scattered light from suspended particles. The asymptotic log-log slope is related to the power law exponent of the particles' mean squared displacement, $\alpha$ . (b) Measured intensity PSD's from a 0.9% wt., 3.7 $\mu\text{m}$ diameter suspension of polystyrene spheres in water. The decreasing log-log slope with incident laser power is indicative of the particles becoming increasingly superdiffusive. ....	77
<b>Figure 29</b> (a) Numerically calculated mean squared displacement of a polystyrene sphere of radius 1.85 microns in the mean field approximation. The sphere undergoes Brownian motion for short times and gradually becomes superdiffusive at longer times. The log-log slopes of the dashed lines are the average log-log slope of the curves over the displayed range of frequencies. (b) Calculated intensity PSD's from the MSD's in (a). The log-log slope of the PSD's decreases with the increasing RMS field magnitude in the simulated cavity. ....	80
<b>Figure 30</b> The optical binding force for two different directions of plane wave illumination relative to the line joining the dipoles. ....	84
<b>Figure 31</b> The geometry for determining the dipole interaction force in spatially inhomogeneous fields. (a) Two dipoles are situated on the $x$ -axis, one at the origin and one at a distance $R$ from the origin. (b) One realization of the Gaussian field is constructed by a superposition of plane waves whose directions are given by the coordinates on the full Ewald sphere. Each plane wave has a phase that is randomly and uniformly distributed between 0 and $2\pi$ . ....	86
<b>Figure 32</b> The dipole interaction force between particles in a Gaussian random field. The force is long-ranged and oscillatory with a period of about half the illumination wavelength. ....	89
<b>Figure 33</b> The pair interaction force for other types of spatially random fields. Each curve corresponds to dipoles in fields whose Ewald spheres are partially covered with two diametrically-opposed, circularly-symmetric patches with the given half angular width. The curves are normalized to their first data points. ....	90
<b>Figure 34</b> Pair interaction force between dipoles illuminated by randomly polarized plane waves traveling predominately longitudinal (0 degrees), around 45 degrees, and transverse (90 degrees) to the line joining the dipoles. ....	91
<b>Figure 35</b> The relationships between the measured quantity in a DLS experiment and material properties. ....	100

<b>Figure 36</b> Retrieval of the field ACF from an unnormalized intensity ACF using the Siegert relation. (a) The measured curve is first divided by the baseline. Then, 1 is subtracted from this curve to produce the field ACF. (b) The value of the field ACF at zero time-lag is the contrast, $\beta$ . .....	103
<b>Figure 37</b> The contrast in intensity fluctuations, $\beta$ , as a function of the number of independent speckles or modes incident on the detector. ....	108
<b>Figure 38</b> A heterodyne setup employing a multi-mode fiber (MMF). The source beam is split into two directions by a beam splitter (BS). One portion of the beam illuminates the sample. The scattered light from the sample is collected by a lens (L) and focused into a MMF. The other portion of the beam serves as the reference and is also focused into a MMF where it is mixed with the light from the sample before being detected.....	110
<b>Figure 39</b> A piece of material undergoes a shear stress $F(\omega)$ , which causes a strain, or change in length of $\Delta L_0$ . ....	117
<b>Figure 40</b> Viscoelastic moduli calculated for a 4% solution of 100,000 molecular weight PEO in water. The low frequency scaling is denoted by the dashed lines and is expected from theory. ....	121
<b>Figure 41</b> A plot describing for what frequencies and masses inertia may be ignored in a suspension of polystyrene spheres in water. The shaded region denotes the combinations of radius and frequency for which the inertial term in the expression for the mean-squared displacement may not be neglected for precise modeling.....	123
<b>Figure 42</b> This picture represents the calculation of the variance for each row of a single difference image. The value of the variance for each row is placed into a single pixel and these pixels are stacked to form a single column matrix for the particular time t. ....	126
<b>Figure 43</b> VT plots calculated across the rows (top) and columns (bottom) of a difference image. The time of the latest image used to calculate a particular difference image is marked along the x-axis. The persistence of features along the x-axis in the VT plots for the rows indicates a preference for the cells to move in this direction. ....	127
<b>Figure 44</b> Horizontal autocorrelations of the VT maps along the a) rows and b) columns.....	128
<b>Figure 45</b> Decay time of the autocorrelations of the VT plots vs. fiber radius. “x-direction” refers to the autocorrelation of the VT plots of the rows and “y-direction” to the VT maps of the columns. The overlapping data points at a fiber radius of 63 $\mu\text{m}$ indicate that the statistics of the cells’ motions are the same in both the x- and y-directions. Error bars represent the standard errors of the decorrelation times. ....	129
<b>Figure 46</b> Decorrelation times of the VT plots for images generated by simulated Brownian cells. The RMS displacement along the x-direction was fixed at 10 pixels per loop iteration. The RMS displacement along the y-direction was varied from 0 to 20 pixels/iteration. ....	132



<b>Figure 47</b> An illustration of the relevant parameters that describe the photonic crystal explored in the text. $a$ is the lattice constant, $r$ is the radius of the air spheres, and $R$ is the radius of the silicon spheres. ....	136
<b>Figure 48</b> (Image credit: Wikipedia) The first Brillouin zone of an FCC lattice. Points within the volume that are bounded by the gray planes lie within the zone. Roman letters are used to denote special crystallographic vertexes on the zone boundary and Greek letters denote special directions in reciprocal space. $\Gamma$ denotes the origin of reciprocal space. ....	137
<b>Figure 49</b> The setup for an optically-controlled active medium. Collimated light from a 532 nm laser beam of variable power is focused by a lens into the suspension of polystyrene spheres in water. Typical concentrations of spheres are of the order of 1% by weight. The multiply scattered intensity fluctuations are picked up by a detector and their power spectrum is recorded. ....	148
<b>Figure 50</b> The mean squared displacement (MSD) of a particle undergoing Brownian motion vs. time. The plot was generated using the above algorithm and the results were averaged over 200 individual particle trajectories. Other simulation parameters include the particle's hydrodynamic radius (0.25 $\mu\text{m}$ ), the particle density (1.05 $\text{g/cm}^3$ ), and the temperature (300 K). Note the transition from ballistic to diffusive motion around the relaxation time, $\gamma^{-1} \approx 20 \text{ ns}$ ....	154
<b>Figure 51</b> Lab frame (x-y-z coordinate axes) and the frame of a single plane wave (x'-y'-z' axes) whose k-vector lies along the z' axis. The red outlined plane is normal to the z' axis and contains the electric field vector $\mathbf{E}$ . ....	157
<b>Figure 52</b> a) Probability distribution function for the intensity of the x-polarized component of the simulated speckle field in the x-y plane. Inset: the real part of x-component of the field. b) Histogram of intensities which take all electric field directions into account. Inset: The intensity distribution within the x-y plane. Solid lines represent a fit to Eq. (118) and a plot of Eq. (119), respectively. The value for the mean intensity in (b) is the mean of the data. ....	158
<b>Figure 53</b> The temporal autocorrelation of the x-component calculated from the simulation. The phases of the 50 plane waves comprising the field varied randomly in time according to a Gaussian-shaped ACF with a characteristic time of 0.1 $\mu\text{s}$ . The fit has a characteristic time of 0.03 $\mu\text{s}$ . ....	159

## LIST OF TABLES

<b>Table 1</b> List of parameter values used for the DOS calculation. ....	139
--	-----

## LIST OF ABBREVIATIONS

<b>ACF</b>	Autocorrelation function
<b>ACT</b>	Activated clotting time
<b>DAQ</b>	Data acquisition device
<b>DDM</b>	Dynamic differential microscopy
<b>DLS</b>	Dynamic light scattering
<b>DOS</b>	Density of states
<b>DWS</b>	Diffusing wave spectroscopy
<b>FCC</b>	Face-centered cubic
<b>FOV</b>	Field of view
<b>LCI</b>	Low coherence interferometry
<b>MCF</b>	Mutual coherence function
<b>MEMS</b>	Microelectromechanical systems
<b>MSD</b>	Mean squared displacement
<b>OB</b>	Optical binding
<b>OPS</b>	Optical path length spectroscopy
<b>PALM</b>	Photoactivation Localization Microscopy
<b>PCS</b>	Photon correlation spectroscopy
<b>PSD</b>	Power spectral density
<b>SLED</b>	Super luminescent light emitting diode
<b>STORM</b>	Stochastic Optical Reconstruction Microscopy

# CHAPTER 1: ELEMENTS OF OPTICS AT THE MESOSCALE

## Defining Mesoscale Optics

Mesoscale optics is the study of scale-dependent light-matter interactions in complex systems [1,2]. To be more precise, it provides a framework for understanding optical phenomena whose characteristics depend critically upon how much of a material light has encountered. Alternatively, its foundation rests upon the idea that the interpretation of an optical signal must change as the light propagates through larger volumes of the system. In this dissertation, this mode of thinking has been applied to solve electrodynamic problems in complex media involving length and time scales that span many orders of magnitude. Unexpected and emergent behavior sometimes appeared that could not have been predicted by simply examining individual parts of the system or its bulk optical properties alone [3]. And because many materials exhibit similar microscopic behaviors, mesoscale optics is very useful as a means for understanding phenomena from a host of other fields, such as materials science and biology.

## *Characteristics of Mesoscale Systems*

The word “mesoscopic” is sometimes used in place of “mesoscale” because of the similarity with the words “microscopic” and “macroscopic.” This analogy, however, is misleading because it suggests that the mesoscale is merely some intermediate length scale between these two regimes. This view does not include the fact that mesoscale systems exhibit properties that change across many orders of magnitude of space and time. To counter the idea that the mesoscale is just a length scale, it has been stated that “there is no mesometer [4].” Rather, a mesoscale system is better characterized by its behavior and the interactions between

its parts. Typically, as the system grows in size and more parts are added, new characteristics of the system arise as a consequence of their interaction.

As an illustrative example, consider the formation of a crystal from a melt approaching the critical temperature. Within the melt, a few atoms may join together through electrostatic interactions into a small crystal nucleation site. Relative to the rest of the atoms in the melt, which are randomly moving about due to thermal fluctuations, these atoms have arranged themselves into an ordered array. However, due to their small number, this arrangement may still be torn apart by thermal fluctuations. Eventually, more and more of the free atoms may by chance join the nucleation site until a macroscopic crystal has formed. The entire process may be viewed at different times as a system comprised of a number of different atoms whose positions are maintained by their interaction. The rigidity and flexibility during the early stages of the crystal growth is strongly dependent on the number of atoms it possesses, or, equivalently, the scale of the system. In this sense, an early seed crystal displays mesoscopic behavior.

Another common feature of mesoscale systems is disorder. If you could zoom in on a material indefinitely you would almost certainly encounter disorder in the material's structure at some magnification. What appears macroscopically homogeneous, like a glass of milk, is in actuality a random combination of all its parts, such as the fat globules and proteins of the milk floating about in the water. The interesting thing about mesoscale systems is that the disorder at small scales tends to average or smear out at larger scales until just a few properties are needed to describe the bulk material. In this sense, a mesoscale system exhibits some sort of intermediary behavior between microscopic chaos and macroscopic order.

Real-world examples of mesoscale systems span a multitude of fields. They include biological cells and tissues [5,6], colloidal and polymeric fluids [7,8], disordered and quasicrystals [9,10], and fabricated nanostructures, such as metamaterials and optically induced crystals and ratchets [11–13]. For all of these examples, continuum models fail to adequately describe the systems because of their limited size. Conversely, because the behavior of these systems depends on the interactions between their parts, the natures of the systems can't be arrived at by studying the parts in isolation [3].

To summarize, the important features of a mesoscale system are the system's size (which is related to the number of its component parts), and the nature and strength of the interactions between the components. Mesoscale systems display characteristics that depend upon the scale of interest and exhibit fluctuations that decrease inversely with the size, or even duration, of the system.

In the next section, the focus will begin with optics and an emphasis on probing and controlling disordered systems. A concept that is central to mesoscale optics will be introduced: the volume of light-matter interaction. This concept is analogous with the size of a mesoscale system in that it effectively determines the properties of the material being probed. The size and duration of the interaction volume may be tuned by the experimentalist to optimize the transmission of information from the material to the observer. It also suggests how light may be used to impart momentum to regions inside a disordered system and thereby control it to some degree. It will become clear that the hallmark properties of mesoscale systems, scale-dependence and disorder, require such a concept to make any sense of their complicated natures.

### *Mesoscale Optics and the Volume of Light-Matter Interaction*

Optics research at the mesoscale requires a certain mode of thinking for analyzing and controlling complex systems with light. The framework extends the ideas about mesoscale systems described above by adding one additional concept: the volume of light-matter interaction. This concept serves two purposes. The first purpose is to better one's ability to understand how the light signal changes with the scale of the system; light that is scattered from a small region is more sensitive to microscopic variations within the region than light scattered throughout the entire bulk [14,15]. The second purpose of this construct is that it helps one avoid the idea that all information in optics is transmitted in the form of images. Rather, the interaction volume frames optics problems within the context of a transfer of information. The goal is to obtain and optimize the information from a light signal that probes a material by appropriately tailoring the interaction volume.

The interaction volume concept is illustrated in Figure 1. In this picture, radiation is incident upon some material and is confined to interact with only a portion of it, either because the material has natural boundaries or because the apparatus was designed to probe a select region. As a result of this interaction, the radiation is absorbed, re-emitted, and/or scattered—possibly multiple times—and eventually escapes to propagate until it is detected. Increasing the size of the interaction volume increases the number of parts of the system that the light encounters. The microscopic and macroscopic limits are the smallest and largest possible volumes of material that the light can explore, respectively. This picture also allows for randomness since the arrangement and coupling between all the parts may vary from one realization of the interaction volume to the next. Different properties of the light (such as

wavelength, direction of propagation, or polarization) will have been altered from their incident state after interacting with the material within this volume. These differences contain information about the material's structure within the volume.

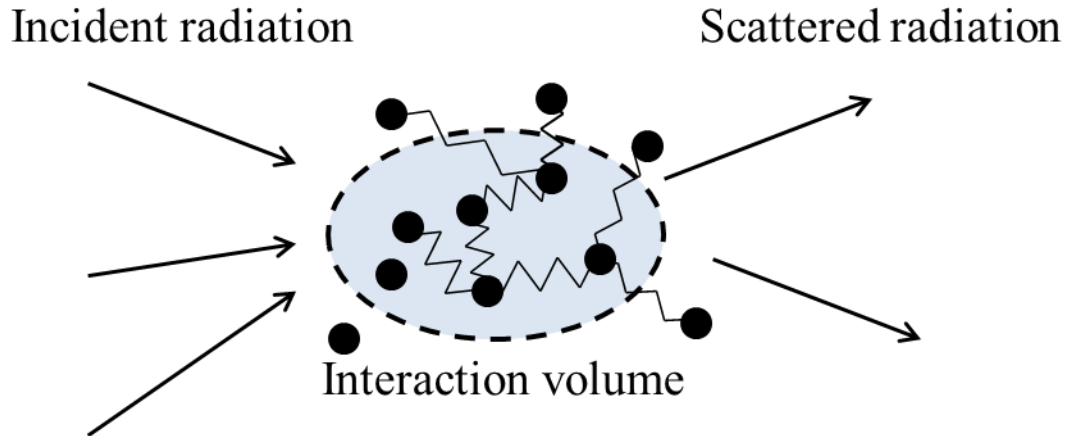


**Figure 1** A mesoscale system probed by some incident radiation. The number of components (black dots) within the volume of the light-matter interaction (encircled by the dotted line) and the coupling between the components of this system (represented by springs joining the particles) determines the nature of the scattered and re-emitted light.

The physical size of the interaction volume that is relevant to the study of mesoscale behavior is usually determined by the wavelength of the light and the length scale of the interaction between the parts. Material structures that are much smaller than a wavelength and located close together experience the same instantaneous electromagnetic field when illuminated. As a result, they collectively act as one structure. Structures that are on the order of a wavelength in size often exhibit resonant scattering, such as Mie scattering from spheres [16]. Coupling between objects on these length scales may give rise to correlated scattering, such as that observed in fractal aggregates [17]. Structures much larger than a wavelength may be either homogeneous and described by ray optics or inhomogeneous and described by a transport of intensity [1]. At this point, the mesoscale is no longer relevant and one need only concern oneself



with bulk optical properties. Based on these examples, the rough limit on the scales of sizes involved in mesoscale optics ranges between 100 nm and 100  $\mu\text{m}$ .

The duration of the light-matter interaction is also an important concept to consider when designing an experiment. One reason for this is that the temporal resolution of any optical measurement is often limited in practice by the spatial resolution. More precisely, this means that probing large volumes in detail takes a long time, while it is often easier to observe fast dynamics from a small region of space, like measuring the fluorescence lifetimes of individual fluorophores. Another reason why the duration of the interaction volume is important is that the scattered light signal may actually change its behavior continuously and over many orders of magnitude in time. As an example, dynamic light scattering (DLS) measures the average time of a fluctuation in a single speckle of light scattered from macromolecular solutions to infer certain properties of the medium [18]. DLS measurements typically last from microseconds to tens of milliseconds to ensure that all the possible relaxation times describing the material's microscopic makeup are captured.

At this point a warning must be made regarding the ability of light to sense mesoscale systems. The coupling between the parts in a system, regardless of its nature, is very important because it is responsible for the collective behavior of the whole system. Light's ability to carry momentum may significantly affect this coupling. For this reason, truly passive sensing of a mesoscale system is not possible. In practice, however, the momentum exchange between light and a material can be made small enough to have a minimal impact. On the other hand, this characteristic of light opens the possibility for control of mesoscale systems. Depending on one's goals, the magnitude of light's effects on a system should be taken into account.

The concept of the interaction volume, its size, and the duration of the light-matter interaction must be supplemented by additional information to be of use in practice. What is the nature of the incident radiation, i.e. its polarization, spectral composition, coherence, and numerical aperture? What determines the size of the interaction volume? Where are the material boundaries? Are we measuring in the near-field, far-field, or both? Is the light-matter interaction linear or nonlinear? Questions such as these must be addressed before one may successfully probe a mesoscale system—and possibly control it.

### Three Aspects of Mesoscale Optics

Because mesoscale optics is a necessarily broad field, existing works from the literature that fall under its description have been classified according to three primary approaches: observing a mesoscopic system, modeling the light-matter interaction at these scales, and controlling a mesoscale system with light.

#### *Observing Mesoscale Phenomena with Light*

Very different optical techniques may be required to understand a complex, mesoscale system. This is because any given technique is often best-suited to exploring only a range of the length and time scales that are relevant to the system. Observations of mesoscale phenomena, which exhibit a range of behaviors that vary with scale, are facilitated by tools that allow us to control the volume of the light-matter interaction.

Many such tools already exist. Take, for example, optical coherence tomography (OCT), which examines localized volumes by suppressing multiple light scattering from a specimen through coherence gating [19]. Confocal microscopy utilizes conjugate pinholes to reject light

from the out-of-focus regions of the sample and improve the image contrast within the volume of interest [20]. Variable coherence microscopy is another technique that localizes the scattered signal from regions of the sample that lie within two coherent volumes [21]. All three modalities, collectively known as gating-techniques, extract information about a sample by combining multiple measurements that are constrained to particular regions of the sample.

Fluorescence-based superresolution techniques like photoactivated localization microscopy (PALM) and stochastic optical reconstruction microscopy (STORM) are popular ways to localize a light signal within fixed biological specimens [22,23]. These techniques are enabled by the ability to randomly “turn on” a limited number of fluorophores that are bound to structures of interest, thereby allowing the experimenter to localize them to within a few tens of nanometers. The large-scale structure of the object is then obtained by adding together many images containing only a few emitting fluorophores.

Dynamic light scattering (DLS) and diffusing wave spectroscopy (DWS) are the traditional methods for optically interrogating the dynamics of micro-, meso-, and macroscopic systems [18,24,25]. Unlike the previously mentioned techniques, which investigate spatial variations of material properties, DLS and DWS are capable of exploring dynamics across many temporal orders of magnitude—typically from nanoseconds to seconds. In DLS, singly scattered light from a small material volume is recorded by a detector and the second-order moment of the intensity is calculated. System-dependent models then link these statistics to properties of the material. DWS extends DLS to multiply scattering systems by accounting for the dispersion of the photon path length distribution [24]. Both DLS and DWS have been implemented in studies of particle sizing, reaction kinetics, viscoelastic measurements, and bacterial motility [18,26]. A

major drawback to these two techniques, though, is that the light-matter interaction must occur over a relatively large volume, meaning that they are limited to large spatial scales. Differential dynamic microscopy (DDM) attempts to overcome this limitation by measuring the dynamics of a scene through a microscope objective [27]. Here, the cost of increasing the resolution at the spatial scale is paid for by a decrease in temporal resolution; it's limited to milliseconds.

Optomechanical systems may be used to sense extremely small scale (even quantized) vibrations of “large” objects such as mirrors [28]. Typically, these systems are realized by an optical resonator with the vibrating mirror at one end. Importantly, the small number of photonic modes and their coupled interaction with the modes of the mirror make this an inherently mesoscale system. This coupling makes optomechanic sensors extremely sensitive tools.

These are just a few examples of the ways in which optical sensing techniques explore systems at the mesoscale, but of course many more exist. They may be classified by either those that reduce the volume and time of interaction (OCT, confocal microscopy) or by those that extend the measurement across many orders of magnitude (DLS). The question as to which techniques are better or worse can only be made with regards to the specimen they are investigating. With this in mind, it is clear that observing new types of systems and phenomena may require new techniques.

### *Modeling Mesoscopic Light-Matter Interactions*

Due to the breadth of phenomena covered by mesoscale optics, one may think it would be difficult to provide a general quantitative treatment for the light-matter interaction in these systems. This is more or less true. However, many of the numerical and analytical tools that are

used by researchers share similar features. For example, the theory of diffusion may describe colloidal particles, the propagation of radiation in disordered systems [1,29], or cell motility [30,31]. Each field uses different terminology and modifications to the underlying theory to fully describe the system under study. However, the principle aspects of the theory remain the same, which demonstrates the interconnectedness of a large range of phenomena.

The importance of randomness in mesoscopic systems has implications for any model of mesoscale light-matter interaction. By random it is meant that some occurrence is predictable only to an extent governed by the laws of probability. This is due to the complexity of the systems involved; it is not possible to fully account for the details. More precisely, information is lost as the volume of interaction grows in size and macroscopic behaviors emerge. As a result, most models are designed around moments of some underlying probability distributions, such as field and intensity correlations [32] or particle mean squared displacements (MSD). Another challenge to modeling interactions in mesoscopic optics is quantifying the concept of disorder. Applying the word “disorder” to a photonic crystal may mean that there is a random variation in the size of the unit cell, an aperiodic perturbation of the lattice, large-scale lattice mismatches, or any combination of the three. The word “disorder” fails to differentiate these three examples and leads one to think that the measurable signature of each effect is the same, when in fact it is not [33,34].

Mesoscale optics is a highly interdisciplinary field that requires a combination of many different ideas to describe the light-matter interaction in complex systems. It draws its ideas from established fields such as condensed hard and soft matter physics, materials science, chemistry, stochastic processes, fractal mathematics, and, of course, fundamental optics. However, these

ideas are not simply being reapplied to new problems. Rather, their combination is a necessary synthesis of new ideas and methods to describe light propagation through scale-dependent systems.

### *Optical Control at the Mesoscale*

A major goal of mesoscale optics is to facilitate control over mesoscopic systems. Fundamentally, this is possible because light carries energy and both linear and angular momentum [35]. The first mechanism of control, energy transfer, has been extensively studied as a means of control by way of photochemical reactions such as those found in many biological systems [36]. The focus in this section, however, will be on momentum transfer between light and a material.

Micro- and nanosized objects have been the subject of momentum-based optical control experiments since Ashkin demonstrated the concept of laser trapping in 1970 [37]. Since these first demonstrations, the field of laser trapping has expanded significantly, especially into the realm of biophysics where it has been used to study processes such as RNA transcription and protein folding [38]. Laser traps used in experiments such as these are formed with high NA objectives that can focus light so strongly that the trapping force becomes greater than the radiation pressure [39]. For single-beam systems, this strong focusing is essential for trapping particles in three dimensions.

Studies involving optical control exploded in number once adaptive optics tools, such as spatial light modulators (SLM's), became widely available. These tools allowed for the precise shaping of coherent wavefronts, which could in turn exert a force with a desired strength and

magnitude upon a particle. Today, adaptive optics techniques are regularly used to generate user-defined light fields, such as the non-diffracting Bessel and Airy beams [40,41], multi-trap and dynamic tweezers [42], and optical “spanners” for spinning particles and microrotors [43]. The state of the art has become so refined that a generic, multi-trap tweezer setup employing an SLM may even be controlled with an iPad that utilizes software “apps” available at the Apple App Store [44].

Optical control also means using light to exploit the interactions between particles and their environment, which is extremely important for mesoscopic systems. For example, when particles located very close to one another are illuminated with a coherent beam, the light-matter interaction binds the particles at predictable distances in a phenomenon known as optical binding [45]. Breathing modes and self-organization are some of the phenomena observed in these bound particle states as they interact with their thermal environment, which makes them simple experimental models for atomic and molecular physics and statistical mechanics [46].

The state of the art in control of colloidal systems is currently focused, in part, on active media, or media composed of suspended particles that are driven by either intrinsic or extrinsic energy sources. The dynamics of active media are analogous to the dynamics of vacuoles and other cell compartments that move within cells under the influence of molecular motors [47]. The motion of such compartments is driven partly by the thermal excitations from the cytoplasmic bath and also in part by the motors. There have been some attempts to classify these systems with effective temperatures such that the fluctuation-dissipation theorem may still be applied to them [48,49], though there is evidence that the effective temperature description is not universal [50]. Other studies of active media have considered the diffusion of inert particles in an

aqueous solution containing much smaller and mobile microorganisms, such as *E. coli* bacteria [51]. In these studies, attraction forces between particles due to the depletion mechanism were reduced due to the inherent motion of the swimming bacteria. Finally, bringing the focus back to optics, the free diffusion of particles composed of two types of materials, or Janus particles, can be manipulated by using light that selectively heats one side of the particles and gives rise to a thermophoretic flow [52]. This has resulted in the first demonstration of an optically-controlled active medium, with many more realizations expected to follow.

Due to the increasing ease with which light may be manipulated, optical control experiments possess much promise for resolving some disputes over the nature of the diffusion of particles in random potential landscapes [47,53–57]. In addition, the ability to control active media with light may lead to further understanding and insight in the control of mesoscopic systems since active media are highly coupled and often exhibit nonlinearities [7]. Therefore, this work should be important for engineering integrated photonic devices and microelectrical mechanical systems (MEMS) that display similar qualities.

### Why Study Mesoscale Optics?

Mesoscale systems are found in many fields of study: physics, biology, geology, and even psychology, sociology, and economics [58]. This is because a mesoscale system comprises any system that changes its behavior over a range of length or time scales, which arguably applies to anything real. Indeed, Mandelbrot argued that scaling effects are a characteristic of Nature itself [59]. The hierarchy of organization that is observed in physical and biological systems (atoms forming molecules that form matter and cells forming tissues that form organs



and organisms) attests to the fact that mesoscale systems are everywhere. Importantly, the mesoscale exists in a state of change. In this state, an increase in the number of parts of a system leads to very different and sometimes unpredictable effects on the entire system. This is only possible if the parts interact and are constrained in some way, whether by a boundary or their mutual interaction.

Mesoscale optics brings this line of thinking to various research areas within optics. In mesoscale optics, the scale-dependent interaction of light with matter is the central idea for understanding and controlling complex systems. Non-Gaussian fluctuations of optical properties and variable material responses spanning multiple orders of magnitude require a coherent logical framework to surmount; this is exactly what mesoscale optics provides.

And finally, just as new phenomena emerge from systems undergoing transitions to increasing complexity, it should not be surprising that fundamentally new and unpredictable optical phenomena will result from studies of the light-matter interaction at the mesoscale. The true value of this framework will likely become clearer as it continues to be applied throughout the many different areas of optics.

### Organization of Work

Light can be used to record fast processes, resolve small objects, and precisely control elements of complex systems. Numerous techniques have already been realized for achieving these goals and more. This study comprises a synthesis of technologies and ideas for studying various mesoscopic phenomena with light.

The elements of this dissertation are divided into the three categories that best describe their objectives: observations, modeling, and control. They are illustrated in Figure 2. These goals are not mutually exclusive but rather serve as rough means for classification. In some cases, a work may encompass all three. Controlling a complex system requires some sort of sensory feedback and appropriate models for interpreting data and exploring parameter spaces, for example. The following chapters include in detail several projects covering all three aspects of mesoscale optics. The chapters include descriptions of the main ideas while most of the specific technical information has been moved to the appendixes.

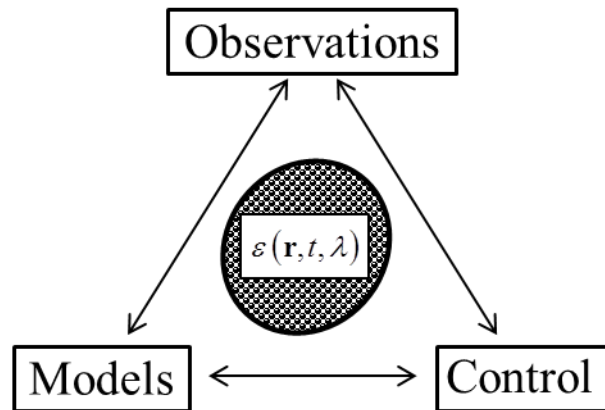


**Figure 2** The three aspects of mesoscale optics. All three involve the exploration of a mesoscopic system with optical parameters given by a dielectric permittivity,  $\epsilon$ .

## CHAPTER 2: OPTICAL SENSING IN MESOSCOPIC SYSTEMS

Mesoscopic systems comprise a number of different types of materials that exhibit complex, microscopic properties. These systems include photonic crystals, biological cells and tissues, polymer and colloidal solutions, and many other disordered materials. This chapter contains information about the development of a number of optical techniques for learning about such systems.

### Low Coherence Interferometry for Probing Multiply Scattering Media

Low coherence interferometry (LCI) employs broadband light sources to limit the volume of interaction between the light and the sample [60–62]. Typically, the bandwidth of these sources extends over a few tens of nanometers, which means the coherence length is a few tens of microns. The light sources in this work are super luminescent light emitting diodes (SL-LED's, or just SLED's), though broadband CW lasers, such as Ti:sapphire lasers, may be used as well.

LCI involves interfering scattered light from a sample with a reference beam whose path length may be controllable. Due to the short coherence length of the light source, an interference signal is obtained only from scattered light that has traveled roughly the same distance as the reference beam within the interferometer and the sample. As a result, the envelope of the interference signal and the phase of the fringes encode properties from a controlled volume of the material. This characteristic of LCI allows the experimenter to probe different optical path lengths inside a multiply scattering medium, for example [60]. Furthermore, the light-matter interaction across multiple spatial and temporal scales may be probed as well [63].

### *Basics of Low Coherence Interferometry*

A simple LCI setup is illustrated in Figure 3. Light from a broadband source, like an SLED, enters the interferometer and is split onto two paths, one going to the medium under investigation (the sample arm) and the other towards a mirror that may be moved along the optical axis (the reference arm). The light reflected from the mirror and the sample is recombined at the detector. Information about the sample is encoded onto the sample arm light, which is then recovered from the interference between the light coming from the sample and reference arms.

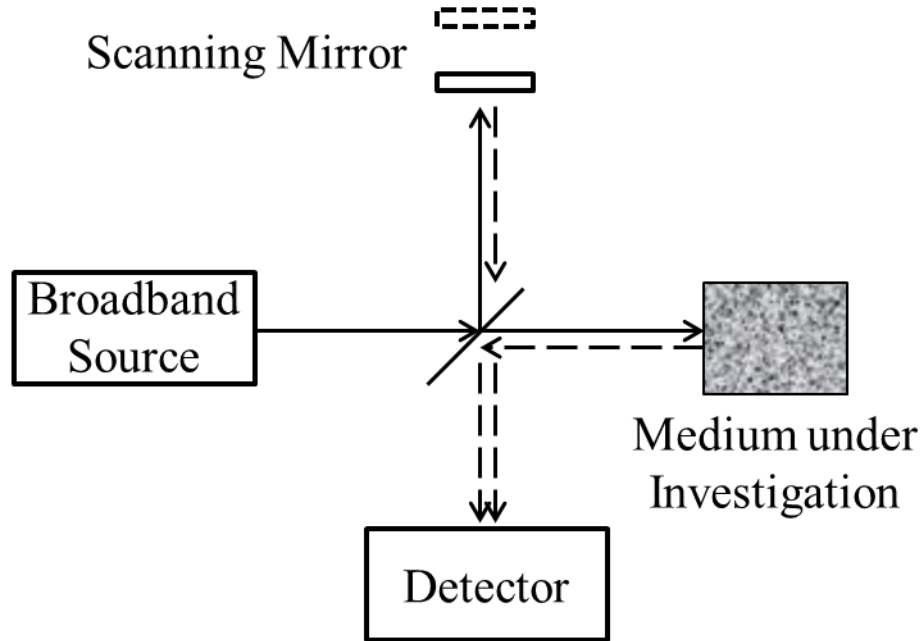


**Figure 3** A basic LCI setup. Light from the broadband source is split along two paths, one leading to the medium under investigation and another to a reference mirror that moves along the optical axis. Light reflected from the medium and the mirror (represented by the dashed lines) travels to the detector.

The expression for the intensity at the detector in an LCI setup will now be derived and it will be shown how it relates to information about the material. For simplicity, first assume that the medium is a mirror with reflectance  $r$  that is independent of wavelength. (The more complicated situation of a multiply scattering medium will follow from this treatment.) Let  $E_0$

represent the electric field from the reference arm.  $rE_0$  is therefore the field from the sample arm. The scanning mirror is initially placed at a distance  $s_0/2$  from the beamsplitter and the effective sample arm mirror is at a distance  $s/2$ . This makes the optical path lengths along each arm  $s_0$  and  $s$ , respectively. The field at the detector is the sum of the field from each of these arms, so that the detector's photocurrent is proportional to the time-averaged square of this sum (i.e. the intensity). Considering at first only the intensity of a single spectral component of the source given by the wavenumber  $k$  leads to

$$I(s, s_0; k) = \left\langle \left| E_0 \exp(iks_0) + rE_0 \exp(iks) \right|^2 \right\rangle_t \quad (1)$$

where the brackets denote a time average. For the rest of this section, the subscript  $t$  will be omitted, the time average being understood. Carrying out the square gives

$$I(\Delta s; k) = \left\langle |E_0|^2 \right\rangle + \left\langle |rE_0|^2 \right\rangle + \left\langle 2\text{Re} \left[ r^* E_0^* E_0 \exp(-ik\Delta s) \right] \right\rangle \quad (2)$$

with  $\Delta s = s - s_0$ . Let  $I_0 = \left\langle |E_0|^2 \right\rangle$  so that Eq. (2) may be simplified to

$$I(\Delta s; k) = I_0 (1 + |r|^2) + 2I_0 \text{Re}(r) \cos(k\Delta s). \quad (3)$$

Now, let  $S_j$  represent the contribution from the  $j$ 'th spectral component to the full spectrum of the source. Because there is no phase relationship between the spectral components of a SLED, they may be added in intensity to produce the total intensity on the detector as a function of  $\Delta s$ .

$$I(\Delta s) = (1 + |r|^2) \sum_j S_j + 2\text{Re}(r) \sum_j S_j \cos(k_j \Delta s) \quad (4)$$

An SLED has a continuous spectrum, so Eq. (4) must be modified accordingly. Multiplying by  $\Delta k \equiv k + 1 - k = 1$  and taking the limit  $\Delta k \rightarrow 0$  gives

$$I(\Delta s) = (1 + |r|^2) \int_k S(k) dk + 2 \operatorname{Re}(r) \int_k S(k) \cos(k \Delta s) dk. \quad (5)$$

The first term of the right-hand-side of Eq. (5) is a constant with respect to  $\Delta s$ , which as a reminder is the difference in optical path lengths between the two arms of the interferometer. The second term is a cosine transform of the spectral density of the source. By the Wiener-Khinchin theorem, this expression is just the mutual coherence function (MCF) of the light source, or [64,65]

$$\Gamma(\Delta s) \equiv \int_{-\infty}^{\infty} S(k) \exp(ik \Delta s) dk = 2 \int_0^{\infty} S(k) \cos(k \Delta s) dk. \quad (6)$$

The MCF describes the coherence properties of the light source and determines the range of values of  $\Delta s$  for which interference fringes may be observed.

The information about the sample “mirror,” i.e. its reflectivity  $r$ , may now be extracted from the measured  $I(\Delta s)$ . Defining  $P \equiv \Gamma(0) = \int_k S(k) dk$  as the total power in the beam of light entering each arm of the interferometer and  $B \equiv (1 + |r|^2)P$  as a measurable background intensity, the real part of the reflectivity is given by

$$\operatorname{Re}(r) = \frac{I(0) - B}{P}. \quad (7)$$

If  $P$  is not known, the reflectivity may be determined from prior knowledge about the MCF and scanning the mirror:

$$\text{Re}(r) = \frac{I(\Delta s) - B}{\Gamma(\Delta s)}. \quad (8)$$

This treatment is only for a single mirror of reflectivity  $r$  acting as the sample. The case of a real scattering medium must now be addressed. In multiply scattering samples there will be many possible paths for a photon to take. These paths may be described by a distribution function representing the relative probability that a photon will travel a path with a length of  $s$  inside the material. This probability is denoted as  $p(s)ds$ . The corresponding concept may be illustrated as a series of partially reflecting mirrors at different distances  $s_j/2$  along the axis of the interferometer's sample arm as illustrated in Figure 4. If, for example, there are three mirrors, then the recorded signal will contain components consisting of a convolution of the MCF with delta functions of weight  $p(s_j)ds, j = 1, 2, 3$  positioned at  $s_1/2, s_2/2$ , and  $s_3/2$  along the optical axis of the sample arm. Strictly speaking, the effective mirrors must be separated by a distance greater than the coherence length of the source to be resolved. However, for most materials of interest  $p(s)$  spans a range on the order of millimeters, which is nearly one hundred times greater than the source coherence length. Therefore, the medium may be modeled as a discrete number of effective, partially reflecting mirrors represented by delta functions and separated from one another at a regular interval of one coherence length.

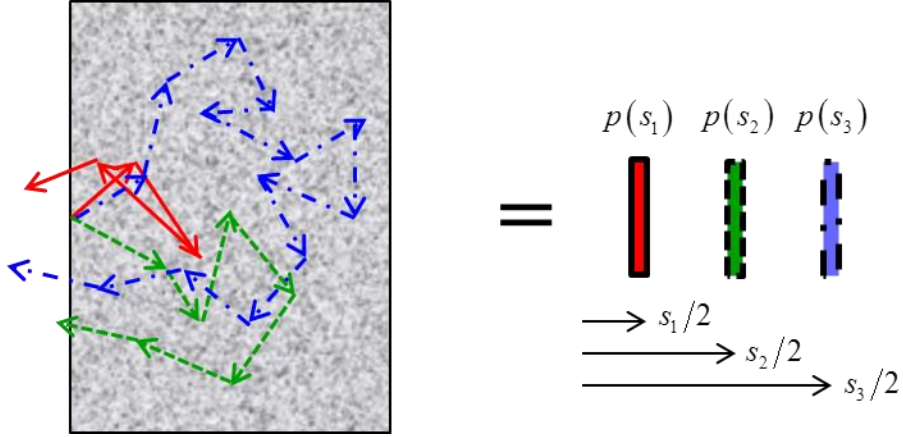


**Figure 4** A multiply scattering medium possesses many possible path lengths for a photon to take, each having a length  $s_j$ . Three possible paths of differing lengths are illustrated. Conceptually, each path may be thought of as a partially reflecting mirror with reflectivity proportional to the probability of a photon traveling that distance inside the material. The distance of the mirror from some reference point is twice the distance of the corresponding path length.

Under these considerations, the recorded interferometer signal for this multiple scattering medium is

$$I(s_0) = \sum_j \left(1 + |r_j|^2\right) P + \sum_j p(s_j) \Gamma(s_j - s_0) \quad (9)$$

which is just the convolution described earlier. Note that the signal is now described as a function of the absolute position of the reference mirror. In practice, the origin of this position may be arbitrarily placed. Additionally, it's worth repeating that if the width of the MCF is very narrow compared to the width of  $p(s)$ , then the path length distribution may be obtained within an accuracy of the coherence length of the source. For the sake of generalizing the argument, multiplying Eq. (9) by  $\Delta s \equiv s + 1 - s = 1$  and taking the limit as  $\Delta s$  goes to zero produces

$$I(s_0) = B + \int_s p(s) \Gamma(s - s_0) ds \quad (10)$$

where  $B$  is again a constant background intensity.



It has now been demonstrated that LCI may be used to measure the reflectivity of a single flat interface or the path length distribution function of a multiply scattering medium. The ability to probe such media is enabled by the rejection of all light but that which travels a very narrow range of path lengths relative to the total range of path lengths involved. This characteristic has been exploited to image below the surface into tissue, such as in optical coherence tomography (OCT) [19], and also allows for a control of the size of the interaction volume within the medium.

Several important factors have not been addressed in this treatment. These include sample reflectivities that vary drastically with wavelength and finite numerical apertures of the detection optics. Still, the treatment holds for a large range of materials and is useful because of its simplicity.

#### Measuring Photon Diffusion Coefficients Independently of Boundary Conditions

One implementation of LCI called optical path length spectroscopy, or OPS, may be used to determine the optical properties of a multiply scattering medium from the recorded path length distribution function. These properties are important for certain diagnostics, such as the non-invasive detection of tumors within the body [66,67]. OPS is advantageous for this purpose because of its simplicity and flexibility. The full integration of the setup into fiber optics eliminates the need for careful alignments.

Perhaps the most common optical descriptors of multiply scattering media are the scattering mean free path,  $\ell_s$ , the absorption length,  $\ell_a$ , and the scattering anisotropy  $g$  [1]. Taken together, they form a universal description of the incoherent transport of radiation within a

general, disordered system [1,29]. Under appropriate conditions, the scattering mean free path and anisotropy may be combined with the energy transport velocity to form the photon diffusion coefficient,  $D \equiv v\ell_s/3(1-g)$  [1]. In this case,  $D$  and  $\ell_a$  describe the transport process.

Unfortunately, geometrical considerations of the host medium often make it difficult to determine these pieces of information. One reason for this is that analytical descriptions for the time-resolved or integrated intensity from a multiply scattering medium only exist for a few specific geometries, like a semi-infinite half-space or the thin slab of infinite extent [67]. A more practical concern is that material boundaries, such as the interface between air and tissue, impose additional constraints on the fits of measured intensity profiles [68,69]. These constraints have a physical basis in the idea that some light that may be reflected back into the medium at these boundaries, which therefore act as effective sources of light. For this reason, radiation transport models assume a non-zero value for the specific intensity (i.e., radiance) over a short distance outside of the medium. Most often, this is represented by the extrapolation length,  $z_b$ . This concept is illustrated in Figure 5 for a point source located a short distance from one surface of a slab of infinite transversal extent.

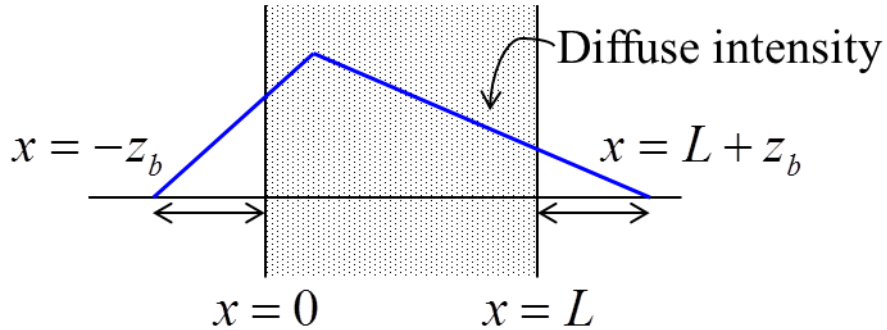


**Figure 5** The diffuse intensity goes to zero at a distance  $z_b$  outside of the scattering medium. This distance is known as the extrapolation length and is determined by  $\ell^*$ , the refractive indexes of the two media, and the scattering anisotropy of the scatterers.

The boundary extrapolation length depends on many different factors, including the transport mean free path  $\ell^* \equiv \ell_s / (1 - g)$ , the effective refractive indexes of the two media, and the scattering anisotropy of the scatterers [68,70,71]. *A priori* information and other models are typically used to make estimates of its value. Unfortunately, estimates for  $z_b$  that are off by relatively small amounts may lead to large errors for the values of the extracted transport parameters [69], therefore necessitating accurate methods for determining the extrapolation length.

To circumvent the need for an independent estimation of the extrapolation length, a modified OPS setup which allowed for more control over the size and shape of the interaction volume was developed. This setup is displayed in Figure 6. Briefly, a SLED was coupled into a fiber-based Michelson interferometer. The sample arm contained a 50/50 fiber splitter which split the light equally along each arm. Note that the fibers from each arm were different lengths. The reference arm contained a scanning mirror. The interferogram was recorded as the mirror was translated. The envelope of this interferogram represented the distribution of path lengths that a photon may have traveled inside the medium, which is denoted by  $p(s)$ .

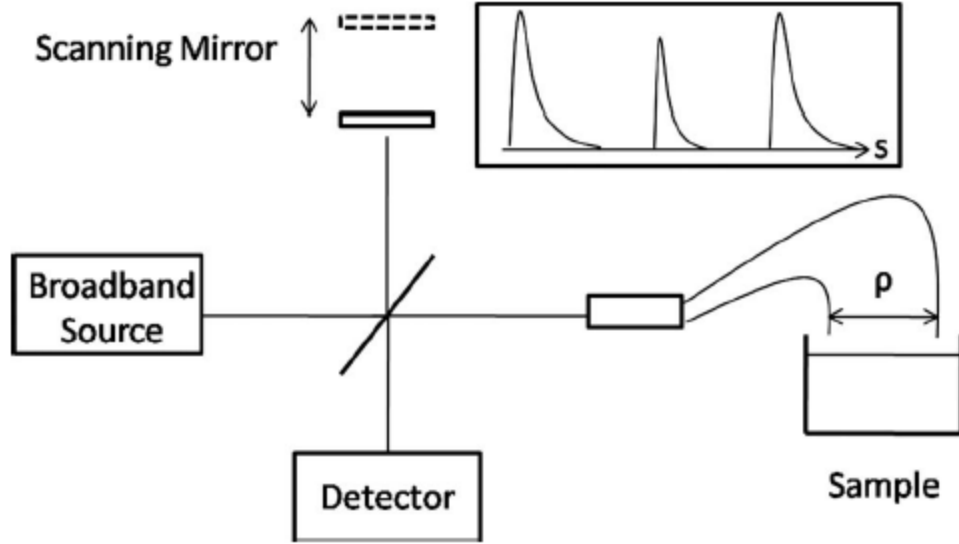


**Figure 6** A bistatic OPS setup for measuring photon path length distributions from a multiply scattering sample. The light is both injected and detected from two fibers situated directly above the sample. The inset displays the envelope of the interferogram. The outside curves are the monostatic path length distributions and the middle curve is the bistatic distribution.

Two types of signals were recorded: a monostatic signal and bistatic signal. Monostatic signals correspond to light that left and entered the same fiber; bistatic signals corresponded to light that left one fiber and entered another. The bistatic signal was a function of the fiber separation distance  $\rho$ . Changing this distance effectively probed different multiple scattering regimes since a minimum path length of  $\rho$  is enforced. Importantly, the effects of the boundary on  $p(s)$  remained the same for each fiber separation so that the boundary extrapolation length could be removed by comparing bistatic signals recorded at different values of  $\rho$ .

As a proof of demonstration of this concept, the bulk scattering properties from a multiply scattering tissue phantom with negligible absorption were determined. The measurement was verified by using two different bounding media: air and oil. Probing the

system over multiple length scales enabled the successful determination of the bulk scattering properties of the phantom without the need to account for  $z_b$ .

### *Bistatic Optical Path Length Spectroscopy*

The modification to the original OPS setup (the original work being described in [60]) is depicted in Figure 6 [72]. Light from a superluminescent LED with a wavelength of 1300 nm and a coherence length of roughly 30  $\mu\text{m}$  is injected into a single-mode fiber-based Michelson interferometer (HP 8504B Reflectometer). The reference arm of the scanning mirror is mechanically translated along the optical axis. Light from the other arm is launched into a 1x2, 50/50 fiber splitter and exits through two fibers that have been cleaved flat and are separated by a horizontal distance  $\rho$ . The fibers also act as detectors by collecting light that has been backscattered from the sample. The distance of the fibers above the sample varies according to the application, but is typically about 1 mm.

Were there only one fiber as in the original OPS demonstration [60], then the light intensity at the detector would be given by Eq. (10). However, taking the modifications from the new setup into account, the signal now takes the form

$$I(s_0, \rho) = B + \int_s p(s, 0) \Gamma(s + s_1 - s_0) ds + \int_s p(s, 0) \Gamma(s + s_2 - s_0) ds + \int_s p(s, \rho) \Gamma[s + \rho + (s_1 + s_2)/2 - s_0] ds \quad (11)$$

where  $s_0$  is twice the distance of the scanning mirror from the splitter, as before, and  $\rho$  is the lateral separation between the probe fibers. The three non-constant terms in Eq. (11) represent the three different curves illustrated in the inset of Figure 6. The locations of these curves are

determined by the different lengths of the two probe fibers, which are  $s_1/2$  and  $s_2/2$ . The first two terms correspond to the monostatic signals (i.e. signals from light that leave and reenter the same fiber) and are convolutions of the source's MCF with the monostatic path length distribution function,  $p(s, \rho = 0)$ . The final term in Eq. (11) is the bistatic signal and consists of light that travels through the medium and enters the probe fiber opposite to the one that the light originated from. This integral is a convolution of the MCF with the bistatic path length distribution function,  $p(s, \rho)$ . Thus, Eq. (11) demonstrates that two different forms of information may be extracted from the bistatic OPS implementation, thereby increasing the information content and throughput and of the measurement.

There are two differences between  $p(s, 0)$  and  $p(s, \rho)$  worth noting. First, for nonzero  $\rho$ , there is a minimum path length that a photon must travel through the medium before it is detected in the bistatic signal. This means that a lower cutoff to the radiation transport process inside a medium may be imposed by the measurement. Second, if any anisotropies in the transport process exists, they may be discerned by comparing the monostatic and bistatic signals. Beyond these differences, it is also important to note that varying the separation between the fibers lends the experimenter a good deal more flexibility than in the monostatic setup.

#### *Determination of the Photon Diffusion Coefficient from Multiple Bistatic Measurements*

For diffusive samples with dimensions much larger than a transport mean free path  $\ell^*$ , the measured curves from the bistatic OPS setup take the shape described by the path length-resolved, backscattered flux [67,73]. The expression for the flux is derived from the diffusion

approximation to the radiation transport equation [1,67,74], which depends on only two parameters of the medium: the photon diffusion coefficient and the absorption length  $\ell_a$ . Though not as general as the equation of transport [1], the diffusion approximation is an accurate model for light transport in many multiply scattering systems and may be refined by exploiting measurements at short path lengths or early photon arrival times [75].

The solution to the photon diffusion equation for the backscattered flux from a point source located one transport mean free path inside a semi-infinite half-space with negligible absorption is given by

$$J(s, \rho) = (4\pi D)^{-3/2} z_0 v s^{-5/2} \exp\left(-\frac{\rho^2 + z_b^2}{4sD}\right). \quad (12)$$

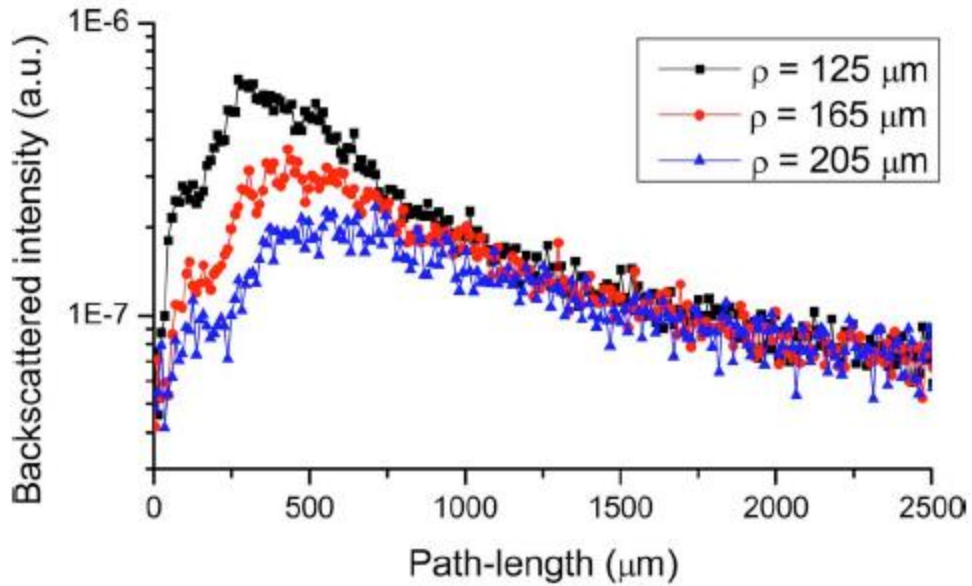
Here,  $v$  is the energy transport velocity and  $D \equiv \ell^*/3$  is the definition of the diffusion coefficient commonly used in the biomedical optics field [67].  $z_0 \equiv 2\ell^*/3$  is the boundary extrapolation length that does not account for material-dependent internal reflections at the boundary, whereas  $z_b$  takes into account these reflections (see Figure 5). The half-space geometry is suitable for many light scattering problems involving tissue within the body. Normalizing Eq. (12) to  $\int_0^\infty J(s, \rho) ds$  for a fixed value of  $\rho$  then gives the path length probability distribution function  $p(s, \rho)$ .

Figure 7 displays three experimental bistatic peaks for the marked fiber separations. The medium is a 10% concentration by weight suspension of 0.43  $\mu\text{m}$  diameter polystyrene spheres in water for which Eq. (12) is a good model of the path length-resolved transport of light. The

probe fibers have been positioned close above the surface of the suspension but are not submerged. Note that these peaks are not normalized. Taking the logarithm of the ratio of any two curves gives, according to Eq. (12),

$$\ln \left[ \frac{J(s, \rho_1)}{J(s, \rho_2)} \right] = \frac{\rho_2^2 - \rho_1^2}{4Ds}. \quad (13)$$

Importantly, this expression is free of the boundary extrapolation length  $z_b$  because it is common to each measurement. Analysis of the path length-resolved behavior of the ratio of two bistatic peaks will, according to Eq. (13), provide information of the medium's photon diffusion coefficient without needing to know the boundary extrapolation length.



**Figure 7** Measured bistatic path length distributions at different fiber separations from a colloidal suspension of 0.43  $\mu\text{m}$  diameter polystyrene spheres at 10% concentration by weight.



### *Results from the Bistatic OPS Measurements*

To test this idea, bistatic peaks were measured from three separate colloidal suspensions with various fiber separations and with two different boundary conditions: an air-liquid interface and an oil-liquid interface. The fibers were located in the air/oil, not the phantom. The dependence of the boundary extrapolation length on the outside medium may be expressed by  $z_b = 2D(1 + R_{eff})/(1 - R_{eff})$ , where  $R_{eff}$  is the Fresnel reflection coefficient going from the scattering medium to the bounding medium and is averaged over all angles and polarizations [71]. If the bistatic OPS technique is independent of the boundary material, then the measured transport parameters should be the same for each interface.

The resulting diffusion coefficients for the suspensions were obtained by averaging the values for  $D$  that were determined over a range of path lengths and fiber separations in Eq. (13). The diffusion coefficients obtained in this manner are displayed in Figure 8 for various combinations of  $\rho_1$  and  $\rho_2 - \rho_1$ . The large deviation at short path lengths ( $s/\ell^* < 5$ ) can be explained in part by the diffusion approximation's poor description of the light transport in this regime.

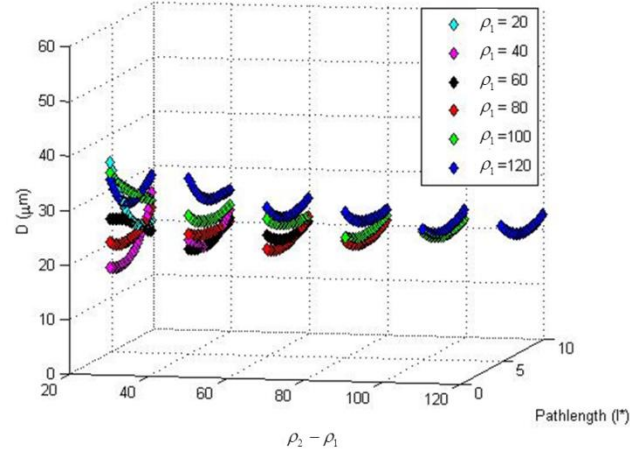


**Figure 8** Calculated values of the diffusion coefficient from the measurements. Path length is in units of  $\ell^*$ .

Figure 9 displays the average diffusion coefficients from three different media and two bounding materials. The three samples A,B, and C were colloidal suspensions of polystyrene spheres with weight concentrations of 10%, 10%, and 5% and sphere diameters of 0.43  $\mu\text{m}$ , 0.33  $\mu\text{m}$ , and 0.43  $\mu\text{m}$ , respectively. Bulk diffusion coefficients were determined from Mie scattering and transport theory [16] and the monostatic values were determined from fits of the curves to Eq. (12) with the theoretical values for  $z_b$ .

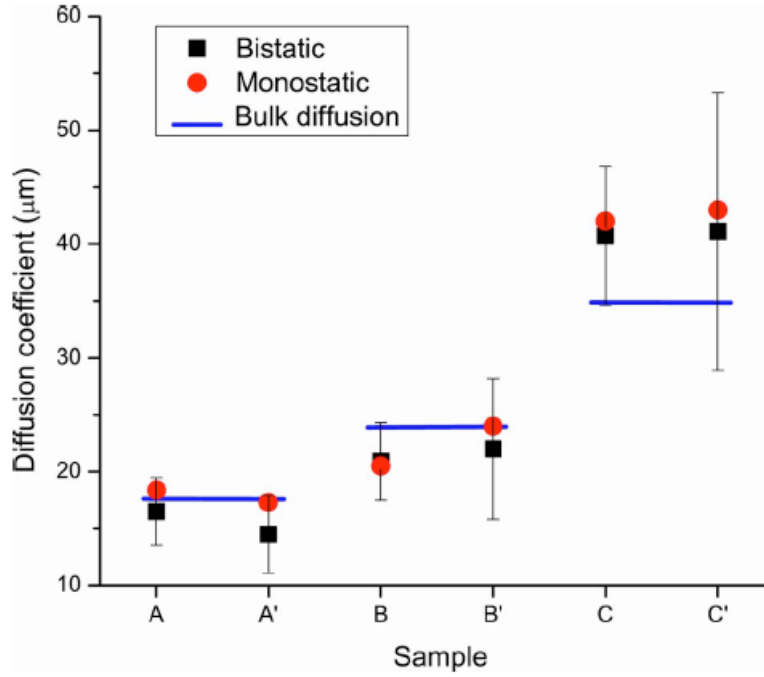


**Figure 9** Average diffusion coefficients extracted from the bistatic OPS setup. Samples A, B, and C are colloidal suspensions of polystyrene spheres at 10% weight concentration and diameter 0.43  $\mu\text{m}$ , 10% and 0.33 $\mu\text{m}$ , and 5% and 0.43  $\mu\text{m}$ , respectively. A', B', and C' are the same samples with oil added on top of the suspensions. The error bars represent one standard deviation of the distribution of the values for  $D$  calculated for various permutations of values from  $(s, \rho)$ .

The bulk diffusion calculations roughly agree with both the monostatic and bistatic measurements. The 5% colloidal sample displays larger error bars because the signal-to-noise ratio of the bistatic curves is quite poor. This could be improved by using a more powerful light source (the SLED used in this experiment emitted a maximum of 5 mW of light). Importantly, no information about the boundary extrapolation length was needed to determine the diffusion coefficients from the bistatic measurements, which proves the claim.

### Low Coherence Dynamic Light Scattering

Low coherence dynamic light scattering, or LC-DLS, is one realization of a group of techniques known as photon correlation spectroscopy (PCS) [18,76]. The simplest

implementation of PCS, known simply as dynamic light scattering (DLS), examines the dynamics of single-scattered light from a sample to infer its microscopic, time-dependent properties. It is perhaps most well-known for measuring dynamic structure factors of complex fluids, such as for colloidal particle sizing applications [18,62,77].

In our implementation of LC-DLS, a fiber is inserted into a complex fluid (e.g. a colloidal suspension, a gel, or even blood) to record the fluctuations of light that is scattered by the fluid with time (see Figure 10). The light is both injected and collected from the same fiber and originates from a SLED whose coherence length is on the order of  $10\text{ }\mu\text{m}$ . The detector sees a time-dependent interferogram which is produced by interference between the backscattered light from the sample and the Fresnel reflection at the fiber/sample interface. Similar to OPS, the scattered light comes from a small volume whose dimensions are determined by the source's coherence length. Thus, LC-DLS also limits the volume of interaction.

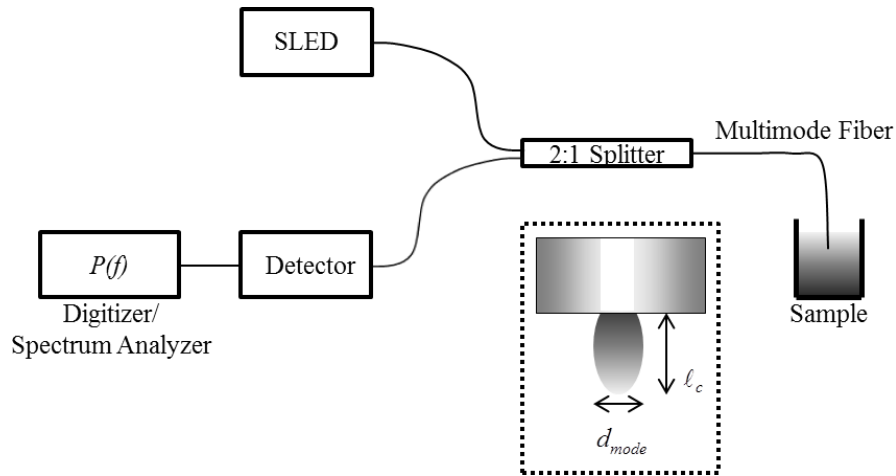


**Figure 10** The low coherence dynamic light scattering (LC-DLS) setup. Broadband light from a super luminescent light emitting diode (SLED) is injected into a fiber splitter and illuminates the sample. Backscattered light is collected by the same fiber and guided to the detector. The detector's photocurrent is digitized by a data acquisition device (DAQ) or the power spectrum is directly calculated with a spectrum analyzer. **Inset** The interaction volume probed by the light at the tip of the fiber. The longitudinal extent of the volume is determined by the coherence length of the light,  $\ell_c$ , and the transverse extent is determined by the field's mode diameter,  $d_{mode}$ .

### *Finding the Field Correlation Function from LC-DLS Measurements*

LC-DLS measures the power spectral density (PSD) of the randomly varying scattered light signal from a medium. Information about the microscopic relaxation processes inside the medium are encoded onto the PSD. This information is only determined after the application of an appropriate model, which often includes some form of *a priori* information. Thus, it is important to keep in mind that, fundamentally, techniques like LC-DLS measure properties of scattered light, *not* material properties. These are inferred after the measurement.

Figure 10 depicts the commonly used fiber-optic based LC-DLS setup. For most experiments, light from a 5 mW, 680 nm center wavelength, fiber pigtailed SLED is injected into a 2:1 50/50 fiber splitter. The jacket of the sample arm of the fiber is stripped and the end of the fiber is cleaved to present a flat interface between the fiber and the sample. The fiber is typically inserted into the sample. Backscattered light is collected through the same fiber and detected with a 200 kHz silicon photoreceiver. The analog signal is typically sampled by a data acquisition device and fed to a computer for further processing. Alternatively, the power spectrum of the photocurrent is computed directly with an electronic spectrum analyzer. The inset of Figure 10 illustrates the extent of the interaction volume probed by this setup. The width of the volume is on the order of the mode field diameter of the fiber, which is about 10  $\mu\text{m}$ , and the length is on the order of the coherence length of the light, which is about 30  $\mu\text{m}$  for the above-mentioned light source. The corresponding coherence volume is on the order of picoliters.

The expression for the PSD may be obtained by first starting with the field incident on the detector. This field may be written as

$$E_{det}(t) = E_0(t) + \sum_j E_s^{(j)}(t) \quad (14)$$

where  $E_0(t)$  is the field reflected from the fiber-sample interface and  $E_s^{(j)}(t)$  is the field scattered from the  $j$ 'th independent region within the interaction volume. By independent region it is meant that the each contribution  $E_s^{(j)}(t)$  to the total scattered field  $E_s(t) = \sum_j E_s^{(j)}(t)$  in Eq. (14) from a volume  $dV_j$  does not depend on any other contribution from a different volume.  $E_0(t)$  is effectively a reference beam in the common-path interferometer. The instantaneous intensity  $I(t)$  is the absolute square of Eq. (14); the intensity autocorrelation function (ACF) is  $G^{(2)}(\tau) = \langle I(t+\tau)I(t) \rangle$ . Here,  $\langle \dots \rangle$  denotes an average over an ensemble of material configurations. One must take special care when analyzing DLS data due to the nature of this average and what is actually determined in experiments, as discussed later.

Assuming that the number of scatterers within the coherence volume is large such that  $\sum_j E_s^{(j)}(t)$  is a Gaussian random variable [18] and removing cross terms that average to zero,  $G^{(2)}(\tau)$  may be expressed as (see **Error! Reference source not found.** for derivation)

$$\begin{aligned} G^{(2)}(\tau) = & I_0^2 + 2I_0I_s + I_s^2 \\ & + I_0 \sum_j I_j \gamma^2(0, j) \left[ g_j^{(1)}(\tau) + g_j^{(1)*}(\tau) \right] + \sum_j \sum_{k \neq j} I_j I_k \gamma^2(j, k) g_j^{(1)}(\tau) g_k^{(1)*}(\tau) \end{aligned} \quad (15)$$

with  $I_0$  representing the intensity of the reference beam,  $I_s = \sum_j I_s^{(j)}$  the total intensity of the scattered light, and  $\gamma^2(j, k) = \exp \left[ -2(s_j - s_k)^2 / \ell_c^2 \right]$  denoting the degree of coherence between

the light scattered from independent regions  $j$  and  $k$  separated by a distance  $s_j - s_k$ .

$g^{(1)}(\tau) \equiv \langle E^*(t+\tau)E(t) \rangle$  is the normalized *field* ACF and is the quantity that best reflects properties of the sample. In most LC-DLS applications, the total amount of light backscattered into the fiber is very small compared to the amount of light reflected off of the fiber tip. This means that the homodyne term in Eq. (15) (the double sum over independent scattering volumes) may be neglected without consequence. Normalizing by  $I_0^2 + 2I_0I_s + I_s^2$  and assuming that the statistics describing the dynamics of each scattering center are the same produces

$$g^{(2)}(\tau) = 1 + \frac{2I_0I_s^{CV}}{(I_0 + I_s^{CV})^2} \text{Re} \left[ g^{(1)}(\tau) \right] \quad (16)$$

which is the normalized intensity ACF. The quantity  $I_s^{CV} = \sum_j I_j \exp \left[ -2(s_0 - s_j)^2 / \ell_c \right]$  is the backscattered intensity that contributes to the interference term in the expression for the total intensity on the detector. Scattering centers significantly farther from the fiber tip than one coherence length contribute very little to this quantity. Finally, the Fourier transform of Eq. (16) provides the PSD of the intensity fluctuations by the Wiener-Khinchin theorem [64].

Eq. (16) is important because it links the measurable quantity—the intensity ACF—to the field statistics, given by  $g^{(1)}(\tau) = \langle E_s^*(t+\tau)E_s(t) \rangle$ . The time dependence of the field ACF may then be linked to the dynamics of the material.

For example, for a monodisperse, dilute suspension of spheres in water, the field ACF is given by

$$g^{(1)}(\tau) = \exp(-q^2 D \tau) \quad (17)$$

where  $q = 4\pi n \sin(\theta/2)/\lambda$  is the magnitude of the scattering vector at scattering angle  $\theta$  and  $D$  is the diffusion coefficient of the spheres [18]. Since  $D$  is inversely proportional to the spheres' hydrodynamic radii [18], Eq.'s (16) and (17), together with the Wiener-Khinchin theorem, allow for the determination of the size of the spheres. This is the principle behind particle sizing using traditional DLS.

DLS is limited in its capabilities by a few factors. As noted, the suspension in traditional methods has to be sufficiently dilute that multiple scattering does not occur. This may be accounted for in some experimental geometries by diffusing wave spectroscopy (DWS) [25], but only after heavy use of *a priori* information. DLS with a low coherence source on the other hand requires no change to the single scattering models and works for many multiply scattering media because the reduced interaction volume suppresses the signal from the multiply scattered light.

Another limitation is that the suspensions must be sufficiently concentrated so that the assumption of Gaussian field statistics is valid. This requirement is known as the Siegert relation and practically means that the number of independent scattering volumes is large enough that the scattered field is described by a Gaussian distribution according to the central limit theorem [78]. If the Siegert relation does not hold, then Eq. (16) is not true and the relationship between the field and intensity ACF's is much more complicated, so much so that it often cannot be modeled. LC-DLS, due to its reduced interaction volume, is most-often limited by this constraint.

Finally, it should be noted that the field and intensity autocorrelation functions,  $g^{(1)}(\tau)$  and  $g^{(2)}(\tau)$  are *ensemble* averages. The measured quantities in a typical DLS experiment, on the other hand, are *time* averages. The equivalence of ensemble and time averages, otherwise known



as ergodicity, must be satisfied for the above treatment to work. For non-ergodic processes, more care must be taken in the data analysis [79] or more refined experiments can overcome this limitation [80].

### *Applications of LC-DLS to Particle Sizing and Motion*

For particle sizing experiments in dilute polydisperse suspensions, Eq. (16) may be expressed as

$$g^{(2)}(\tau) = 1 + \int_0^\infty S(\Gamma) \exp(-\Gamma \tau) d\Gamma \quad (18)$$

where  $\Gamma_j = q^2 D_j$  is the exponential decay rate of a single component of the intensity ACF corresponding to a free particle in suspension with diffusion coefficient  $D$ .  $S(\Gamma)$  is a weighting factor that depends in part on the relative proportion of particles in the suspension with diffusion coefficient  $D$  and also on their scattering cross sections. Curve fitting routines like CONTIN have been developed to extract  $S(\Gamma)$  from a measurement of the intensity ACF [81].

For monodisperse dilute suspensions (particles of a single size), the normalized intensity ACF is written as [18,82]

$$g^{(2)}(\tau) = 1 + \beta \exp(-q^2 D \tau) \quad (19)$$

All of the constant factors here have been assimilated into  $\beta$ , which represents the contrast between the dynamic signal and the static background intensity. The Fourier transform of this

expression is the PSD:  $P(f) = \int_{-\infty}^{\infty} g^{(2)}(\tau) \exp[-i2\pi f\tau] d\tau$ . From Eq. (19), the PSD of intensity fluctuations for a monodisperse suspension of particles is

$$P(f) = \delta(f) + \left( \frac{\beta f_0}{\pi} \right) \frac{1}{f^2 + f_0^2} \quad (20)$$

with  $f_0 = q^2 D / 2\pi$ . The second part of the PSD is a Lorentzian with corner frequency  $f_0$  and an asymptotic log-log slope of -2.

Figure 11 displays three PSD's for suspensions of 1  $\mu\text{m}$  diameter polystyrene spheres in water at 1%, 5%, and 10% concentration by weight. The log-log slope of the curves is -2 and the corner frequency depends on the particle radius  $r$  through the Einstein-Stokes relation

$$D = \frac{k_B T}{6\pi\eta r}. \quad (21)$$

In this expression,  $k_B$  is Boltzmann's constant,  $T$  is the absolute temperature, and  $\eta$  is the viscosity of the fluid. Fitting to Eq. (20) and using Eq. (21) and the corner frequency expression gives particle diameters of 1.1  $\mu\text{m}$ , 1.2  $\mu\text{m}$ , and 1.4  $\mu\text{m}$  for each of the concentrations. The differences between measured and actual sizes are likely due to hydrodynamic interactions between the particles [83,84]. Note that concentrations above 1% are very difficult to obtain correct sizing information with traditional DLS techniques since the signal-to-noise ratio of the singly scattered component is too low. However, the suppression of multiple scattering in LC-DLS allows the experimenter to perform particle sizing in even dense suspensions.

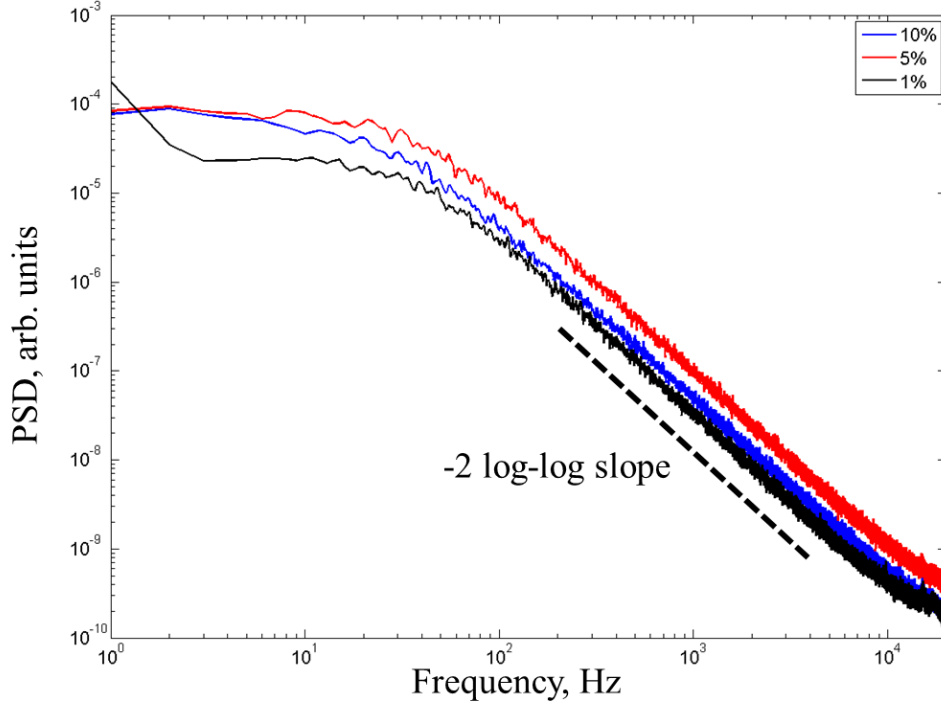


**Figure 11** Power spectral density of the intensity fluctuations from a suspension of 1  $\mu\text{m}$  diameter polystyrene spheres at different weight concentrations. The curves are characterized by an asymptotic log-log slope of -2 and a corner frequency that depends on their size.

For monodisperse suspensions of particles with more complicated dynamics than free diffusion, the intensity ACF becomes [18]

$$g^{(2)}(\tau) = 1 + \beta \exp\left(-q^2 \langle \Delta R^2(\tau) \rangle / 6\right) \quad (22)$$

with  $\langle \Delta R^2(\tau) \rangle$  representing the mean squared displacement (MSD) of a single particle. This expression could have been guessed from Eq. (17) and the well-known result from the theory of Brownian motion,  $\langle \Delta R^2(\tau) \rangle = 6D\tau$ . Diffusive processes in which the MSD grows nonlinearly in time are described as anomalous [85]. In these cases, the MSD typically grows like a power law

$\langle \Delta R^2(\tau) \rangle \sim \tau^\alpha$  with  $\alpha < 1$  denoting subdiffusion and  $\alpha > 1$  denoting superdiffusion. If this is true, then the asymptotic form of the PSD will be

$$P(f) \sim \frac{1}{f^{\alpha+1}} \quad (23)$$

which means that  $\alpha$  is revealed by the log-log slope of the data. This is shown in Figure 12 for 0.098  $\mu\text{m}$  diameter polystyrene spheres in a 100,000 molecular weight PEO and water solution. The slope of the PSD is greater than -2, which signifies a value for  $\alpha$  that is less than 1. The physical reasoning for this change is that the PEO polymer chains cage the microspheres and limit their diffusive motion, which leads to subdiffusion.

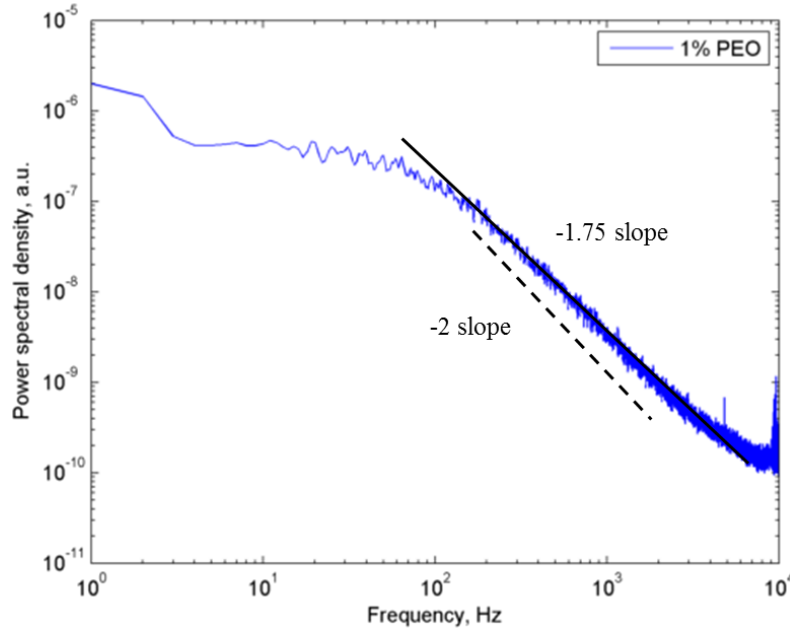


**Figure 12** Powerspectral density of intensity fluctuations measured with LC-DLS from viscoelastic media. The sample is a suspension of 0.098  $\mu\text{m}$  diameter polystyrene microspheres in 100,000 molecular weight PEO solutions at 1.0% wt. concentration. The asymptotic log-log slope of the PSD is greater than -2, which indicates that the power law exponent for the particles' MSD is less than one. Compare this to the figure from reference [86].

### *Optical Microrheology of Complex Fluids*

LC-DLS was used to explore several properties of complex fluids, such as their viscoelasticity (see the **Error! Reference source not found.** for a brief introduction to this microscopic mechanical property). One complex fluid in particular was investigated: a solution of water and a triblock copolymer known as Pluronic. The viscoelasticity of Pluronic, which exhibits intricate phase behavior over a relatively small temperature range (20°C to 70°C), is particularly troublesome to investigate at high shear rates due to the limitations of mechanical rheometers [87]. Additionally, light scattering microrheology experiments employing diffusing wave spectroscopy (DWS), a DLS technique that incorporates multiple scattering into the data analysis, necessarily requires large sample volumes [88,89]. Thus, any type of local viscoelasticity measurement on Pluronic is precluded in DWS. Finally, the Pluronic itself exhibits strong scattering at certain temperatures. This means that the traditional method of extracting the viscoelasticity from the tracer particle motion by using the generalized Stokes-Einstein equation cannot be applied [90].

LC-DLS measurements on picoliter volumes provided local viscoelastic data on this important polymer for the first time. The behavior in the PSD of the backscattered intensity fluctuations may be seen in Figure 13.

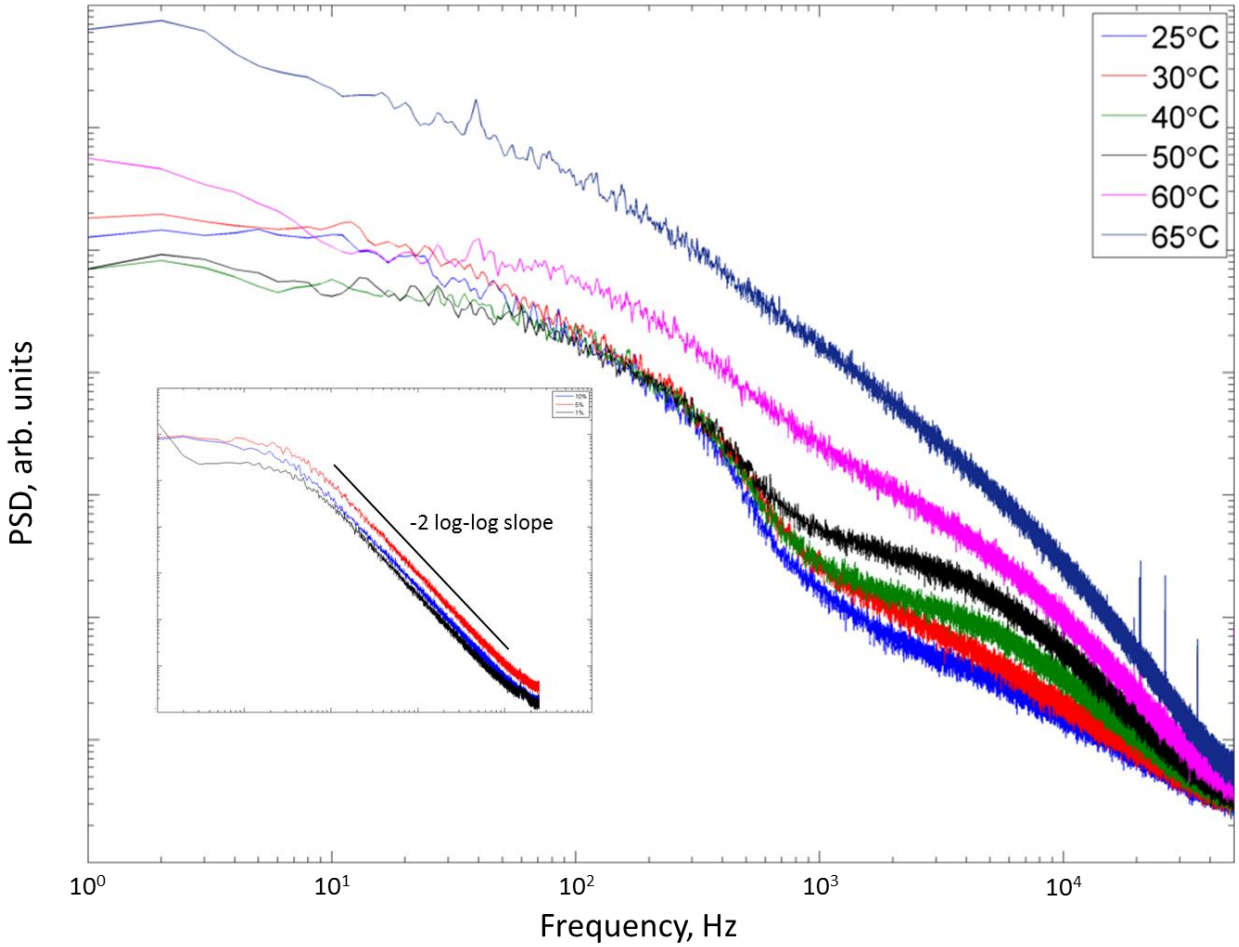


**Figure 13** PSD of the backscattered intensity fluctuations from a 10% Pluronic L64 solution in water seeded with 1% wt., 1.0  $\mu\text{m}$  diameter polystyrene spheres. The curves represent data taken at the noted temperatures. **Inset** PSD's from suspensions of 1.0  $\mu\text{m}$  diameter polystyrene spheres in water at 1%, 5%, and 10% weight concentrations are provided as a reference. The PSD for this simple colloid is a Lorentzian whose shape is independent of temperature.

The complex behaviors of the PSD curves at certain temperatures do not fit any traditional models. Figure 14 displays an analysis of a few of these PSD's from a solution of 10% Pluronic L64 in water (Figure 14 (b) also contains 1  $\mu\text{m}$  diameter polystyrene microspheres as tracers at 1% concentration by weight). At 25°C, the PSD from the solution is the same as a PSD from a dilute suspension of independent spheres with a radius of 0.13  $\mu\text{m}$ . However, at higher temperatures, the low-to-mid frequency roll off (100-1000 Hz) is analogous

to free particle diffusion described by a MSD that scales with a time exponent of 2.5. This is not physical for free particles, so another mechanism must be responsible for the fast roll off. The high frequency behavior of the PSD's in Figure 13 is from the Pluronics itself, not the tracer particles.

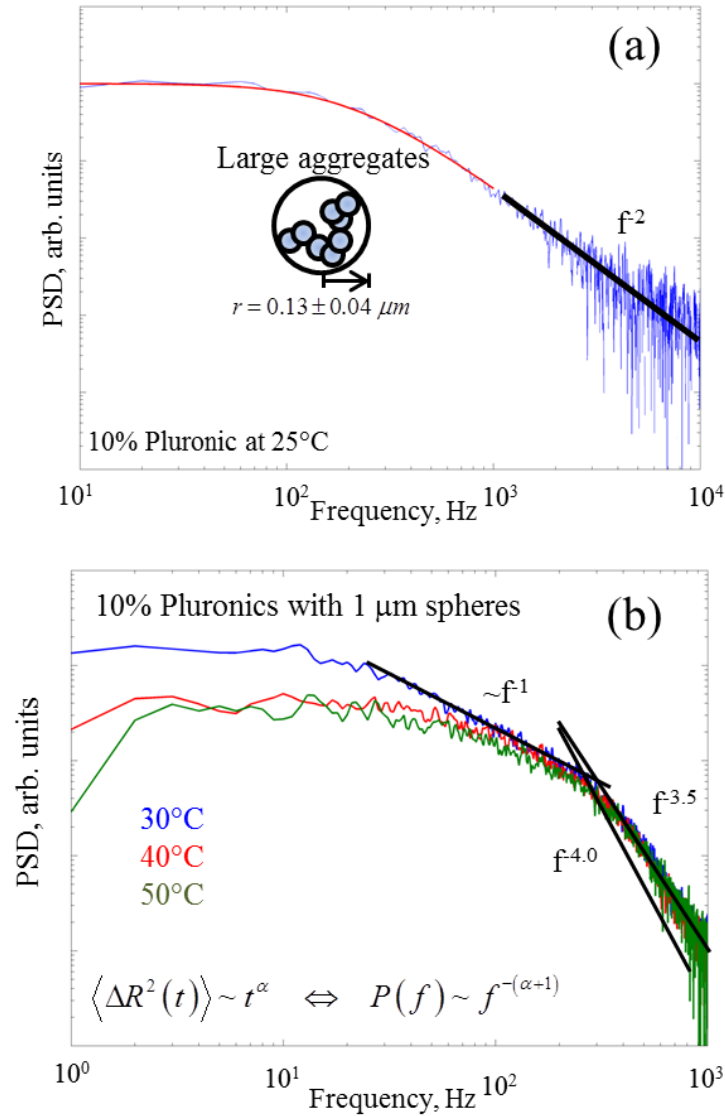


**Figure 14** Analysis of the Pluronics data. a) At 25°C, 10% Pluronics L64 in water contains signatures of bulk polymer with a hydrodynamic radius of 0.13  $\mu m$ . b) At larger temperatures, the PSD experiences an initial slow decay, followed by a fast rolloff. The slope of the PSD suggests a mean squared displacement that grows with time exponent of 2.5. Since this is not physical for freely diffusing particles, some other mechanism must be causing this behavior.

Another fluid system with complex microrheological properties is human blood. The work with human blood comes from the need for surgeons to measure clotting times during interventional surgery and of doctors for treating a range of cardiovascular diseases that are related to blood's viscoelasticity [91]. In this case, localizing the volume of interaction with LC-DLS is important for creating a minimally invasive catheter that can be inserted into an artery or vein at a specific site inside the body. External methods for measuring blood flow, such as laser speckle velocimetry [92], are limited to velocity measurements near the surface. However, LC-DLS obtains full viscoelastic data from the light that's scattered by the red blood cells in the blood at any location that the catheter can reach.

As an example of this capability, Figure 15 displays viscoelastic data measured with the LC-DLS fiber probe and a mechanical rheometer from different human blood samples. After being drawn from a patient, each sample was split into two parts. One part was inserted into a blood rheometer as would be commonly found in an operating room. It measured the activated clotting time (ACT) of the sample, which is the time it takes for a clot to form after being induced. The y-axis displays the loss tangent, which is a quantity that is derived directly from the signal measured from the fiber probe. (Mathematically, it is the ratio of the imaginary part of the viscoelastic modulus to the real part. See **Error! Reference source not found.**) The figure displays a good correlation between the measured signal and the ACT derived from the rheometer measurement. Importantly, the rheometer required several minutes to work whereas the light scattering-based measurement took only seconds.



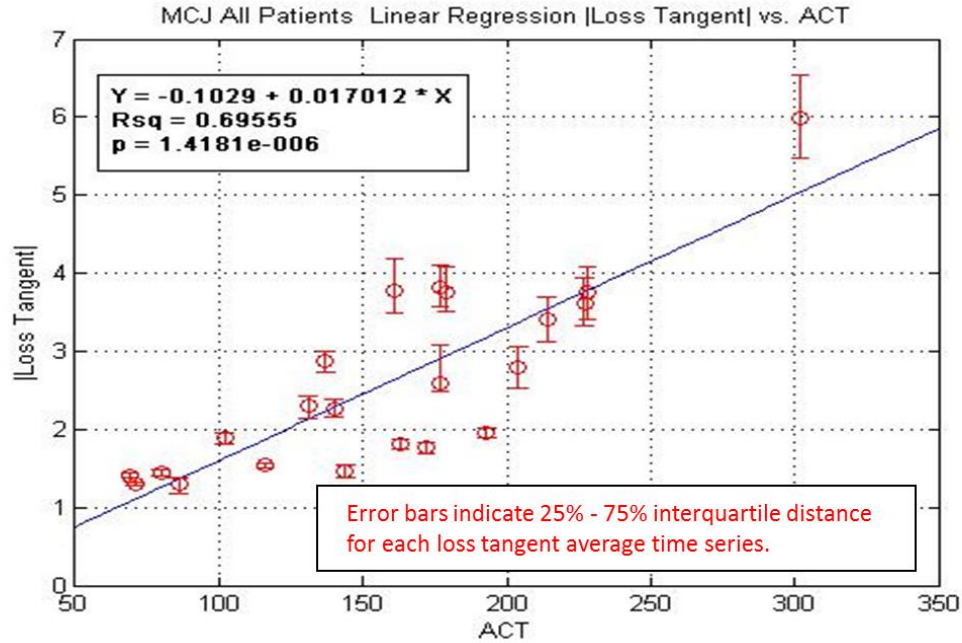


**Figure 15** Blood viscoelasticity vs. the activated clotting time (ACT). There is a correlation between the ACT, which is the average time it takes for an induced blood clot to form, and the viscoelastic response measured by the instrument. The loss tangent is the ratio of the imaginary part of the viscoelastic modulus to the real part.

There remain open-questions as to the application of the model of independent tracer particle motion to a fiber-based LC-DLS measurement of blood viscoelasticity. First, are the red blood cells, which contribute most to the optical signal, truly passive and independent Brownian probes of their viscoelastic environment? Due to their large concentration within the blood, the answer to this question is likely to be “no.” Second, is the interaction volume large enough to measure from many statistically-independent regions within a sample of blood? This question is relevant because of the large size of red blood cells, which is about 5  $\mu\text{m}$  in diameter. Given the large size and high concentration of scatterers in the blood, the pure Brownian motion of independent particles is likely not an accurate model for discerning absolute parameters of the blood viscoelasticity.

Despite these issues, this simplified model still retains some use. The PSD of the scattered light fluctuations within the model's context is well understood and follows its predicted behavior. Furthermore, at frequencies larger than a few thousand Hertz (times shorter than about a millisecond), the red blood cells have not moved enough to significantly affect one another's movement. This fact, coupled with the rejection of the multiply scattered light by the coherence gating effect, allows for application of the independent Brownian particle model at these frequencies. Finally, (unpublished) trials on controlled samples of whole blood have revealed a strong correlation between the measured viscoelastic moduli and the blood's activated clotting time, an important quantity for describing the rate of coagulation [91]. Figure 15 contains some of the results from these trials. Thus, so long as one does not require measurements of the absolute values of the viscoelastic moduli, then one can determine the clotting rate of a blood sample quite well.

### Conclusion

LCI is a useful diagnostic technique for probing the structure and dynamics of multiply scattering random media. Most models that link scattered light to material information require the sample to be singly scattering, rendering multiply scattering media difficult to characterize experimentally. LCI takes advantage of the short coherence length of the light source to reduce the size of the light-matter interaction volume in such a way that multiple scattering cannot obfuscate the optical signal. In this chapter it was demonstrated how LCI can be used to eliminate the required knowledge about the boundary extrapolation length from the determination of a medium's photon diffusion coefficient. It also facilitated DLS measurements

for both particle sizing and microrheology of complex fluids. Since most of the described setups make use of fiber optics, the interferometers are inexpensive, compact, and do not require alignment. Furthermore, the common path interferometer used for probing complex fluids is not subject to phase noise and is easily implemented into existing hardware, like catheters and endoscopes.

## CHAPTER 3: MODELS FOR MESOSCOPIC OPTICS

Modeling a mesoscopic system is often difficult because the properties of the system change with the size or duration of the volume of the system that is probed. Still, one can employ some general theories, like that of diffusion, to explain the results of measurements that are performed on a number of disparate systems, such as disordered photonic lattices and biological cells. In this chapter, models for explaining the scale-dependent behavior of these systems are presented along with the experiments that helped generate them.

### Determining Anisotropic Cell Motility on Curved Substrates

Cell motility, or motion, is driven in large part by mechanical cues from the extracellular environment [93,94]. Forces are exerted to and from the extracellular matrix to the cytoskeletal filaments through contact points known as focal adhesions. Recent work has found that the geometry of the extracellular environment plays an important role in cell morphogenesis and that this role is likely facilitated by the mechanical coupling between a cell and its surroundings [95].

Exploring cell motility and testing hypotheses from cell mechanics requires novel optical tools and models. This is partly because there are difficulties with live cell imaging that are not usually encountered in other optics setups. Unlike inanimate samples, cells must be maintained in a state similar to their natural one within the body. Otherwise, they die or act in ways that are not relevant. In addition, the large and random behavior of cells requires statistical methods and tools that are capable of recording a large number of them at once. Sometimes the live environment precludes a way to image a large number of cells clearly, especially if the environment is three dimensional.

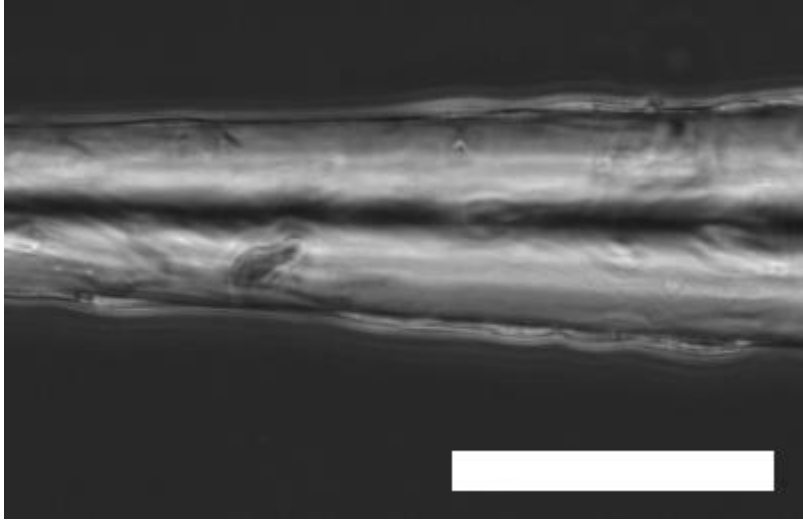
Such was the case for our study of Schwann cells. The goal of the study was to determine the effect of the radius of curvature of the substrate on their motion. Schwann cells (glial cells of the peripheral nervous system) are responsible for coating axons in the myelin sheath. Degradation of the myelin sheath leads to a range of diseases, most notably multiple sclerosis. Knowledge of how Schwann cells move on an axon is therefore needed to understand the myelination mechanism and how it may fail. The question that was addressed in this project was the following: to what extent does the radius of curvature of the substrate affect Schwann cell motility?

#### *Difference Imaging for Determining Anisotropic Motility*

To this end a method for extracting directionality of moving objects from a series of low contrast and poorly resolved images was developed. Specifically, an image processing technique for determining whether a large number of cells moved preferentially along one of two directions perpendicular to each other was created. The important directions in the experiment corresponded to those parallel and perpendicular to the axis of a tapered quartz glass fiber that was covered in motile Schwann cells.

A typical 10x phase contrast image of these cells is seen in Figure 16. The nonuniform background light intensity through the fiber, the limited depth of field, and the inherently poor contrast of the cells ruled out the use of conventional single-cell tracking algorithms [96]. For instance, noise in popular image correlation analyses is multiplicative, so objects require a high contrast to be tracked [96]. Importantly, the quartz fiber itself distorted the images of cells that lay on it. These issues made it impossible to determine the motion of any one cell with traditional

cell tracking algorithms. Therefore, a technique that works by examining the dynamics of a large number of cells at once in poor imaging environments was developed.



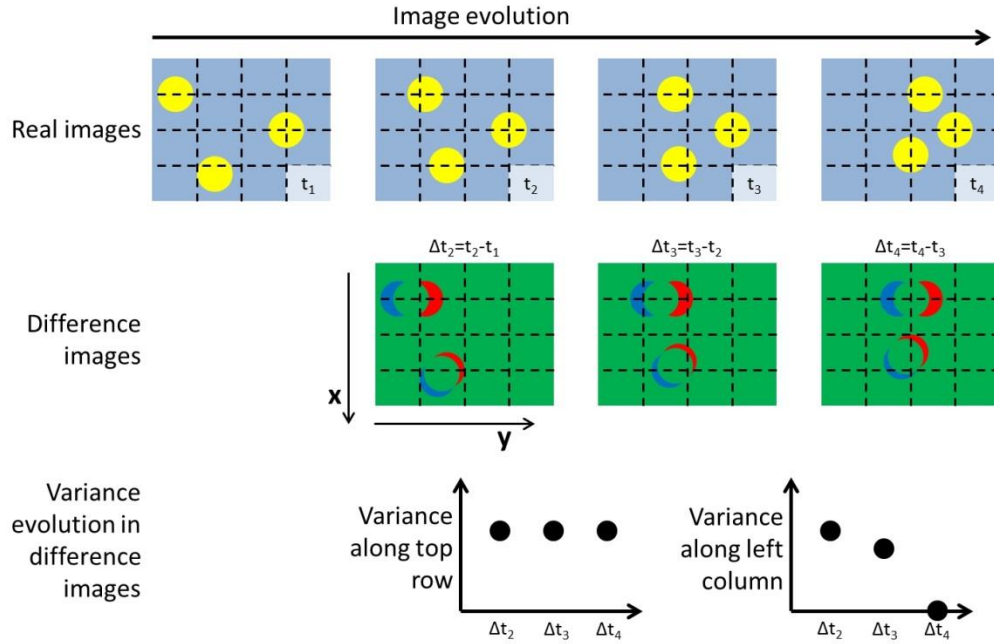
**Figure 16** Primary rat Schwann cells move on a quartz fiber. The image was taken with a phase contrast microscope. The microscope's limited depth of field and the cells' poor contrast prevents the use of single-cell tracking algorithms for extracting the statistical information about their motion. Scale bar: 100  $\mu\text{m}$ .

Figure 17 illustrates the new algorithm that was developed to process the images. Images were taken of motile cells at times  $t$  spaced by an interval  $\Delta t$  (ten minutes in the experiments). These cells are depicted by the yellow objects in the top row of Figure 17. Then, the intensities in the pixels of an image at time  $t$  were subtracted from the corresponding intensities in an image at time  $t + \Delta t$ , yielding a difference image. Mathematically, this is represented by

$$D(i, j; t; \Delta t) = I(i, j; t + \Delta t) - I(i, j; t) \quad (24)$$

where  $D$  is the difference image and  $I$  is the intensity in pixel  $(i, j)$  at time  $t$ . The features in the difference images contain information about 1) cells that moved, 2) cells that changed shape, and 3) cells that appeared or disappeared from the field of view. Since the cells that were observed

moved faster than they changed shape, cell motion was the major contributor to the features in the difference images.



**Figure 17** Pictorial description of the processing steps for determining preferred direction of motion. Top row: a series of images containing moving cells (yellow dots) is captured from the microscope. Middle row: successive images are subtracted from one another. Changes between the images are encoded onto the intensity values of the pixels (here marked by different colors). Bottom row: the variance of the intensities along a row and column is determined. The behavior of this variance in time reveals characteristics about the motion of the cells.

A number of statistical parameters concerning the dynamics of a scene can be extracted from the difference images through a judicious choice of processing steps or calculations. For example, difference imaging has been used to extract information about the Brownian motion of unresolved particles and the motility of *E. Coli* bacteria in suspension [27,97]. In our specific case, the advantage of analyzing the difference images is two-fold: the static background intensity was eliminated, leaving only the dynamics of the scene, and a large number of cells could be analyzed at once.

The new contribution to difference image analysis goes as follows. With reference to Figure 17, the variance of the pixel intensities across each row and column of the difference images was determined. The variance of a single row  $i$  in the difference image is given by

$$V(i; t, \Delta t) = \frac{1}{N-1} \sum_{j=1}^N [D(i, j; t, \Delta t) - \bar{D}(i; t, \Delta t)]^2 \quad (25)$$

with  $N$  representing the number of columns indexed by  $j$  and  $\bar{D}(i; t, \Delta t)$  is the mean intensity in row  $i$ . A similar calculation produces the variance over all columns,  $V(j; t, \Delta t)$ . Each of these quantities is a vector of data  $M$  or  $N$  units long, with  $M$  the number of rows and  $N$  the number of columns, depending on the direction that the variance is taken across. The variance operation in this sense is a projection of the data onto one of two orthogonal bases.

The evolution of the variance of pixel intensities in time contains the information pertaining to any preferred direction of motion for the cells. For example, the top object moving uniformly from the left to the right in the real images in the top row of Figure 17 generates the two red and blue “moon” shapes in the difference images (the middle row). The variance calculated for *rows*  $V(i; t, \Delta t)$  containing the top object in the real images of Figure 17 will remain constant across all of the difference images because the object moves uniformly and horizontally. However, the variance of the pixel intensities calculated across the *columns* of the difference images will fluctuate in time as the object moves from the left to the right. Thus, the fluctuations of the variance allow one to infer information about the directionality of a cell without tracking it.



This evolution is illustrated in Figure 18 and was obtained from a simulation of cells on a 2D substrate moving randomly according to Brownian motion. The standard deviation of their step sizes between frames in the x-direction was 5 pixels and in the y-direction was 1 pixel. The top plot is the variance of each row of the difference images vs. frame number ( $t + \Delta t$ ). Red colors denote higher values for the variance, green colors mid-range values and blue colors denote lower values. Clear differences for this anisotropic random walk can be seen between the two variance vs. time (VT) plots. Quantifying these differences and relating them to the anisotropy in the model is the primary objective.

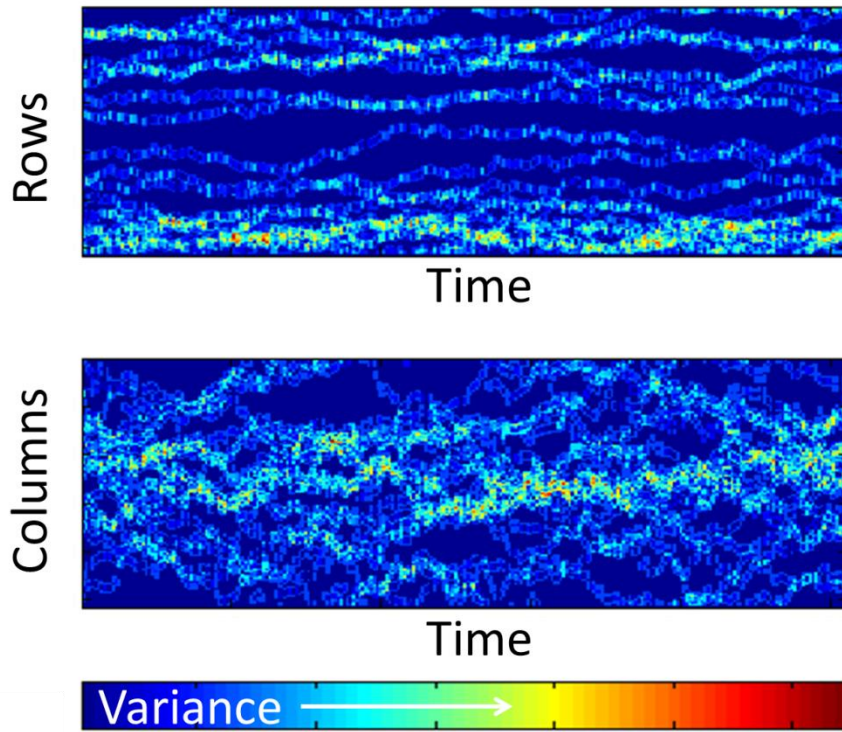


**Figure 18** Evolution of the variance for simulated cells calculated across rows (top) and columns (bottom). At each time step, simulated cells could move randomly in the x-direction with step sizes drawn from a Gaussian probability distribution function with a standard deviation of 5 pixels. In the y-direction, the step sizes were also Gaussian but with a standard deviation of 1 pixel. Because the cells move greater distances (and are more likely to move) in the x-direction, the features in the top graph, known as a variance vs. time (VT) plot, are different than the bottom one. Quantifying the differences between the two plots leads to determining the anisotropy of the motion.

### *Measuring Schwann Cell Motility on Fibers*

The question that was central to this work was whether a curved surface could force cells to move preferentially in one direction instead of another. To answer this question, Schwann cells were observed moving on tapered optical fibers of varying radii and the above technique was applied to extract information about their preferred direction of motion.

First, quartz optical fibers were tapered from their standard radius, about 63  $\mu\text{m}$ , to a radius of about 10  $\mu\text{m}$  over lengths spanning a few hundred  $\mu\text{m}$ . This step was performed with a micropipette puller (Sutter Instruments P-2000) and usually resulted in a large spread in minimum diameters and taper lengths.

The fibers were sterilized by immersing them in 80% ethanol and 20% water for 20 minutes and then irradiating them with UV light for 15 minutes. Following sterilization, the fibers were immersed in solutions of 200  $\mu\text{g/mL}$  poly-L-lysine and 25  $\mu\text{g/mL}$  laminin for one hour each to promote attachment of the cell's focal adhesions to the fiber. After this, the fibers were rinsed with phosphate buffered saline and Dulbecco's modified essential medium with 10% heat inactivated fetal bovine serum (known as D10). They were then transferred to the center of a 60 mm uncoated tissue culture dish filled with 500  $\mu\text{L}$  of D10 and seeded with about 1000 primary rat Schwann cells. After 24 hours, the Schwann cells had attached and the medium volume was increased to 2 mL. The dish was placed on a Zeiss Observer Z1 widefield microscope with an onstage incubator maintained at 37  $^{\circ}\text{C}$  with a 5% humidified  $\text{CO}_2$  atmosphere. Phase contrast images were acquired every 10 minutes for 18 hours with a 10X Zeiss EC Plan-Neofluar objective and a Hamamatsu ORCA R2 camera. The light source was a 100 W halogen bulb with appropriate heat filters.

Five positions on two separate fibers were monitored during the observation period. The plane of focus was set to the top of the fiber's surface as judged by eye. Each image in the series for one position was digitally registered such that the same pixels contained the center of the fiber in each image, eliminating any effects of stage drift in the difference images.

The images were first converted to 8-bit grayscale before successive images were subtracted from one another. A series of  $N$  images produced  $N-1$  difference images. The pixel intensities of the difference images were scaled to the range [0-255] such that no change in intensity corresponded to a pixel value of 127. The variance of the pixel intensities along each row and column were calculated according to the process explained above. Two, two-dimensional maps of the variance of the pixel intensities vs. time (VT plots), one for the rows and one of the columns of a series of difference images, were generated as indicated above. The motion of a large number of cells predominately along a horizontal or vertical direction was indicated by the presence of predominantly horizontal "tracks" in the corresponding VT plot. The decay rate of the horizontal autocorrelation of the VT maps was an indicator of the degree of directed motion of the cells in one direction relative to another.

As noted above, movies of Schwann cells were recorded along two different tapered quartz fibers in the same Petri dish for 18 hours. Images were taken of six regions at 10 minute intervals. The fibers in the observed regions had radii of curvature of  $9 \pm 2$ ,  $12 \pm 2$ ,  $17 \pm 2$ ,  $36 \pm 4$ ,  $46 \pm 5$ , and  $63 \pm 4$   $\mu\text{m}$ . Based on the time evolution of the variance of the pixel intensities in the difference images, it was found that the Schwann cells move preferentially in directions parallel to the axis of the cylindrical substrate for radii of curvature less than or equal to 46  $\mu\text{m}$ , with this preference increasing as the radius of curvature decreases. Schwann cells on the

cylinder with a radius of curvature of 63  $\mu\text{m}$  displayed no preferential direction of motion. In other words, the Schwann cells moved isotropically, i.e. they moved as if they were on a flat surface for substrates with radii of curvature equal to (and presumably greater than) 63  $\mu\text{m}$ .

Assuming that the cells' displacements between successive images along two, independent directions (parallel and perpendicular to the cylinder's axis in this case) were normally distributed, it was concluded that the upper bound on the root-mean-square (RMS) step size of the Schwann cell movement along the fiber's axis was  $45 \pm 2 \mu\text{m}$  per hour (0.75  $\mu\text{m}/\text{minute}$ ). Visual observations indicate that the RMS step size along the axis does not change with the fiber's decreasing radius of curvature. This is also the RMS step size in directions perpendicular to the axis when the cells' motion has become isotropic. This upperbound was determined with help from the simulations (see Appendix C), in which it was discovered that the RMS step size between consecutive frames when the motion becomes isotropic is roughly half the average cell length. The size was determined by averaging over about one hundred cells' long and short axes, which produced a value of  $15.0 \pm 0.7 \mu\text{m}$ .

#### *Discussion of the Observations and their impact on Cell Motility Studies*

The speed of the cells that was inferred is comparable to speeds reported for Schwann cell motility on purified extracellular matrix cables [98] and on cultured sensory neuron axons [99]. In the former report, investigators measured Schwann cell motility on both purified fibronectin cables with diameters of 50-100  $\mu\text{m}$  and on mixed fibronectin/fibrinogen cables with diameters of 200-250  $\mu\text{m}$ . They observed that the rate of migration was dependent on the concentration of fibrinogen in the mixed cable and varied between 0.3  $\mu\text{m}/\text{minute}$  to 0.8

$\mu\text{m}/\text{minute}$  on 50:50 fibronectin/fibrinogen cables. On sensory neuron axons, Schwann cells migrated at  $0.2 \mu\text{m}/\text{minute}$  [99] just below the lower limit reported for the fibronectin/fibrinogen cables. The slower speed of migration of Schwann cells on sensory axons reflects the actual biological process that is influenced by a number of factors, including interaction with diverse types of cell adhesion molecules expressed on the axon's surfaces, difference in surface rigidity, and topography of the axon. This complexity of interactions and processes which must be integrated by the cell is not comparable to activation of a single type of receptor, the integrins that mediate motility on the purified laminin and fibronectin substrates.

Results of previous works allow us to speculate on the cause of the observed anisotropy of the cells' motion. Fluorescence micrographs of fixed fibroblasts and epitheliocytes on cylindrical substrates revealed a preferential alignment of actin microfilament bundles either parallel or perpendicular to the axis of the underlying cylinders [100]. It was later determined that polarized cells such as fibroblasts tend to exhibit actin microfilament bundles aligned parallel to the axis of the underlying cylindrical substrate, whereas discoid epitheliocytes showed alignment perpendicular to the axis [101]. On flat surfaces, the discoid cells displayed no preferential alignment of their actin microfilament bundles. Continuum models of the stress on cytoskeletal filaments and whole cells on curved substrates corroborates these ideas [102,103]. Since actin is a key component in the motility process, it is possible that the resulting alignment of the actin filaments due to the substrate curvature is a cause of the anisotropic motion.

Determination of the minimal radius of curvature that directs anisotropic motility should facilitate investigation of the molecular pathways for sensing and responding to this physical constraint. Surprisingly, other studies have uncovered specific pathways essential for different

aspects of motility. For instance, the ENA/VASP protein impacts the speed of migration by controlling lamellipodial dynamics [104], and the function of phospholipase A2 and phosphoinositide-3-kinase are essential for chemotaxis but not for general motility in *Dictyostelium* [105]. Sensors and pathways essential for changing from isotropic to anisotropic motility based on the radius of curvature can be uncovered by analyzing migration of Schwann cells in the presence of specific inhibitors and confirmed by assessing migration of Schwann cells lacking expression of specific receptors, kinases and cytoskeletal modifying proteins.

Another application for this work would be its use in cell motility assays on non-glial cells. It would be notable to determine if other cell types would show the same preference for motility on curved substrates. Quartz optical fibers are relatively inexpensive and are offered commercially in a variety of types and sizes. Directionality of different cell types can be explored easily and cheaply, especially since no microscopes with abilities beyond phase contrast imaging or fluorescence labels are required. The added benefit of injecting light into the fibers is currently being explored by our group and promises future advantages for sensing motile cells.

This work corroborates many theoretical and numerical findings about the stress in the cytoskeleton on curved surfaces and experimental work on actin fiber alignments [100,102,103]. Specifically, it is thought that cells move easiest along directions that minimize the stress in the cytoskeleton. This conclusion was reached by analyzing cellular motion across a range of curvature scales and in a large field of view. Here, the scale-dependent behavior is not actually the light-matter interaction, but rather the motility of the cells.

### Anomalous Transport of Light in Partially Disordered Photonic Crystals

The propagation of light in a disordered medium is commonly described as a random walk of photons with an average step size given by the transport mean free path  $\ell^*$  [1,29]. This picture interprets the light as tiny particles that diffuse through the medium and not as a wave that carries energy.

Though useful for many applications, such as biomedical imaging, the random walk model does not explain some behaviors of light in multiply scattering systems, such as enhanced backscattering and the correlation functions in the scattered field that arise from short, medium, and long range effects [2,106,107]. These effects are ascribed to interferences inside the material which are due to the wave-like nature of light. Another wave interference effect is Anderson localization, whereby the energy in a wave can be trapped inside the material due to scattering and constructive interference alone [108]. Though originally formulated to explain the metal-to-insulator phase transition for electronic conduction in solid-state systems, Anderson localization was later extended to light inside dielectric superlattices (i.e. photonic crystals) by John [9,109].

Disordered photonic crystals are intriguing systems in which to study optical localization phenomena because the degree of disorder within them may be tuned. By the term disorder here it is meant that there exist variations in the unit cell structure, size, or refractive index and that these depend on the location inside the “crystal.” Strictly speaking, this kind of photonic crystal is not a crystal anymore, but since, from a macroscopic viewpoint, there is still a significant periodic component to the structure’s refractive index, the term crystal will be retained to describe these systems.

Scattering from periodic variations of a material's dielectric function is deterministic. On the other hand, the random variations in the photonic crystal's structure cause some of the light to be scattered randomly. The interplay of order and disorder in these systems essentially means that there is a competition between structural components in their contribution to the total light scattering mechanism, namely, deterministic Bragg resonances or random refractive index fluctuations.

The study of light propagation in disordered photonic crystals is particularly important because any real, fabricated device containing a photonic crystal will suffer from some sort of imperfection. Recently, it was found that a small amount of disorder, not too much and not too little, is sufficient to induce the localization of light [34,110]. However, these optical phenomena have been observed only in transmission, which enforces a minimum length scale upon the light-matter interaction. The evolution from localized to propagating modes within the same material has not been observed. In reflection, only the enhanced backscatter effect of light, a form of weak localization, has been reported.

To better understand the localization phenomena and optical transport in disordered crystals, such systems were analyzed with OPS and a model based on the scaling theory of localization was developed to interpret the results [63,111]. Namely, evidence for the continuous renormalization of the diffusion coefficient of light was found. This conclusion was enabled in part by the measurement apparatus and also because mesoscale thinking connected the observations with a good model.



### *Photon Path Length Distributions in Disordered Photonic Crystals*

As described above in the section entitled Measuring Photon Diffusion Coefficients Independently of Boundary Conditions, OPS employs low coherence interferometry to obtain the path length distribution of the photons' random walk inside a multiply scattering material [60]. Importantly, it obtains this distribution in reflection. As a result, each path length corresponds to an average volume of interaction between the light and the material (see Figure 19). This is unlike a path length or time-resolved transmission measurement in which the size of the material acts as a low path length cutoff.

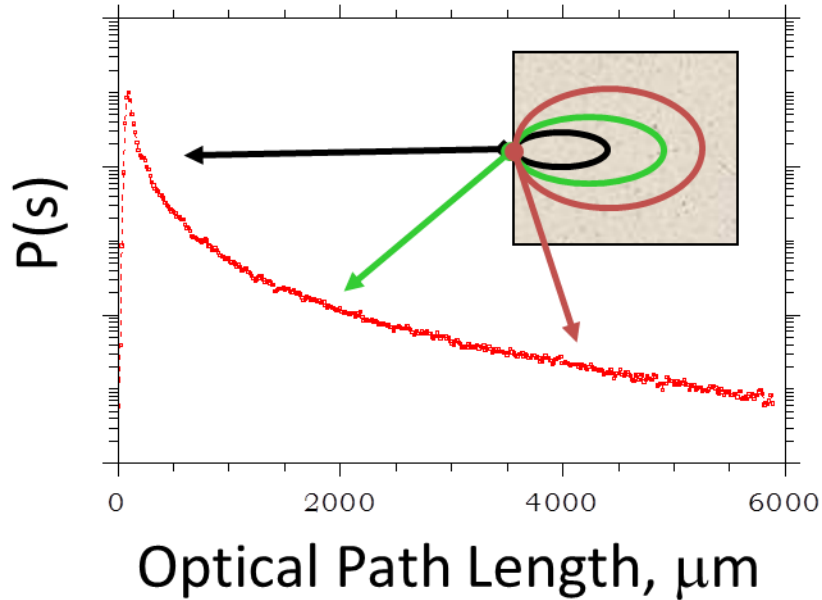


**Figure 19** The path length distribution of light as measured by OPS from a multiply scattering medium. Different path lengths in the signal correspond to different volumes for the light-matter interaction.

Partially disordered photonic crystal were examined using OPS with two different low coherence sources: SLED's with center wavelengths at 1300 nm and 1550 nm [63]. This particular photonic crystal, in the absence of disorder, would have exhibited a 3D bandgap at 1550 nm. However, the disorder opened the bandgap and allowed light at this wavelength to

propagate inside the material. 1300 nm light was chosen as a control since the nature of the crystalline structure had a minimal impact at this wavelength. In other words, the photonic crystal acted entirely as a random, multiply scattering medium for 1300 nm light.

Figure 21 displays the path length distributions obtained from the partially disordered photonic crystal at the two wavelengths. Notably, a slower decay is observed at  $\lambda = 1550$  nm. This decay is explained by the scaling theory of localization. The scaling theory of localization describes the optical transport with a renormalized diffusion coefficient according to

$$D = D_0 \ell^* \left( \frac{1}{\xi} + \frac{1}{L} + \frac{1}{L_{abs}} \right) \quad (26)$$

with  $D_0$  the diffusion coefficient in the absence of renormalization,  $\xi$  a cutoff length scale for renormalization effects,  $L$  the thickness of the material/photonic crystal, and  $L_{abs}$  the absorption length. The effects of all three length scales act to reduce the diffusion coefficient. Typically, the material thickness  $L$  is fixed, but in OPS, where each path length corresponds to different interaction volumes,  $L$  may be taken as a function of path length,  $L \sim \sqrt{6Dt}$ . This idea is illustrated in Figure 20.

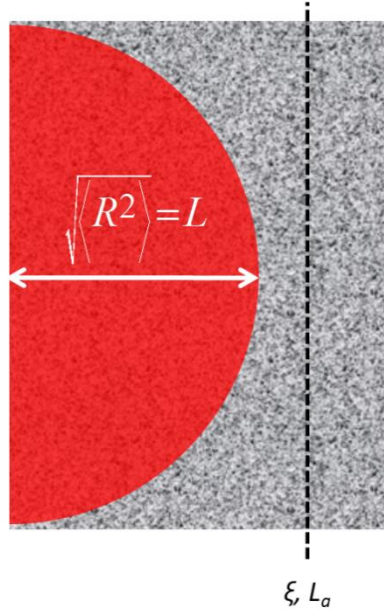


**Figure 20** Light diffusing in a disordered material. In reflection, the interaction volume is equivalent to the volume that an infinitesimally short pulse of light has spread to in a finite time, which is related to the mean squared displacement of the light. Cutoff and absorption length scales,  $\xi$  and  $L_a$ , for the diffusion process exist. When the volume occupied by the energy reaches these scales, the diffusion process reverts from an anomalous one to a normal one.

Substituting this expression for  $L$  in Eq. (26) and letting the other two length scales go to infinity leads to  $D \sim t^{-1/3}$ , which means the photon diffusion coefficient is time-dependent. As described in the next section, this has the consequence that the path length distribution will display a -2 log-log slope, rather than the expected -2.5 log-log slope seen in normally diffusive media [63]. For path lengths greater than the cutoff length scale  $\xi$  and the absorption length, the photon diffusion equation predicts that the path length distribution should begin to decay exponentially, which is observed in Figure 21 for path lengths greater than about 600  $\mu\text{m}$  (note that the photonic crystal was only about 10  $\mu\text{m}$  thick!).

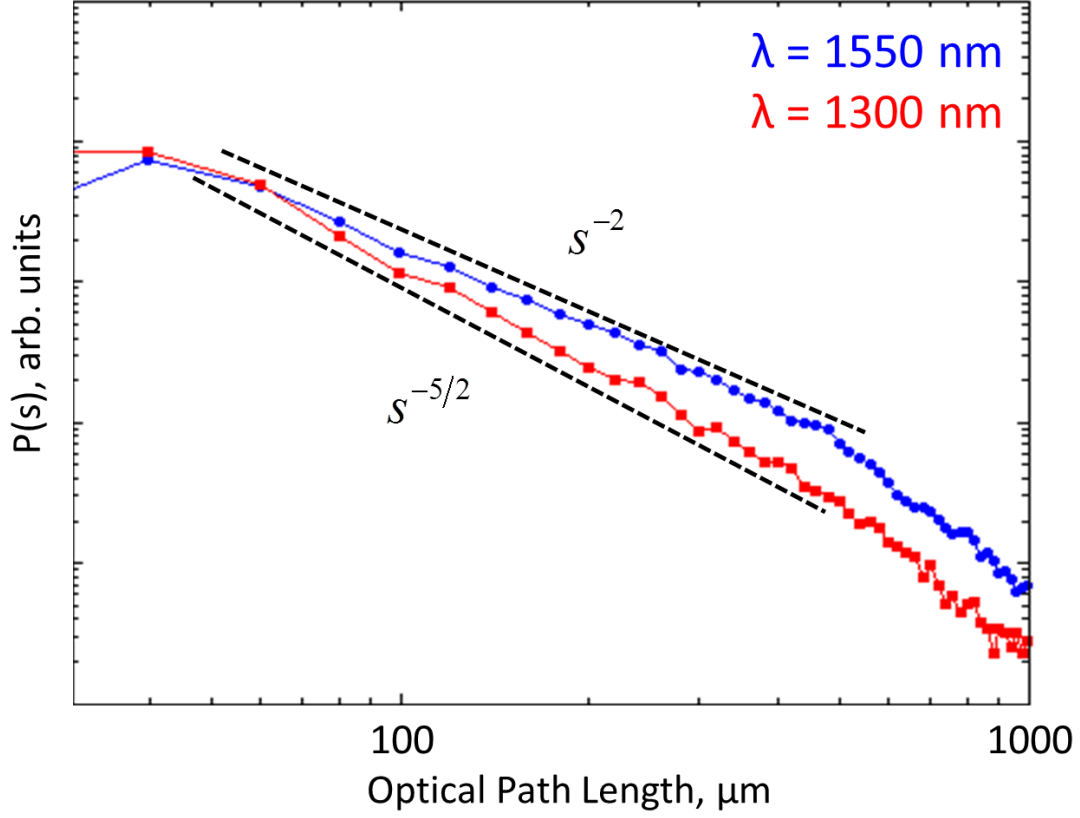


**Figure 21** Path length distributions from the partially disordered photonic crystal at the two wavelengths indicated. The -2 log-log slope is explained by the scaling theory of localization and indicates an anomalous transport of light at  $\lambda = 1550$  nm.

### *Scaling of the Path Length Distribution*

To obtain the behavior for  $p(s)$  under the scaling theory, consider the path length distribution from a semi-infinite, multiply scattering medium with a point source excitation at its surface [67]:

$$\log[p(s)] = -\frac{3}{2}\log(D) - \frac{5}{2}\log(s) - 2\mu_{abs}s - \frac{z_b^2}{4Ds} + \text{constant} . \quad (27)$$

$z_b$  is the boundary extrapolation length discussed above and  $\mu_{abs}$  is the absorption coefficient. This expression is valid for when  $L/\ell^* \sim 1$ . In our sample, this ratio was about 15. For paths sufficiently far from the boundary and shorter than the absorption length, only the first two terms in Eq. (27) survive. Substituting the  $D \sim s^{-1/3}$  behavior into Eq. (27) and simplifying produces

$$\log[p(s)] \approx -2\log(s) + \text{constant} . \quad (28)$$

### *Physical Basis for the Observed Scaling Behavior*

The scaling theory of localization explains the observations in Figure 21, but it does not explain why the disorder should cause a renormalization of the diffusion coefficient. As previously mentioned, S. John showed that a small amount of disorder near a photonic crystal bandgap could cause weak mode coupling into and out of the gap [9]. Therefore, evidence of a pseudogap would demonstrate a cause for the anomalous light transport.

Figure 22 displays the density of states (DOS) for this photonic crystal as determined from the average of the band diagrams for thirteen different inverse opals using realistic structural parameters for an inverse opal made of amorphous silicon. The depression at 1550 nm is the pseudogap responsible for the renormalization of the diffusion coefficient. The DOS at 1300 nm displays a less well-defined pseudogap and is extremely sensitive to variations in the structural parameters. The light transport at this wavelength is normally diffusive and is not determined by the crystalline structure of the material. A detailed description of how the density of states was determined is given in **Error! Reference source not found.**

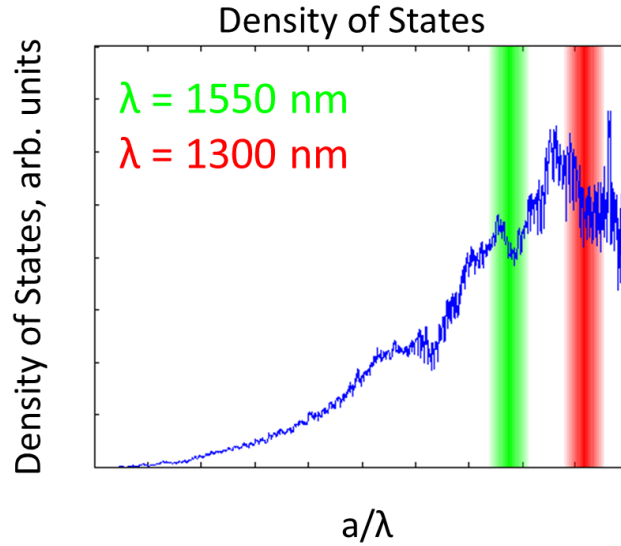


**Figure 22** The calculated density of states for the disordered photonic crystal. The slight depression at 1550 nm is the pseudogap responsible for the renormalization of the diffusion coefficient.

This work is important because it is the first demonstration of both normal and anomalous (renormalized) transport inside the same material. It is also another demonstration of a scale-dependent light-matter interaction. The nature of the interaction changed with the volume of the material that was probed.

### Image Reconstruction by Polarization Multiplexing

In some sensing applications it may be desirable to reduce the number of measurements but still obtain the same amount of information. For example, consider photoactivated localization microscopy (PALM) and stochastic optical reconstruction microscopy (STORM). These techniques work by taking repeated images from a fluorescently labeled sample with a very small number of fluorophores emitting in each image [22,23]. The centroid of the point spread function from each fluorophore is determined and marked for every image. Finally, the centroid data are combined to generate a superresolved image of the labeled sample. Because

many hundreds to thousands of images are needed to recreate one scene, the ease of use of both STORM and PALM are often limited by the amount of time they take to get data. Acquisitions can last from a few minutes to a few hours.

In other cases it may simply be cheaper to take fewer measurements and sacrifice the amount of recorded data. When collecting a scene that spans a wide field of view (FOV) in the infrared region of the spectrum, one may choose to place different cameras in different fixed directions. The cost of infrared cameras is quite large, however, so it may not be feasible to cover all directions. One may instead mechanically scan the camera, but this too introduces complexity into the measurement system.

An alternative to collecting a large FOV with scanning cameras is to encode multiple regions of a scene onto a particular characteristic of the light and detect it using a single CCD camera. Previous work for expanding the field of view has included encoding images using the finite coherence length of a light source and polarization mixing, but these works do not improve the measurement cost [112,113]. A computational imaging technique by a polarization multiplexing/demultiplexing scheme was developed that imaged scenes spanning a  $360^\circ$  FOV in a limited number of measurements. This is an important requirement of any imaging apparatus that encodes information onto the polarization of light because, in principle, there are only four independent measurements of polarization that may be made [114].

### *Proof of Concept*

The polarization mux/demux scheme is illustrated in Figure 23.  $N$  different regions from a scene are encoded onto separate polarization states using polarization optics, i.e. waveplates,

polarizers, etc., and then superposed onto a CCD camera. The camera collects  $M$  mixed images with different settings of the analyzer. At most, four of the mixed images are independent and correspond to the Stokes parameters for the superposed image. The  $M$  images are then fed into a computer where a sparse reconstruction algorithm reproduces the  $N$  original regions. Essentially, the measurement cost is less than the number of outputs since  $N > M$  images are obtained.

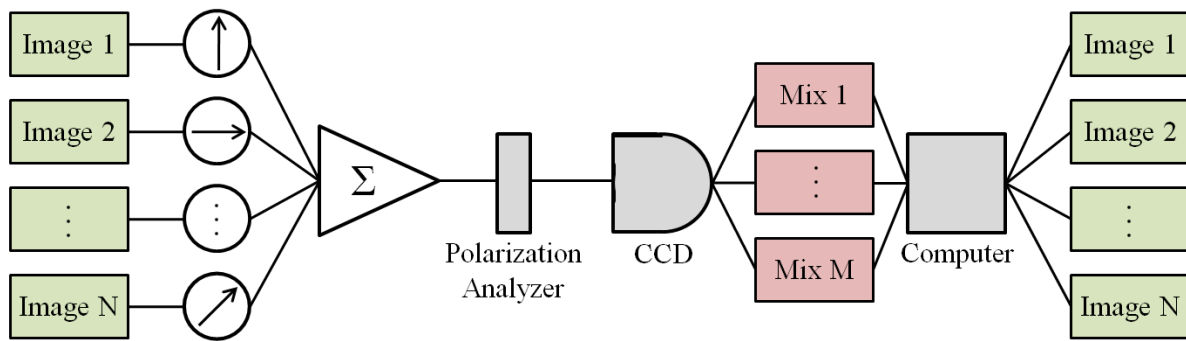


**Figure 23** The polarization multiplexing/demultiplexing scheme.  $N$  images from a scene are encoded onto a single polarization state and overlapped onto an analyzer. The  $M \leq 4$  resulting mixed images are recorded by a CCD camera. A reconstruction algorithm then reproduces the  $N$  original images by applying some appropriate *a priori* information about the scenes.

A proof of concept experiment for this scheme was performed by reconstructing four regions from three independent measurements. The details of the reconstruction are given in the next section and in **Error! Reference source not found.**, but for now the focus is on the results. The setup is displayed in Figure 24. The regions are combined with beamsplitters and imaged with a single lens onto the CCD. Polarizers placed in the imaging path of each region encode the scenes onto linear polarization states with different orientations, while another polarizer is used to reproduce the first three Stokes parameters,  $S_0$ ,  $S_1$ , and  $S_2$  of the mixed scene.

The results of the reconstruction of images of different shapes are found in Figure 25. Each scene contained a shape that coincided spatially with the shapes in the other scenes. Localization of a shape to its direction of origin is not possible without the computational



reconstruction. In Figure 25 b) the Stokes measurements are displayed with the analyzer set to 0, 45, and 90 degrees. The bottom four images display the reconstructed scenes and demonstrate that each shape has been localized to its direction of origin.

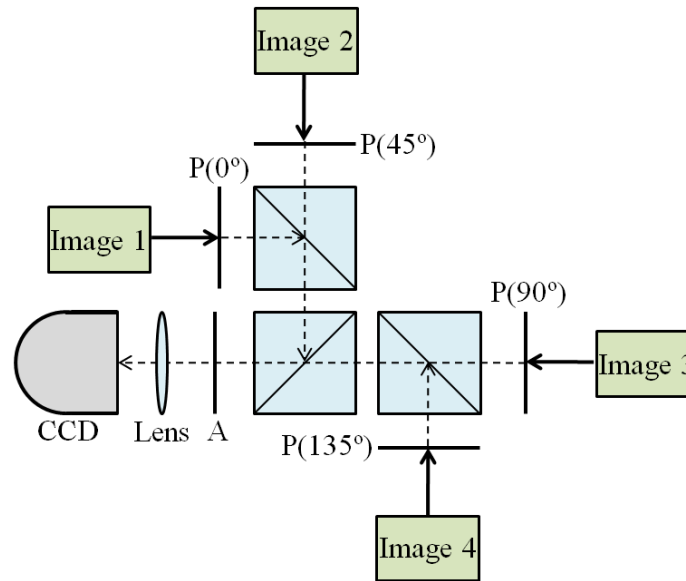


**Figure 24** The 3x4 polarization multiplexing/demultiplexing setup. Four separate input images are encoded onto different linear polarization states (P) and then overlapped at the CCD. An analyzer (A) performs the three Stokes measurements.

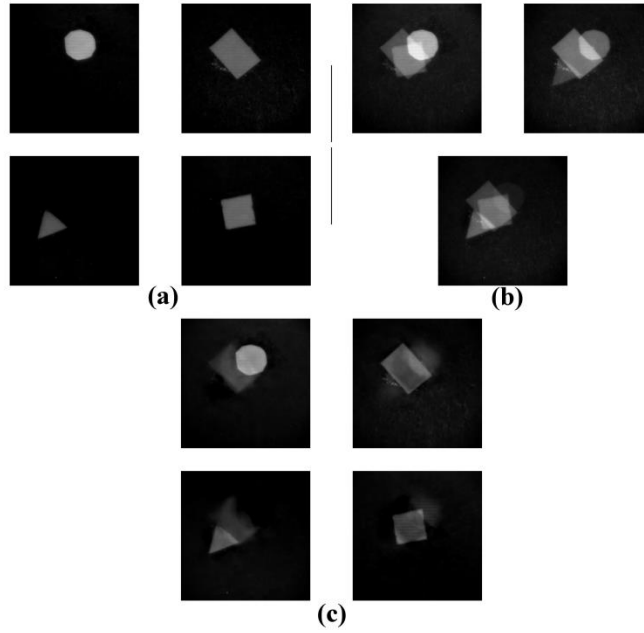


**Figure 25** a) The original scenes of four distinct shapes obtained by blocking all but one arm of the setup in Figure 24. b) The three Stokes measurements showing the overlapped shapes. These measurements were performed with the analyzer set to 0, 45, and 90 degrees. c) The reconstructed scenes, demonstrating that each shape has been localized to its original direction.

### *Reconstruction of Degenerately-Mixed Images*

The reconstruction algorithm is based on a  $\ell_1$ -norm minimization routine that was carried out in Matlab [115]. To understand how this works, consider the act of taking the  $M$  mixed image measurements. The mixed images, assuming incoherent light and unpolarized scenes, may be represented as single elements in a vector  $\mathbf{y}$ :

$$\begin{pmatrix} y_1 \\ y_2 \\ \vdots \\ y_M \end{pmatrix} = \mathbf{A} \begin{pmatrix} x_1 \\ x_2 \\ \vdots \\ x_N \end{pmatrix}, \quad M < N. \quad (29)$$

The columns of the  $M \times N$  mixing matrix  $\mathbf{A}$  contain the Stokes parameters that represent the polarization state that each image is encoded onto. Since  $M < N$ , this set of linear equations is underdetermined and requires *a priori* information to solve.

One powerful assumption is that the original images are sparse. Sparsity describes signals that, in some basis, contain elements with significant energy in only  $K$  elements, with  $L \gg K$  being the number of elements in the signal. For images,  $L$  corresponds to the number of pixels. Sparsity in the direct image space is limited to a small class of images that correspond to very few discrete features against a uniform background, but, in principle, a sparsifying transformation for any image may usually be found using the technique known as basis pursuit [116]. For images, a wavelet representation is almost always sparse [117].

Writing Eq. (29) in a wavelet representation,  $\mathbf{d} = \mathbf{A}\mathbf{c}$ , the reconstruction algorithm proceeds by solving the following optimization problem

$$\hat{\mathbf{c}}_k = \arg \min \|\mathbf{c}_k\|_1, \text{ subject to } \mathbf{d}_k = \mathbf{A}\mathbf{c}_k \quad (30)$$

for  $k=1,2,\dots,K$ . The  $\ell_p$ -norm of a  $D$ -dimensional vector  $\mathbf{v}$  is given by  $\|\mathbf{v}\|_p = \left( \sum_{i=1}^D |v_i|^p \right)^{1/p}$ .

Each  $\hat{\mathbf{c}}_k$  represents the magnitude of the original image in the sparse basis and is the output of the reconstruction. An inverse wavelet transform then produces the reconstructed images.

The motivation for running the optimization routine over the  $\ell_1$ -norm comes from the large and recent body of literature on compressed sensing. This work proves that, in the absence of noise and for sparse inputs, the  $\ell_1$ -norm always converges on the exact answer [118,119]. Satisfactory results were found using this method even in the presence of noise, though there are

more rigorous approaches to deal with noisy images [120]. To demonstrate the practicality of the approach, Figure 26 displays the results of the image reconstruction from more complex objects.

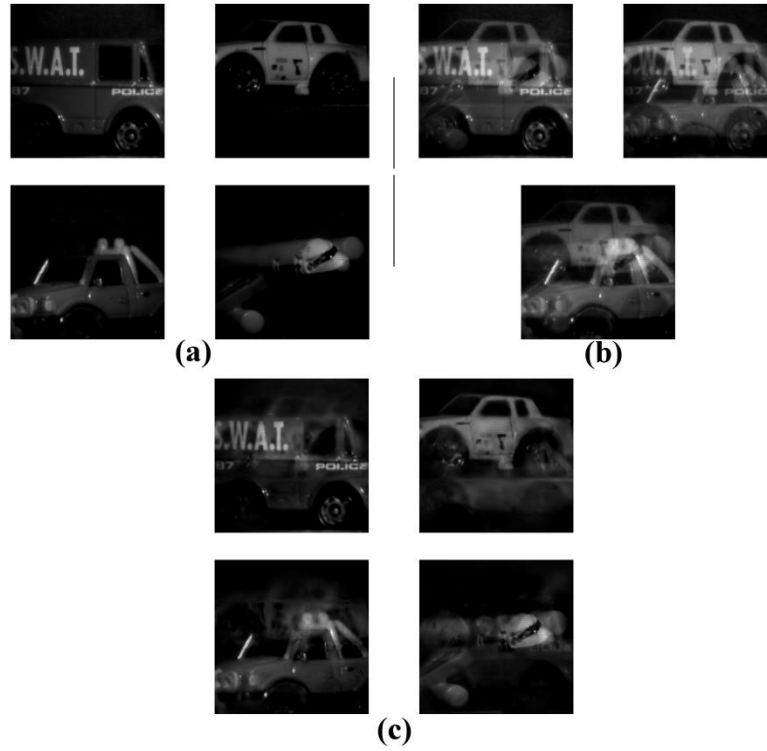


**Figure 26** a) Original, b) mixed, and c) reconstructed images of complex scenes using the polarization multiplexing/demultiplexing setup.

While this work does not deal directly with the mesoscale, one can imagine its utility in speeding up the collection of the typically large data sets in optical sensing applications, many of which work in the mesoscale.

## CHAPTER 4: CONTROLLING MESOSCALE SYSTEMS WITH LIGHT

Structural modifications to microscopic systems can occur when light interacts with matter. Besides interactions involving an exchange of energy, which are well-studied, there can also be a transfer of momentum between light and a material. This chapter details work involving the mechanical control of colloidal suspensions using speckle light fields. The use of speckle as a means of control is novel and intriguing because many systems of interest will strongly scatter light and create a speckle field inside themselves when illuminated. And because colloids share many properties with other physical systems that are much harder to study, such as atomic gases and the liquid state, this work is important for understanding the rich and complex physics involved in such systems.

### Optically Controlled Active Media

The state of the art in control of colloids is currently focused, in part, on active media. Active media are composed of suspended particles that are driven by either intrinsic or extrinsic energy sources in addition to experiencing thermal fluctuations [7,121]. The coupling of energy sources in active media leads to a host of unexpected, nonequilibrium behaviors also encountered in a wide variety of natural phenomena, such as the dynamics of mobile bacteria [51,122], protein diffusion on membranes [123], and turbulent fluid flows [124,125]. These naturally-occurring systems are very complex and not easily amenable to study [126]. To address this issue, a unique realization of an optically controlled active medium was developed to explore the dynamics of these systems. This tunable experimental model consists of diffusing colloidal

particles in a stochastic spatiotemporal 3D speckle pattern and was designed to mimic nonequilibrium states in strongly coupled and disordered systems [127].

The optically-controlled active medium comprises a colloidal suspension of dielectric microspheres that is illuminated by a laser beam. The suspension is contained in a small cavity placed in a large aluminum block that also serves as a heat sink. Reflections from the rough walls of the well and the multiple scattering from the mobile particles completely randomize the three-dimensional optical field in both time and space as illustrated in Figure 27. This inhomogeneous field imparts a random force onto the particles and, as a result, they diffuse under the influence of both the optical and Brownian forces. Furthermore, the speckles change continuously due to the motion of the particles; therefore the light-particle system is strongly coupled, or in other words the dynamics of each part affect the other. This system is easily controllable since the coupling between the particles and the speckle field is determined by the particles' size and composition, as well as the field strength.

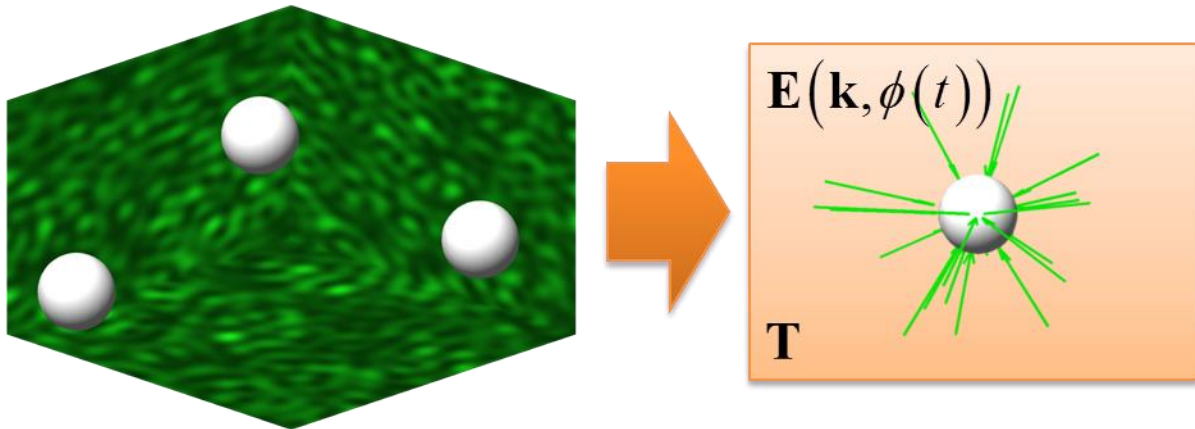


**Figure 27** The particles in a multiply scattering medium are subject to a three-dimensional speckle field. A mean field approximation to this situation is to analyze a single particle in a thermal bath at temperature  $T$  and subject to a number of plane waves with random  $k$ -vectors and phases that vary with time.

In the experiments, different suspensions of polystyrene microspheres were prepared at volume fractions low enough that hydrodynamic coupling between the spheres was minimized yet high enough that the light underwent heavy multiple scattering [83]. The power spectral density (PSD) of the fluctuations of scattered intensity was continuously measured using an optical fiber inserted into the suspension. The frequency dependence of the PSD is related to the particles' mean squared displacement (MSD). When the MSD follows a power law in time, such as  $\langle |\mathbf{r}(t+\tau) - \mathbf{r}(t)|^2 \rangle \sim \tau^\alpha$ , the asymptotic form of the PSD is  $P(f) \sim f^{-(1+\alpha)}$  [128,129]. The exponent  $\alpha$  describes the type of particle diffusion. The particles diffuse normally if  $\alpha = 1$ , while their motion is characterized as subdiffusive or superdiffusive for  $\alpha < 1$  and  $\alpha > 1$ , respectively. Figure 28 (a) illustrates three separate PSD's for the three different diffusive regimes. Figure 28 (b) displays the measured PSD's from a 0.9% wt. suspension of 3.7  $\mu\text{m}$  diameter polystyrene microspheres in water for increasing incident beam powers. When the power of the beam increases, the asymptotic log-log slope of the PSD becomes steeper, which indicates that the particles are becoming more and more superdiffusive.

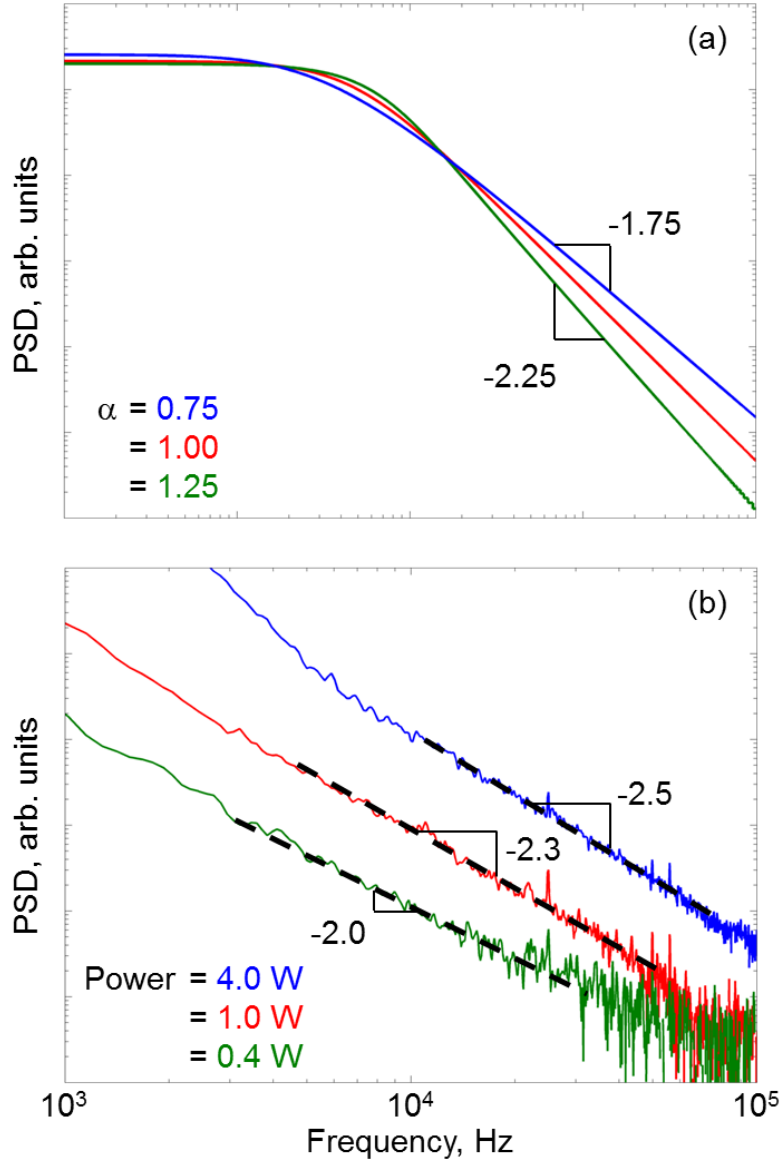


**Figure 28** (a) Theoretical power spectral densities (PSD) of the intensity fluctuations of scattered light from suspended particles. The asymptotic log-log slope is related to the power law exponent of the particles' mean squared displacement,  $\alpha$ . (b) Measured intensity PSD's from a 0.9% wt., 3.7  $\mu\text{m}$  diameter suspension of polystyrene spheres in water. The decreasing log-log slope with incident laser power is indicative of the particles becoming increasingly superdiffusive.

The magnitude of the log-log slope is an indicator of the strength of the coupling between the field and the particles. To see why, consider the Langevin equation of motion for a particle with mass  $m$ , velocity  $v$ , and inertial damping rate  $\gamma$



$$m \frac{dv}{dt} = -m\gamma v + \hat{\xi} + \hat{F}. \quad (31)$$

where  $\hat{\xi}$  is the delta-correlated, zero-mean random term responsible for Brownian motion. The random optical force  $\hat{F}$  is due to the additional source of energy in an active medium [130].

Considering times much longer than  $\gamma^{-1}$ , the MSD calculated from Eq. (31) is

$$\langle |r(t+\tau) - r(t)|^2 \rangle = \frac{2k_B T}{m\gamma} \tau + \frac{F_0^2}{(m\gamma)^2} \int_0^\tau \int_0^\tau \Gamma(t' - t'') dt' dt'' \quad (32)$$

with  $F_0^2 \Gamma(t' - t)$  representing the autocorrelation of the optical force. (See **Error! Reference source not found.**) For times much shorter and longer than the characteristic time  $t_c$  of  $\Gamma(t' - t)$ ,

the MSD becomes

$$\begin{aligned} \langle |r(t+\tau) - r(t)|^2 \rangle &= \frac{2k_B T}{m\gamma} \tau + \frac{F_0^2}{(m\gamma)^2} \tau^2, \quad \tau \ll t_c \\ &= \frac{2k_B T}{m\gamma} \tau + \frac{F_0^2}{(m\gamma)^2} \sqrt{2\pi} t_c \tau, \quad \tau \gg t_c. \end{aligned} \quad (33)$$

This result assumes that  $F_0^2 \Gamma(t' - t)$  is Gaussian, but the reasoning applies for any exponentially decaying autocorrelation function. The MSD rises quadratically at first but then increases linearly for times much longer than  $t_c$ . For times similar to  $t_c$ , it grows with a time-dependent exponent  $\alpha = d[\log \text{MSD}] / d[\log t]$  that lies between 1 and 2, which is reflected in the log-log slope of the PSD of the scattered intensity fluctuations of light. Furthermore, the magnitude of the optical force  $F_0$  is determined by the particle size, refractive indices, and average optical

power. Changing any of these parameters deterministically changes the MSD and allows for an optically-controlled diffusion.

The movement of an ensemble of single particles in spatiotemporal speckle was also simulated with three-dimensional Brownian dynamics simulations. In these simulations, the field incident on a particle accounted for the multiple scattering inside the suspension. This assumption, which is similar to mean field approximations in condensed matter physics [131,132], requires specific spatial and temporal autocorrelations for the constructed field (see again **Error! Reference source not found.**). At each step, the particle's position was updated and reflected a random displacement due to Brownian motion and a displacement due to an optical force applied over the length of the time step. Figure 29 (a) displays the MSD for a diffusing particle whose radius is  $1.85\text{ }\mu\text{m}$  and is subject to a mean-volume speckle field for several different RMS electric field strengths in the cavity. Neglecting the short time inertial and hydrodynamic effects, the MSD for small times grows linearly until the acceleration from the optical force becomes appreciable. This is reflected in the upward bend of the MSD. Once the optical force decorrelates (which in the real system is due to the motion of the particles), the MSD levels out again to a linear dependence in time (not shown in this plot). The deviation from normal diffusion, which is represented by the lowest field magnitude, depends on the strength of the coupling between the light and the particles. Figure 29 (b) depicts the PSD of the intensity fluctuations that would arise from a suspension of particles exhibiting this MSD.

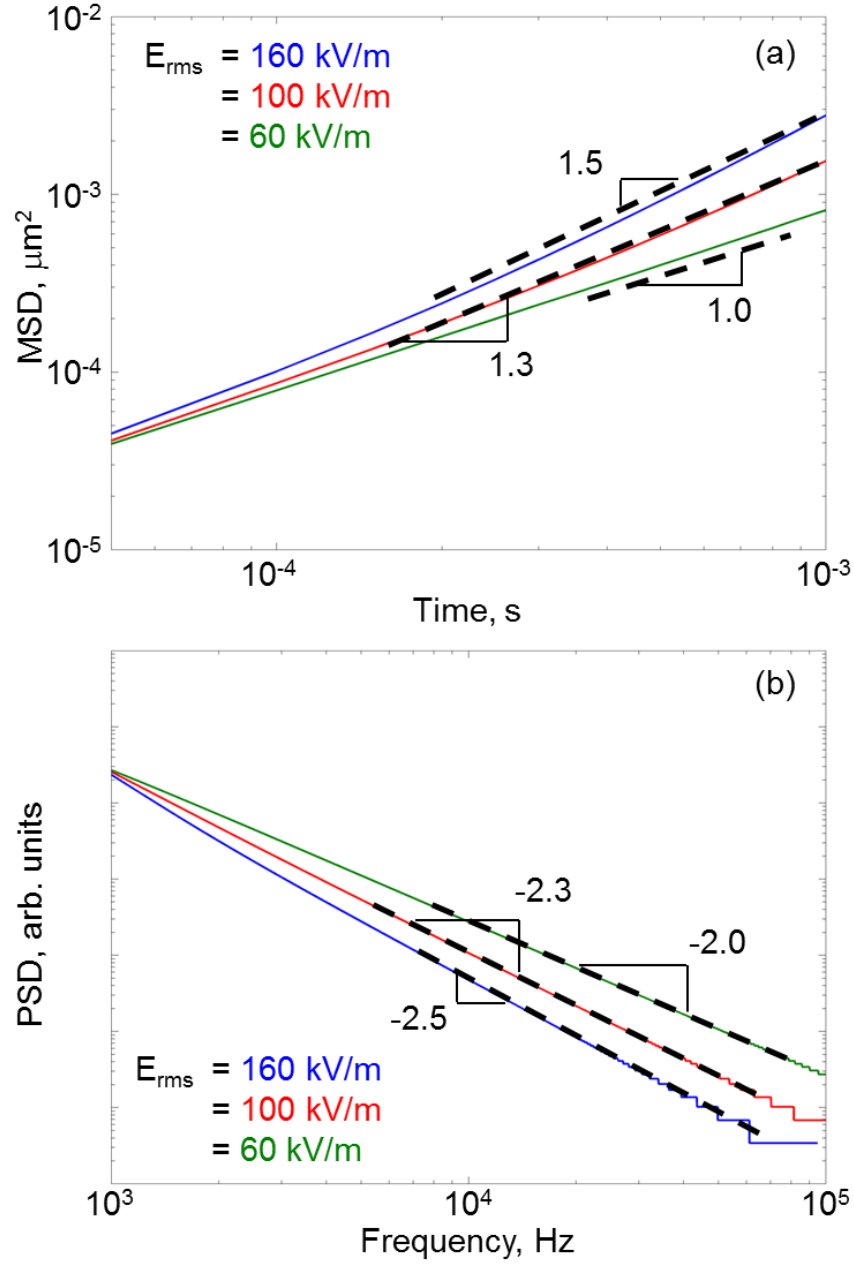


**Figure 29** (a) Numerically calculated mean squared displacement of a polystyrene sphere of radius 1.85 microns in the mean field approximation. The sphere undergoes Brownian motion for short times and gradually becomes superdiffusive at longer times. The log-log slopes of the dashed lines are the average log-log slope of the curves over the displayed range of frequencies. (b) Calculated intensity PSD's from the MSD's in (a). The log-log slope of the PSD's decreases with the increasing RMS field magnitude in the simulated cavity.

Changes in temperature have been ruled out as a cause of the observed effects. A change in temperature should only cause a shift of the MSD curves along the y-axis. At the same time,

the corner frequency, and not the log-log slope, should change in the PSD's. Simulations of the distribution of heat inside the well were also carried out and found to be negligible since the aluminum block acted as a heat sink in this experiment [133].

The effect of the light in our system is fundamentally different from other active media. For example, the particles' motion for optically-controlled Janus particles is due to thermophoresis [52]. The negligible absorption of polystyrene precludes this. In fact, it is the coupling between the light and particles that drives the observed effect. This aspect of the model is important to the study of diffusion in spatiotemporal random potentials, where it is unclear as to whether the motion is sub- or superdiffusive in the long time limit [47,53–57,130]. In addition, in the fully developed 3D speckle field both the gradient force and the radiation pressure are significant, which is unlike previous considerations of radiation pressure on colloidal particles [37,134].

This experimental model of active media demonstrates the dynamic coupling between two random processes: the Brownian motion of particles and the reconfiguration of the electromagnetic field in space and time. The extra energy provided by the light through this coupling leads to superdiffusive behavior of the particles. The coupling between the particles' motion and the light is controlled through the optical power and particle size, but also may be influenced through the particles' composition and shape.

### Dipole-dipole Interactions in Random Electromagnetic Fields

In the previous section the colloidal particles were treated as being independent; in other words, their motion did not affect their neighbors. However, this assumption is not strictly true

for certain suspensions in which the particles interact and affect one another's motion. When this happens, the random motion of individual particles may no longer be treated independently. Not surprisingly, electromagnetic fields may mediate some of these interaction forces between particles in colloidal suspensions [45]. What is surprising, however, is that *random* electromagnetic fields can still give rise to an interaction force.

There are a number causes of particle interactions in colloids. In an uncharged colloid, hydrodynamic effects tend to dominate all the interactions between particles, but this is only appreciable for suspensions that are dense enough. In dilute suspensions, the particles are effectively independent. A hydrodynamic interaction is one in which one particle exerts a force on one or more other particles by virtue of its movement through the solvent fluid. Hydrodynamic interactions are notoriously difficult to model, but their effects may be observed at least qualitatively in DLS experiments [135].

In charged colloids, the particles exert forces on one another through an electrostatic field. These types of colloidal suspensions have been studied for many decades and exhibit many interesting properties [136].

In this section a class of interactions between neutral particles with dipole moments that are induced by random electromagnetic fields will be explored [137]. The emergence of a force between two particles in a spatially incoherent field is counterintuitive because one might expect that the force would average out to zero, as it does in temporally incoherent fields [138]. This pair-wise force nevertheless survives an ensemble average of quasi-monochromatic field realizations. What is also surprising is that it is a long range force that exists over distances of multiple wavelengths and shares some characteristics with the optical binding phenomenon [45].

This type of interaction is important because it provides a new method for engineering colloidal dynamics and provides new insights into the connections between colloidal physics and statistical mechanics.

### *Optical Binding*

The interaction between two or more particles in a strongly focused electromagnetic field is well-studied and called optical binding (OB) [45,139,140]. Understanding OB is a good starting point for understanding the interaction between particles in a random electromagnetic field. In OB, colloidal particles are illuminated by a strong laser field and form bound states corresponding to some local minima in their mutual energy. The location and depth of these minima are determined by the wavelength of the light, the shape of the illuminating beam, and its intensity. For cases involving two particles, the minima will tend to lie at relative distances that are on the order of a wavelength apart [45]. OB has been explained by a model that takes account of the local field modifications within the vicinity of a particle using Greens functions [141].

The OB force between two dipoles is illustrated in Figure 30. These curves are the result of evaluating the expressions for the force given in Ref. [138] and the total field provided in Ref. [141] between two induced dipoles in a purely dielectric material illuminated by a plane wave traveling 1) perpendicular to the line joining the dipoles and 2) parallel to the line joining the dipoles. The force is long range and oscillates periodically. For transverse illumination, the periodicity of the oscillations is about one wavelength. For longitudinal illumination, it is about half the wavelength of the light. OB under longitudinal illumination is typically stronger than

under transverse illumination [139]. The exact positions of the minima also depend on the polarization of the light.

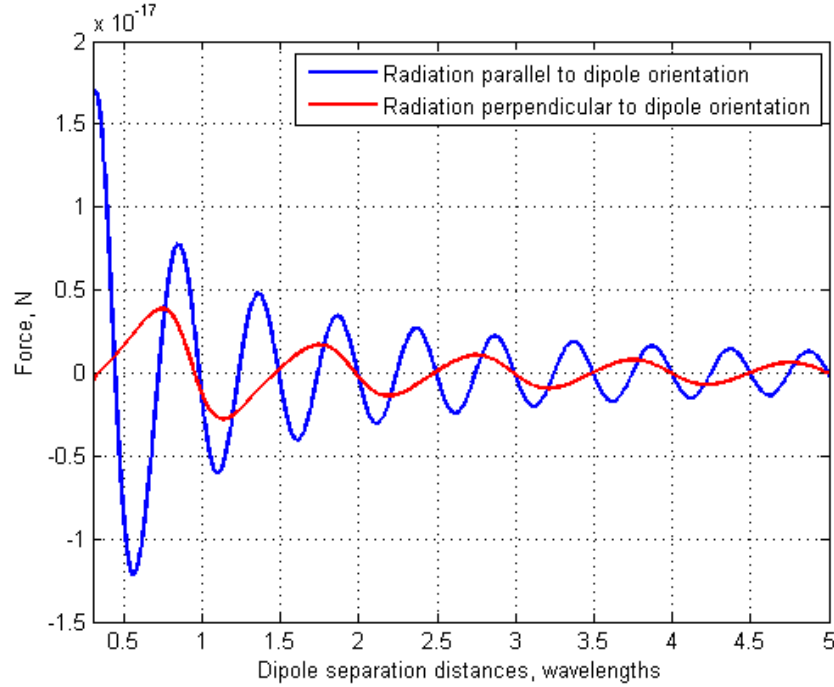


**Figure 30** The optical binding force for two different directions of plane wave illumination relative to the line joining the dipoles.

More complex OB-like interactions have been observed in large, optically bound structures of many particles [135,139]. Additionally, the particles may actually spin and rotate about their center of mass when illuminated by light carrying orbital angular momentum [144]. These are just a few of many examples of how light may mediate forces between particles in suspension.

### *Particle Pair Interactions in Spatially Incoherent Fields*

In the studies of OB mentioned in the preceding discussion, the illumination is deterministic. In other words, the light beams had intensity profiles and polarizations that were

non-probabilistic and unchanging. The question of whether two colloidal particles (dipoles, in this treatment) may interact in a spatially inhomogeneous and random electromagnetic field has not been addressed. This question adds another degree of complexity to the study of optically-controlled active media because particles interacting through such a field will not be independent of one another's positions.

A similar question involving induced particle interactions in temporally partially coherent fields has been addressed in Ref. [138]. In this work, the researchers explored the OB phenomenon in temporally partially coherent fields. They found that, as the bandwidth of the illumination was increased, the optical binding strength diminished. This was due to minima in the potential energy that were located at different positions for different wavelengths. This means that adding temporal randomness to the controlling field reduced the strength of the interaction, which is why it is perhaps surprising that the interaction force would survive in spatially incoherent fields.

The same system as Depasse and Vigoreux of two dipoles, one at the origin and another at a distance  $R$  from the origin along the  $x$ -axis, is considered [141]. This arrangement is illustrated in Figure 31. The dipoles have no static charge and a complex polarizability,  $\alpha$ .



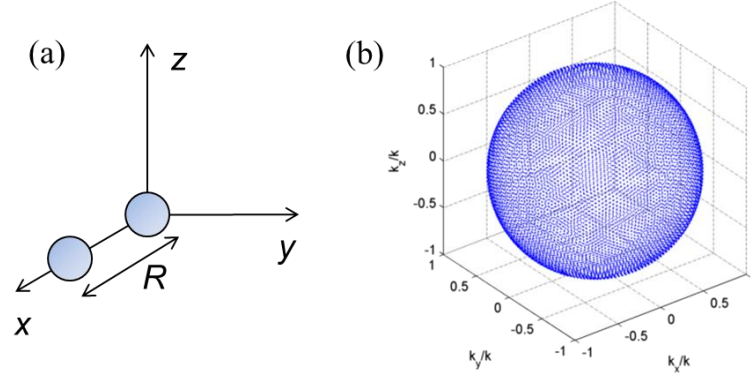


**Figure 31** The geometry for determining the dipole interaction force in spatially inhomogeneous fields. (a) Two dipoles are situated on the x-axis, one at the origin and one at a distance  $R$  from the origin. (b) One realization of the Gaussian field is constructed by a superposition of plane waves whose directions are given by the coordinates on the full Ewald sphere. Each plane wave has a phase that is randomly and uniformly distributed between 0 and  $2\pi$ .

The random, spatially incoherent field that illuminates the dipoles in this study is a Gaussian random field (see Figure 31 (b)). Also referred to as fully developed speckle, this field is constructed by a superposition of plane waves traveling in all possible directions in three dimensions. The directions are given by unit vectors whose end points lie on the Ewald sphere. The field is monochromatic and the polarization of each plane wave is described by a complex vector of unit magnitude whose direction in the complex plane is random and uniformly distributed between 0 and  $2\pi$  [144].

The derivation consists of finding the force on the dipole at  $\mathbf{r}_2 = R\hat{\mathbf{x}}$  in the presence of the other dipole at the origin. First, the total, time-harmonic field at the second dipole is calculated. The total field is derived from the following system of two equations in two unknowns [141]:

$$\begin{cases} \mathcal{E}^\gamma(\mathbf{r}_1) = \mathbf{E}^\gamma(\mathbf{r}_1) + \overline{\overline{G}}\alpha\mathcal{E}^\gamma(\mathbf{r}_2) \\ \mathcal{E}^\gamma(\mathbf{r}_2) = \mathbf{E}^\gamma(\mathbf{r}_2) + \overline{\overline{G}}\alpha\mathcal{E}^\gamma(\mathbf{r}_1). \end{cases} \quad (34)$$

$\mathcal{E}^\gamma(\mathbf{r})$  is the total electric field at the point  $\mathbf{r}$ ,  $\mathbf{E}^\gamma(\mathbf{r})$  represents the incident, Gaussian electric field,  $\bar{\bar{G}}$  is the Greens function tensor and  $\alpha$  is the polarizability of the dipoles. The solution for the field at the second dipole,  $\mathbf{r}_2 = R\hat{\mathbf{x}}$  is found easily from these equations to be

$$\mathcal{E}^\gamma(\mathbf{r}_2) = \left( \bar{\bar{I}} - \bar{\bar{G}} \alpha^2 \right)^{-1} \left[ \mathbf{E}^\gamma(\mathbf{r}_2) + \bar{\bar{G}} \alpha \mathbf{E}^\gamma(\mathbf{r}_1) \right]. \quad (35)$$

Once the total field is found, it may be used to find the ensemble average force between the dipoles. Due to the symmetry of the system, only an x-component of the force will survive after averaging over many realizations of the field. The expression for the total force between two induced dipoles is [142]

$$\langle F_x(\mathbf{r}) \rangle = \frac{1}{2} \text{Re} \left[ \alpha^* \left\langle \mathcal{E}^{*\gamma}(\mathbf{r}) \frac{\partial \mathcal{E}^\gamma(\mathbf{r})}{\partial x} \right\rangle_\gamma \right]. \quad (36)$$

The result of this derivation for dielectric and nonabsorbing particles such that  $|G_x \alpha| \ll 1$ ,  $|G_y \alpha| \ll 1$ , and  $\text{Im} \alpha \ll \text{Re} \alpha$  is (see **Error! Reference source not found.**)

$$\begin{aligned} \langle F_x(R) \rangle &\approx \frac{1}{6} \langle I \rangle \alpha^2 k^4 f(kR) \\ f(\xi) &= \frac{3 \left[ \xi (18 - 8\xi^2 + \xi^4) \cos(2\xi) + (-9 + 16\xi^2 - 3\xi^4) \sin(2\xi) \right]}{\xi^7}. \end{aligned} \quad (37)$$

In the limit of small dipole separations,  $\lim_{\xi \rightarrow 0} f(\xi) = -(11/5)\xi^{-2}$ , the force is attractive and its magnitude increases as the inverse square of the separation distance. In comparison, the force

goes as the inverse distance in OB. To reiterate, the fact that the average force is not zero is in itself surprising given that the illuminating speckle is fully developed.

### *The Nature and Consequences of the Non-zero Interaction Force*

The interaction force is plotted in Figure 32. This curve was generated by computing the average force between two dipoles with equal radii of  $0.15\text{ }\mu\text{m}$  and refractive indexes of 1.59 in a background medium with index 1.33. (Arbitrary units are used on the y-axis because it's not clear how to relate the average field strength of a three dimensional electromagnetic field to a more familiar quantity, like the irradiance of a laser beam.) There are two important characteristics of this force: it is long range, which means it extends over multiple wavelengths of the incident light, and it is oscillatory with a period of about half the excitation wavelength. In this sense, it is very similar to the longitudinal optical binding force plotted in Figure 30. Particles will tend to position themselves at distances equivalent to the zeros of the force in this curve in the absence of other forces, like thermally-induced Brownian motion or hydrodynamic interactions. When the other forces are present, the particles are only more likely to be at these positions relative to others; they will not be at these positions with absolute certainty.

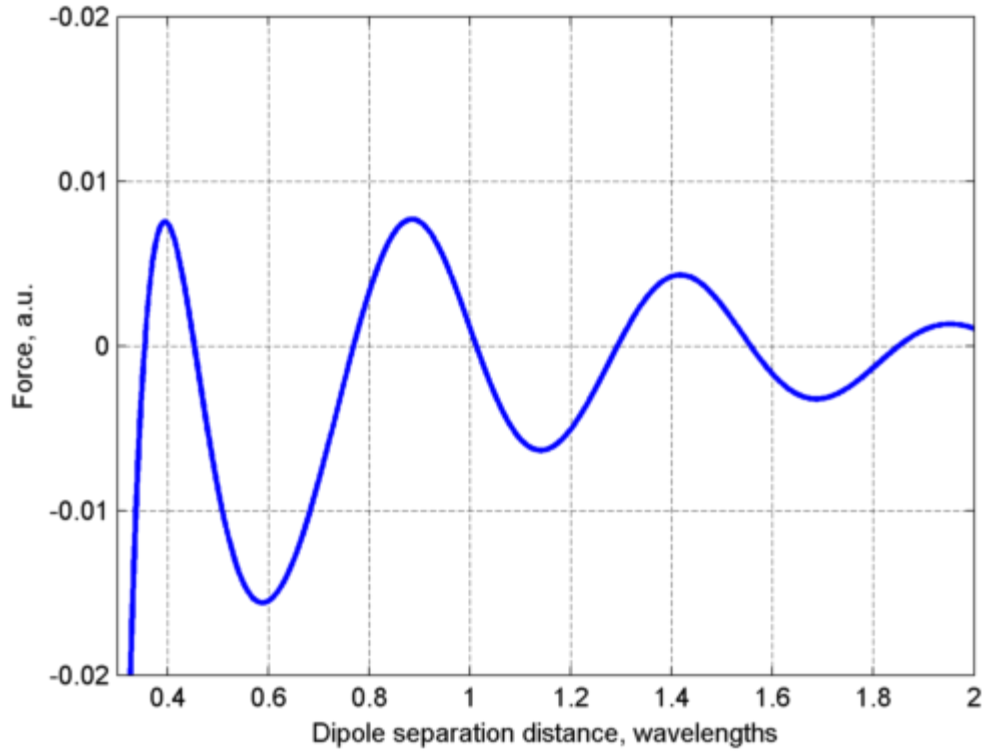


**Figure 32** The dipole interaction force between particles in a Gaussian random field. The force is long-ranged and oscillatory with a period of about half the illumination wavelength.

It's interesting to note that the existence of this force is not dependent on a field quantity that is a Gaussian random variable. A partially spatially coherent field can be constructed by taking two small patches on the Ewald sphere that are circularly symmetric and diametrically opposed. This would be equivalent to illuminating the dipoles from two directions through a finite numerical aperture. The forces between the dipoles illuminated by randomly polarized plane waves emanating from diametrically-opposed Ewald sphere patches with a half-angular width between 30 and 60 degrees are displayed in Figure 33. 1000 realizations of the field were generated by assigning a random polarization to each plane wave, superposing them, then calculating the total field and the force on the dipoles from this incident field. Because the symmetry is broken in this case, the orientation of the dipoles was changed uniformly and

randomly for each realization. This is known as a tumble average. Doing this better approximates the outcome of an experiment on real colloidal particles since they are in a state of constant motion and continuously changing their positions. The material properties are the same as in Figure 32.

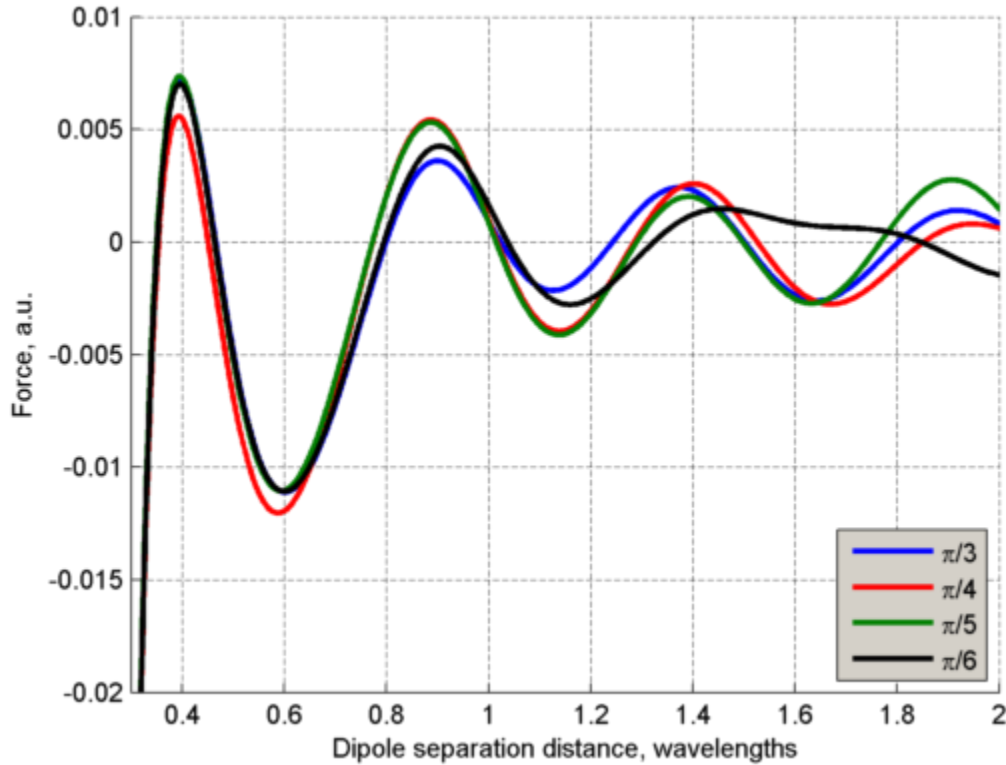


**Figure 33** The pair interaction force for other types of spatially random fields. Each curve corresponds to dipoles in fields whose Ewald spheres are partially covered with two diametrically-opposed, circularly-symmetric patches with the given half angular width. The curves are normalized to their first data points.

Qualitatively, the forces remain similar, despite the non-Gaussianity of the incident field. This may be understood if one accepts the case presented in Figure 32 (an incident Gaussian random field) as one extreme of the interaction and optical binding in a single plane wave at the other extreme. Both extremes have qualitatively similar features, so it stands to reason that illumination of the dipoles by the intermediate cases of plane waves covering only parts of the Ewald sphere should be similar to the other two as well.

Lastly, the dependence of the force on the directions of individual plane waves that comprised the field was considered. To simulate this, the orientation of the dipoles along the x-axis was fixed. Then, they were illuminated with plane waves whose directions covered two circularly-symmetric and diametrically opposed patches on the Ewald sphere with half angular widths of 45 degrees. One thousand realizations of the field were generated for each of three cases with the axis of symmetry joining the two patches set to 0 degrees, 45 degrees, and 90 degrees to the x-axis. At 0 degrees, the plane waves traveled predominantly at longitudinal directions to the line joining the dipoles and at 90 degrees they are predominantly transverse. The forces are plotted in Figure 34.

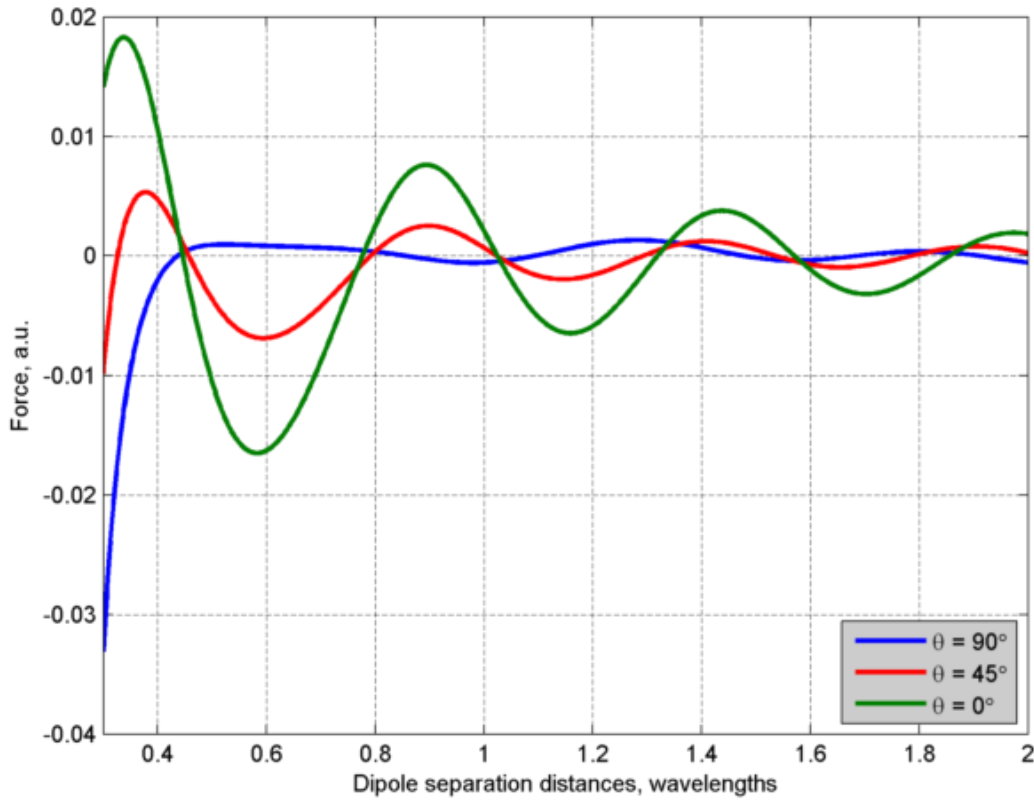


**Figure 34** Pair interaction force between dipoles illuminated by randomly polarized plane waves traveling predominately longitudinal (0 degrees), around 45 degrees, and transverse (90 degrees) to the line joining the dipoles.

Again, the forces are qualitatively similar, but this time they display some significant differences. Clearly, for longitudinal illumination, the amplitude of the oscillations in the force is stronger, which gives rise to more stable bound positions of the dipoles. Also, the period of the oscillations belonging to the force for the transverse illumination is not half a wavelength but is closer to one full wavelength of the illuminating light. This is the same for transverse optical binding, where a plane wave illuminates two dipoles perpendicularly to the line joining the dipoles.

The pair interaction between dipoles was examined for two reasons. For one, it is a simple first step to explore the nature of interaction forces in a many-body system, like a colloidal suspension. More importantly, though, the pair interaction force often largely determines the macroscopic properties of a disordered, many-body system [146]. Thus, this study may lead to even more ways to control dense, complex materials using light.

## CHAPTER 5: CONCLUSIONS AND OUTLOOK

### A Summary of the Past and Present

Mesoscale optics spans fields such as cell biology, materials science, and chemistry. As a framework, it unifies the interpretation of the interaction of light with complex media when the outcome depends significantly on the scale of the interaction. With this interpretation, new and superior approaches for characterizing, understanding, and controlling complex mesoscale systems may be developed.

The essential concept in mesoscale optics is that the outcome of an experiment is determined, among other things, by the volume of the light-matter interaction. Information about the material parts within it and how they are interconnected is encoded onto the many properties of the scattered and re-emitted light. The information content carried by the light naturally changes as the interaction volume changes size or duration. This concept is the basis of a framework for understanding scale-dependent light-matter interactions.

There are three aspects of mesoscale optics. These aspects—observations, modeling, and control—describe the goal of an experiment and determine the approach to the stated problem. They are not mutually exclusive.

The first aspect that was discussed (Chapter 2) dealt with observations of mesoscopic phenomena. Observing such phenomena in materials is facilitated by techniques that control the volume of the light-matter interaction, such as low coherence interferometry. This technique is used to suppress multiple scattering of light within a turbid medium to learn about the dynamics of small volumes of analyte. Effectively, it enables workers to probe extremely disordered materials by controlling the size and location of the volume being probed. Low coherence



interferometry was employed to analyze the dynamics of the microscopic structure of picoliter-sized volumes of complex fluids. This allowed for the determination of some important material properties, such as particle size, viscoelasticity, or even the clotting time of human blood.

Another application of low coherence interferometry, optical path-length spectroscopy, revealed the scale-dependent nature of photon diffusion inside a turbid medium, specifically near a material boundary. It works because only certain photon path lengths are observed at a time, allowing the experimenter to separate the different contributions to the diffuse energy from an otherwise intractable signal.

In Chapter 3 new ways to model mesoscale light-matter interactions were presented. There, a new assay for exploring cell motility on curved-substrates was developed along with numerical tools for answering the question “is the cellular motion anisotropic?” This experimental model will have important applications for studying other cellular processes as well, such as the formation of the myelin sheath around axons [147].

Myelination of axons by Schwann cells is a process in which a mechanical phenomenon like motility plays an important role. In spite of intense research, understanding the physical and cytoskeletal basis of myelination is still rudimentary and this impacts the development of treatments for myelin-based diseases. Extension of the work performed on Schwann cell motion on curved substrates could also include the myelination process. Importantly, the ability to grow Schwann cells on a tapered fiber will permit the study of distinctive aspects of the interaction between axons and myelin-secreting Schwann cells typically found in the peripheral nervous system. Such an approach may provide answers to fundamental questions about the myelination process such as: Is there a minimum critical diameter of the axon at which myelination occurs?

What limits the number of myelin layers? Does myelination proceed as a step wise process of wrapping followed by compaction, or in some other manner?

Approaches like this one in mesoscale optics will help scientists learn about many other complex and microscopic systems found in biology. The entire cellular system especially has come under increasing scrutiny by physicists in the last few decades [5,95,148–150]. This may be attributed to two reasons, among many others: better technologies have allowed us to probe its mechanical structure and it serves as the quintessential system for testing new physical theories, such as nonequilibrium thermodynamics [7,126].

Light interacting with highly scattering media is often modeled as diffusive. However, in complex materials such as disordered photonic crystals, light diffusion is anomalous. This atypical kind of transport is due to a coalescence of order and disorder within the silicon lattice of the crystal. Despite the complexity of the transport process, a simple model was developed based on a path-length dependent diffusion coefficient that explains the phenomenon well. The validity of this model was verified with unique experimental measurements based on optical path length spectroscopy. These measurement techniques were tailored to observe processes that change over many length and time scales.

A signal that is leaving the interaction volume in mesoscopic systems may be too complex to process by existing means and new approaches may be required in specific situations. A new way to multiplex multiple images onto a single sensor was described in Chapter 3 to address one issue of complexity. Based on polarization multiplexing, the scheme uses a sparse model to maximize the information throughput with the appropriate use of priors. It has important advantages for imaging and sensing at variable scales of interaction.

Aside from being a characterization tool, light can also modify properties of a material. Chapter 4 demonstrated the control of an active medium using not the energy but the momentum carried by light. The random nature of an active medium and the coupling between the light and matter made this system inherently mesoscopic. Models based on the Langevin equation and Brownian motion were evoked to explain the observed patterns in the scattered light. The model did not account for the coupling between the particles and the randomly scattered light. In-depth understanding of the intricacies of this new phenomenon may lead to new means to control such systems and new understandings in related systems, such as atomic condensates and systems driven far from equilibrium.

The development of this model active medium is important to cellular biomechanics because it mimics many superdiffusive processes inside the cell, such as the motion of vacuoles driven by molecular motors and the diffusion of proteins within the cell membrane. Due to their size and their immersion in the cytoplasmic bath at physiological temperatures, the motors and proteins are subject to random thermal fluctuations, despite being driven by the cellular machinery. As a result, their motion is described by anomalous diffusion [47], just as the motions of the particles were described within our experiment. Turning now to the control of cells, it should be noted that optical influences on cellular processes are usually considered to be photochemical in nature. However, at optical frequencies the impedance of the cell membrane is low, so even weak electromagnetic fields may permeate the entirety of a cell body and interact with its components. Because of this and the fact that light carries momentum [35], one can imagine that cellular biomechanics may also be affected using light.

As another building block to this complex phenomenon, the electromagnetic interaction between two induced dipoles subjected to a spatially incoherent field was also addressed in Chapter 4. It was found that, unintuitively, an oscillatory force that depends on the separation between the dipoles survives even after an ensemble average over field realizations,. This is a rather counterintuitive result because one might expect that any force arising from an electromagnetic interaction would average to zero in a random field. The consequences of this force should be manifest in the macroscopic properties of the colloid.

The most important contribution to optics from the framework presented in this dissertation is that it places sensing and control problems within a systems-based context. In other words, the interaction volume is a black box with input signals that may change its behavior and output signals that contain information about its properties. From this starting point, an experimentalist can design efficient and simple techniques for learning about or controlling the system. This approach is in contrast to those that rely on rigorous physical models to explain an otherwise simple phenomenon. Though the more rigorous model may be complete, it may complicate the experimental design and understanding of a project by introducing more complexity than is needed. The goal of the framework is to simplify measurements and models to make them easier to understand for scientists working in different fields.

The foundations of mesoscale optics are proving to be important to the study of microscopic, complex systems. Cellular sensing and biophysics, in particular, should benefit greatly from this framework. My hope with this work is to make sense of the highly disordered, the small, and the enormously complex systems that impact the quality of our lives.

## **APPENDIX A: FUNDAMENTALS OF DYNAMIC LIGHT SCATTERING**

## Useful Quantities in Dynamic Light Scattering

### *The Intensity and Field Autocorrelation Functions*

The measured quantity in a dynamic light scattering experiment is the intensity autocorrelation function, which is defined as

$$G^{(2)}(\tau) \equiv \langle I(t)I(t+\tau) \rangle. \quad (38)$$

This quantity describes the similarity of the scattered intensity from a dynamic sample between two times separated by a duration  $\tau$ . The field autocorrelation function is defined as

$$G^{(1)}(\tau) \equiv \langle E^*(t+\tau)E(t) \rangle. \quad (39)$$

If Eq. (38) is normalized to  $\langle I^2(t) \rangle$  and Eq. (39) to  $\langle |E(t)|^2 \rangle$ , then the normalized intensity and field autocorrelation functions are obtained

$$g^{(2)}(\tau) \equiv \frac{\langle I(t+\tau)I(t) \rangle}{\langle I^2(t) \rangle} \quad (40)$$

$$g^{(1)}(\tau) \equiv \frac{\langle E^*(t+\tau)E(t) \rangle}{\langle |E(t)|^2 \rangle}. \quad (41)$$

In a DLS experiment, one measures  $G^{(2)}(\tau)$  and from it derives  $g^{(1)}(\tau)$ . Information about the refractive index density fluctuations of the medium are encoded onto  $g^{(1)}(\tau)$ .  $g^{(1)}(\tau)$  is equivalent to the intermediate scattering function (ISF),

$$F(\mathbf{q}, \tau) = \frac{\langle \rho(\mathbf{q}, t + \tau) \rho^*(\mathbf{q}, t) \rangle}{\langle |\rho(\mathbf{q})|^2 \rangle} \quad (42)$$

which describes the dynamics of the refractive index density,  $\rho(\mathbf{q}, t)$ , with time. The point of a DLS experiment is to determine the ISF and link it to meaningful quantities that describe the medium, such as radial distribution functions and dynamic structure factors [151]. Figure 35 illustrates the relationship between these quantities.

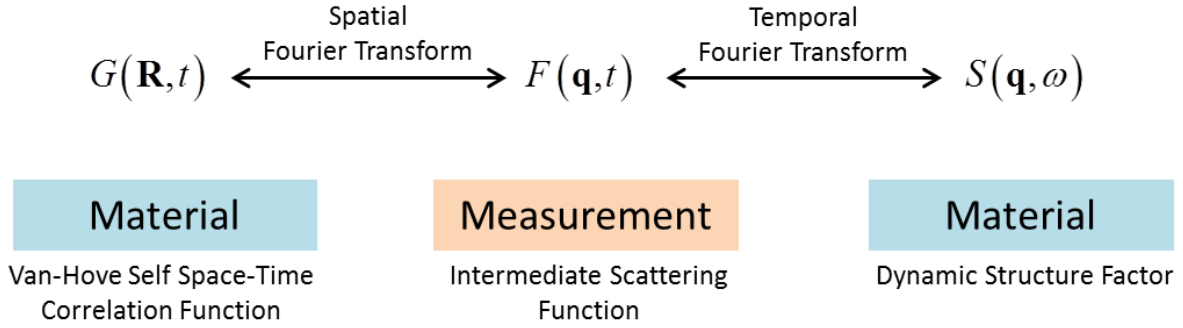


**Figure 35** The relationships between the measured quantity in a DLS experiment and material properties.

### *Material Correlation Functions*

The Van-Hove self space-time correlation function is defined as

$$G(\mathbf{R}, \tau) \equiv \langle \delta(\mathbf{R} - [\mathbf{r}(t + \tau) - \mathbf{r}(t)]) \rangle. \quad (43)$$

This function describes the probability that a particle (or more generally a density fluctuation) will suffer a displacement  $\mathbf{R}$  in a time  $\tau$ . For example, in a colloidal suspension of independently moving particles, the self correlation function is just the probability distribution function describing a particle's location at a given time. Eq. (43) may be obtained from the ISF by taking a spatial Fourier transform

$$G(\mathbf{R}, t) = (2\pi)^{-3} \int_{-\infty}^{\infty} F(\mathbf{q}, t) \exp(-i\mathbf{q} \cdot \mathbf{R}) d^3q. \quad (44)$$

This computation requires knowledge of the ISF across all scattering angles. For isotropic systems, Eq. (43) is a time-dependent radial distribution function.

The dynamic structure factor of the medium is obtained from the time-domain Fourier transform of the ISF:

$$S(\mathbf{q}, \omega) \equiv (2\pi)^{-1} \int_{-\infty}^{\infty} F(\mathbf{q}, t) \exp(i\omega t) dt. \quad (45)$$

This quantity is the power spectral density of the refractive index fluctuations measured at one scattering angle  $\mathbf{q}$ .

### The Siegert Relation

In a homodyne experiment, when there is no reference field to interfere with the light scattered from the sample, Eq.'s (40) and (41) may be related if some conditions are satisfied. This well-known relationship is the Siegert relation [78]. It is expressed as

$$g^{(2)}(t) = 1 + \left| g^{(1)}(t) \right|^2. \quad (0.46)$$

This relation is valid when the scattered field at the detector is a superposition of the fields originating from a large number of independent scattering volumes within the volume of interaction between the light and sample. By large I mean that enough scattering volumes exist such that the field at the detector follows a zero-mean Gaussian distribution according to the central limit theorem [18]. Third and higher-order moments of the Gaussian distribution are



completely defined by the first and second-order moments. Thus, the intensity autocorrelation function  $g^{(2)}(\tau)$ —a fourth-order moment of the field—is related to the second order field autocorrelation function  $g^{(1)}(\tau)$  by Eq. (0.46).

The Siegert relation may fail in a number of instances. One such instance occurs when the detector area is large enough to span multiple coherence areas, or speckles [18]. Each speckle may be considered as an independent random variable. However, unlike the field, these random variables add in intensity during the detector's integration time which effectively reduces the contrast in the fluctuations [152]. In this case, Eq. (0.46) may be rewritten as

$$g^{(2)}(t) = 1 + \beta \left| g^{(1)}(t) \right|^2 \quad (0.47)$$

where  $\beta$  is typically determined experimentally and decreases with the number of speckles spanned by the detector's area.

The Siegert relation may also fail when the small scattering volumes may no longer be considered as independent, such as when the sample is undergoing a phase transition [18]. In this case, density fluctuations within the sample may be correlated by up to centimeter length scales. The effect is the same as not having enough scattering centers within the interaction volume to assume Gaussianity of the scattered field. Despite the difficulty in modeling such a process, a non-Gaussianity in the scattered field does raise the possibility of learning more about the light-matter interaction than could be learned from the Siegert relation alone.

Figure 36 illustrates how to determine the field ACF from the measured intensity ACF using the Siegert relation and homodyne detection [18]. First, the intensity ACF is divided by the baseline value  $B$  and then 1 is subtracted from the resulting curve.

$$\beta \left| g^{(1)}(\tau) \right|^2 = \frac{G^{(2)}(\tau)}{B} - 1 \quad (48)$$

The value of this new curve at  $\tau = 0$  is just  $\beta$ , the contrast of the fluctuations against the background.  $\beta$  is at most one, which corresponds to the case of measuring only a single speckle.

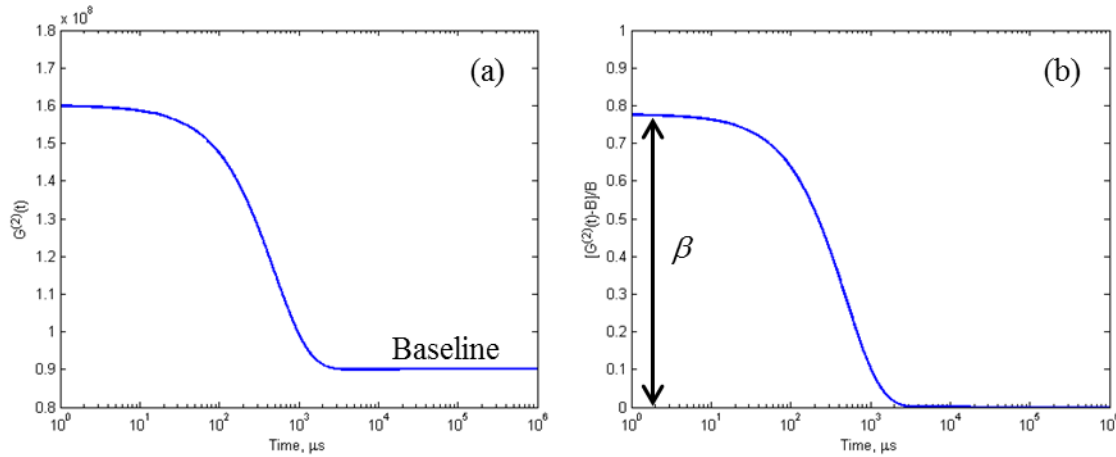


**Figure 36** Retrieval of the field ACF from an unnormalized intensity ACF using the Siegert relation. (a) The measured curve is first divided by the baseline. Then, 1 is subtracted from this curve to produce the field ACF. (b) The value of the field ACF at zero time-lag is the contrast,  $\beta$ .

### Derivation of the LC-DLS Autocorrelation Functions

In a low coherence DLS experiment like the one illustrated in Figure 10, the field incident on the detector may be written as

$$E_{det}(t) = E_0(t) + \sum_j E_s^{(j)}(t) \quad (0.49)$$

where  $E_0(t)$  is the field reflected from the fiber-sample interface and  $E_s^{(j)}(t)$  is the field scattered from the  $j$ 'th independent region within the interaction volume. Momentarily dropping the dependence on time for ease of reading, the measured intensity is written as

$$I = \left\langle \left| E_0 + \sum_j E_s^{(j)} \right|^2 \right\rangle = \left\langle |E_0|^2 + \sum_j |E_s^{(j)}|^2 + E_0 \sum_j \overline{E_s^{(j)}} + \overline{E_0} \sum_j E_s^{(j)} + \sum_j \sum_{k \neq j} \overline{E_s^{(j)}} E_s^{(k)} \right\rangle. \quad (0.50)$$

The bar over a quantity denotes its complex conjugate and  $\langle \dots \rangle$  represents an ensemble averaged quantity. Care must be taken at this step not to drop the third and fourth terms in the sum of Eq. (0.50), which at first glance may be thought to average to zero. This is because some of the cross terms will survive the averaging when determining the intensity ACF. Making the substitution

$I_0 = |E_0|^2$  and  $I_s = \sum_j |E_s^{(j)}|^2$  and reintroducing the dependency on time, the intensity ACF is

$$G^{(2)}(\tau) = \langle I(t) I(t+\tau) \rangle = I_0^2 + 2I_0 I_s + \langle [A(t) + A(t+\tau)] + B(t; \tau) + \overline{B(t; \tau)} + C(t; \tau) \rangle \quad (0.51)$$

with the three new functions in Eq. (0.51) being defined as

$$\begin{aligned} A(t) &\equiv \left[ \overline{E_0(t+\tau)} E_0(t+\tau) + \overline{E_s(t+\tau)} E_s(t+\tau) \right] \\ &\times \left( E_0(t) \sum_j \overline{E_s^{(j)}(t)} + \overline{E_0(t)} \sum_j E_s^{(j)}(t) + \sum_j \sum_{k \neq j} \overline{E_s^{(j)}(t)} E_s^{(k)}(t) \right) \\ &+ \left[ \overline{E_0(t)} E_0(t) + \overline{E_s(t)} E_s(t) \right] \\ &\times \left( E_0(t+\tau) \sum_j \overline{E_s^{(j)}(t+\tau)} + \overline{E_0(t+\tau)} \sum_j E_s^{(j)}(t+\tau) + \sum_j \sum_{k \neq j} \overline{E_s^{(j)}(t+\tau)} E_s^{(k)}(t+\tau) \right) \end{aligned} \quad (0.52)$$

$$B(t; \tau) \equiv E_0(t) \overline{E_0(t+\tau)} \sum_j \sum_k \overline{E_s^{(j)}(t)} E_s^{(k)}(t+\tau) \quad (0.53)$$

$$C(t; \tau) \equiv \sum_j \sum_k \sum_l \sum_m \overline{E_s^{(j)}(t) E_s^{(k)}(t+\tau) E_s^{(l)}(t) E_s^{(m)}(t+\tau)}. \quad (0.54)$$

Eq. (0.52) averages to zero because it contains odd-order moments of the scattered field  $E_s(t)$  [32]. Terms for which  $j \neq k$  in Eq. (0.53) are zero on average because the regions are assumed to be independent. Terms such that  $j \neq k$  and  $l \neq m$  in Eq. (0.54) average to zero for the same reason; the regions from which the fields are backscattered into the fiber are independent. Finally,  $C(t; \tau) = I_s^2$  if  $j = k = l = m$  in Eq. (0.54).

Eliminating all the terms that average to zero simplifies Eq. (0.51) considerably. It may be further simplified by introducing the field ACF specific to a scattering region  $g_j^{(l)}(\tau) = \left\langle \overline{E_s^{(j)}(t) E_s^{(j)}(t+\tau)} \right\rangle / I_s^{(j)}$  and noting that terms that are time-delayed and second order in fields originating from different regions—including the Fresnel reflection—exhibit the following decay due to the coherence length of the light source

$$\left\langle \overline{E^{(j)}(t+\tau) E^{(j)}(t) E^{(k)}(t+\tau) E^{(k)}(t)} \right\rangle \sim \gamma^2(j, k) = \exp \left[ -2(s_j - s_k)^2 / \ell_c^2 \right] \quad (0.55)$$

where  $s_j$  is the optical path length of light travelling from the fiber to region  $j$  and back and  $\ell_c$  is the coherence length of the light. Making these substitutions reduces Eq. (0.51) to

$$\begin{aligned} G^{(2)}(\tau) = & I_0^2 + 2I_0 I_s + I_s^2 \\ & + I_0 \sum_j I_j \gamma^2(0, j) \left[ g_j^{(l)}(\tau) + \overline{g_j^{(l)}(\tau)} \right] + \sum_j \sum_{k \neq j} I_j I_k \gamma^2(j, k) g_j^{(l)}(\tau) \overline{g_k^{(l)}(\tau)}. \end{aligned} \quad (0.56)$$

The introduction of Eq. (0.55) that led to Eq. (0.56) reflects the low coherence nature of LC-DLS. Scattered fields that travel further than the coherence length do not interfere with the light reflected from the tip of the fiber.

Eq. (0.56) is functionally equivalent to the expression for the intensity ACF in general optical heterodyne experiments. In these experiments, heterodyning is beneficial only for weak signals such that  $I_0 \sim I_s$  [82]. Since this is valid for most LC-DLS measurements, the last term in Eq. (0.56) may be neglected. In addition, after normalizing Eq. (0.56) by the expression  $I_0^2 + 2I_0I_s + I_s^2$ , the normalized intensity autocorrelation function is produced:

$$g^{(2)}(\tau) = 1 + \frac{2I_0I_s^{CV}}{(I_0 + I_s^{CV})^2} \text{Re} \left[ g^{(1)}(\tau) \right]. \quad (0.57)$$

Here, the substitution  $I_s \approx I_s^{CV} = \sum_j I_j \exp \left[ -2(s_0 - s_j)^2 / \ell_c \right]$  has been made and represents the intensity of the light that is collected from the coherence volume. The most significant part of Eq. (0.57) is that the field autocorrelation function is directly measured from the intensity fluctuations. For this reason, no assumptions about the Gaussianity of the field need be made in this heterodyne setup.

### On the Use of Multimode Fibers for Heterodyne Measurements

Optical mixing setups that involve beating the collected light signal with a reference beam (a.k.a. local oscillator) are known as heterodyne detection systems. These are contrasted with homodyne or “self-beating” systems where the signal is beat against itself. Heterodyne detection is capable of enhancing the fluctuations of weak signals and can directly measure the

field ACF, whereas homodyne detection is simpler to implement and its signals display higher contrast since no background from the reference is present. Signals may also contain information that corresponds to both types of detection; in this case, some prior knowledge may be needed to separate the two contributions.

When the signal is comprised of a fully developed speckle field, the intensity in each speckle is statistically independent of the intensity in every other speckle [152]. In a pure homodyne detection setup, multiple speckles that are incident on the (single pixel) detector act to reduce the contrast in the intensity fluctuations. This is because the detector effectively averages the result of multiple random processes, i.e. the intensity in each speckle. When the detected fields are scalar and Gaussian, this decreasing contrast is modeled with the parameter  $\beta$  in the Siegert relation in Eq. (0.47) and repeated here:

$$g^{(2)}(\tau) = 1 + \beta \left| g^{(1)}(\tau) \right|^2. \quad (0.58)$$

Lemieux and Durian provided an expression for  $\beta$  as the number  $N$  of discrete speckles on the detector increases [78]. This expression is

$$\beta = \frac{\sum_{j=1}^N \langle I_j \rangle^2}{\left( \sum_{j=1}^N \langle I_j \rangle \right)^2}. \quad (0.59)$$

Figure 37 plots Eq. (0.59) as a function of the number of speckles. In practice,  $\beta$  is a continuous number that lies in the range  $[0, 1]$ . From examination of Eq. (0.59) it is easy to see that  $\beta \rightarrow 0$  as  $N \rightarrow \infty$ . At some point, with an increasing number of speckles incident on the detector, the

contrast is decreased below the noise in the system and the dynamic signal, the intensity ACF, is lost. Only the average, constant intensity remains.

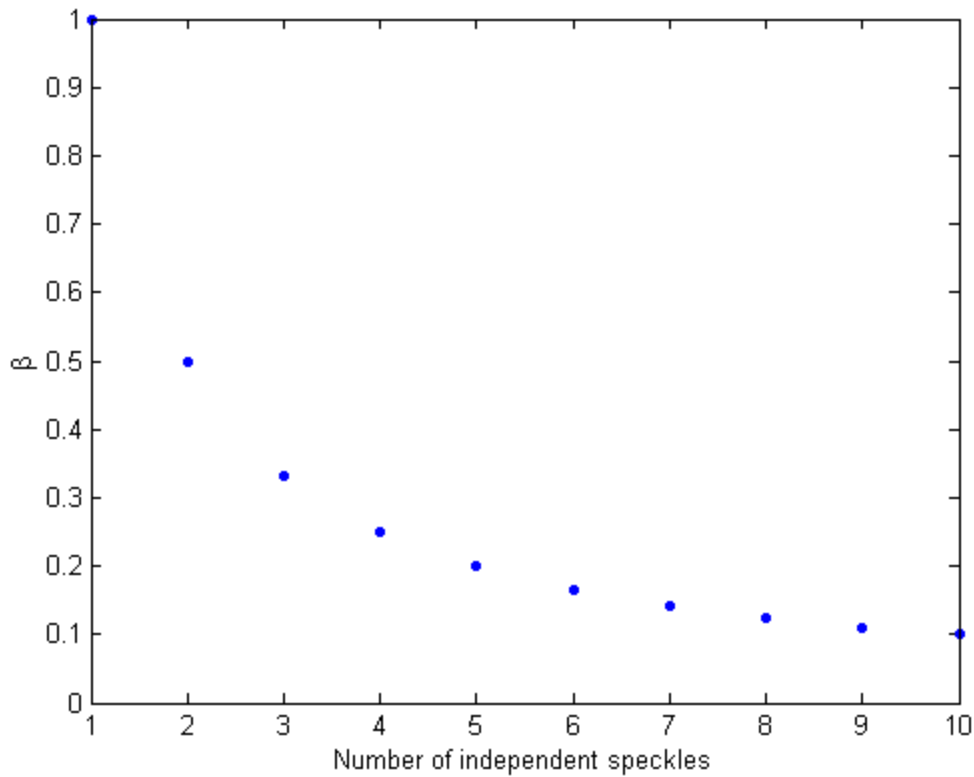


**Figure 37** The contrast in intensity fluctuations,  $\beta$ , as a function of the number of independent speckles or modes incident on the detector.

Increasing the number of speckles on the detector is equivalent to increasing the number of modes collected by the optical system. Though the contrast of the signal always decreases, a corresponding increase in the number of modes usually means more power is collected. This means that for some applications, particularly when the intensity in a single speckle is too weak and lies below the noise floor of the detector, moving to a multi-mode collection scheme will boost the signal above the noise and allow it to be detected. In this case, the loss in contrast is balanced by the experimenter having gained the ability to actually sense the signal.

This idea can be shown mathematically. Figure 38 represents a typical optical interferometer for performing heterodyne detection of the light scattered by a dynamic sample. The general expression for the normalized intensity ACF from a single-mode heterodyne setup is derived from Eq. (0.56) above [77]

$$g^{(2)}(\tau) = 1 + \frac{2I_R I_s}{(I_R + I_s)^2} \sum_j \gamma_{R,j}^2 \operatorname{Re} \left[ g_j^{(1)}(\tau) \right] + \frac{I_s^2}{(I_R + I_s)^2} \sum_j \sum_{k \neq j} \gamma_{j,k}^2 \overline{g_j^{(1)}(\tau)} g_k^{(1)}(\tau). \quad (0.60)$$

$I_R$  is the intensity of the light in the reference and  $I_s = \sum_j I_j$  is the intensity of the light that is scattered from all of the independent regions  $j$  of the sample and collected within the setup's numerical aperture.  $\gamma_{j,k}$  is a function of the difference in optical path lengths between regions  $j$  and  $k$  and represents the degree of coherence between the fields scattered from the two regions.  $g_j^{(1)}(\tau)$  is the field ACF from region  $j$ . Note also that bars here denote complex conjugates, not the “\*” symbol. If the sample is homogeneous, the field ACF is the same for each region. In this case, Eq. (0.60) reduces to

$$g^{(2)}(\tau) = 1 + \frac{2I_R I_s}{(I_R + I_s)^2} \left( \sum_j \gamma_{R,j}^2 \right) \operatorname{Re} \left[ g^{(1)}(\tau) \right] + \frac{I_s^2}{(I_R + I_s)^2} \left( \sum_j \sum_{k \neq j} \gamma_{j,k}^2 \right) \left| g^{(1)}(\tau) \right|^2. \quad (0.61)$$



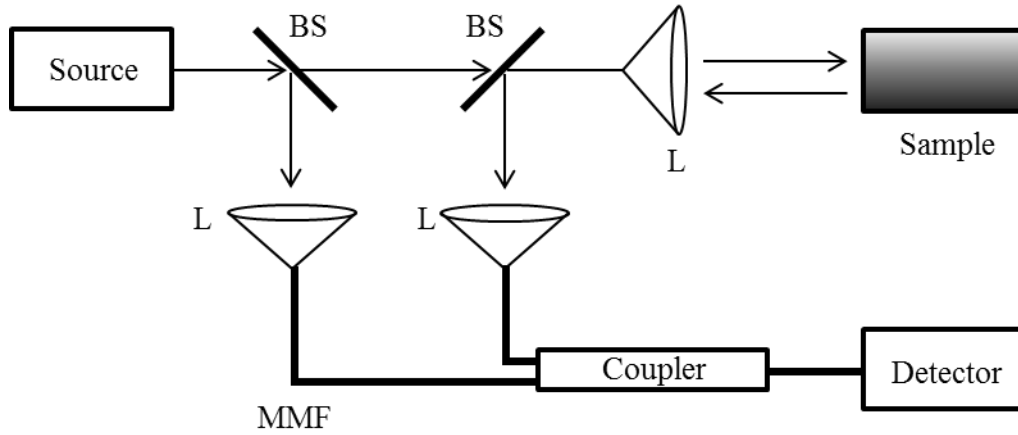


**Figure 38** A heterodyne setup employing a multi-mode fiber (MMF). The source beam is split into two directions by a beam splitter (BS). One portion of the beam illuminates the sample. The scattered light from the sample is collected by a lens (L) and focused into a MMF. The other portion of the beam serves as the reference and is also focused into a MMF where it is mixed with the light from the sample before being detected.

With the exception of the sums over the degrees of coherence between two regions  $\gamma_{j,k}^2$ , Eq. (0.61) is a general result that has been explored previously for the case of coherent illumination [82]. The second term, which is proportional to the real component of the field ACF, is known as the heterodyne component and the third term is known as the homodyne component. The two coefficients

$$\beta_{het} = \frac{2I_R I_s}{(I_R + I_s)^2} \quad (0.62)$$

$$\beta_{hom} = \frac{I_s^2}{(I_R + I_s)^2} \quad (0.63)$$

represent the contrast of the separate components to the background. Eq. (0.61) demonstrates that a degree of coherence of the source that is less than unity will decrease the contrast of the signal. Also, the presence of  $I_R$  in Eq. (0.62) means that the heterodyne component may be amplified by increasing the power in the reference beam. However, when the detected field is composed of

multiple orthogonal modes, such as those of a multi-mode fiber (MMF), Eq.'s (0.62) and (0.63) will also depend on how the reference and signal fields are distributed across those modes, as will now be demonstrated.

The reference field may be decomposed into a number  $N$  of transverse, orthogonal modes of the MMF according to

$$E_R(r, \omega, z) = \sqrt{f_R P} \sum_{j=1}^N a_j(\omega) U_j(r, \omega) \exp[i(k_j z + \phi_r)] \quad (0.64)$$

where  $P$  is proportional to the input optical power and  $f_R$  is the fraction of this power contained in the reference.  $a_j(\omega)$  is the fraction of the reference beam's energy occupied by transverse mode  $U_j(r, \omega)$ , while  $k_j$  is the propagation constant for that mode which travels a distance  $z$  to the detector after entering the MMF. The phase  $\phi_r$  is proportional to the optical path length traversed by the beam before entering the MMF. The coefficients  $a_j$  satisfy the condition

$$\sum_{j=1}^N |a_j(\omega)|^2 = 1. \quad (0.65)$$

Similarly, the scattered field is expressed as

$$E_s(r, \omega, z) = \sqrt{f_s P} \sum_{j=1}^N b_j(\omega) U_j(r, \omega) \exp[i(k_j z + \phi_s)] \quad (0.66)$$

with  $f_s$  the fraction of the input power collected by the system and the complex coefficients  $b_j$  satisfying

$$\sum_{j=1}^N |b_j(\omega)|^2 = 1. \quad (0.67)$$

$\phi_s$  is the phase associated with the beam's propagation through the system, to the sample, and back to the MMF. The length of the reference arm may be controlled in some applications such that  $\Delta\phi = \phi_s - \phi_r = 0$ .

Letting  $S(\omega)$  represent the optical power spectrum of the source, the magnitude of the heterodyne component of Eq. (0.61) may now be expressed as

$$B_{het} = 2 \int S(\omega) \int_{\omega} \overline{E_R}(r, \omega, z) E_s(r, \omega, z) d^2r d\omega. \quad (68)$$

This treatment is sufficient so long as the sample's reflectance displays no strong dependence on the optical angular frequency,  $\omega$ , which is a reasonable assumption for the types of samples considered here. It is also assumed in Eq. (68) that the reference and sample arm fibers are of equal length. Substituting Eq.'s (0.64) and (0.66) into Eq. (68) gives

$$B_{het} = 2P\sqrt{f_R f_s} \int_{\omega} S(\omega) \sum_{j=1}^N \overline{a_j}(\omega) b_j(\omega) \exp(i\Delta\phi) d\omega \quad (69)$$

The phase difference  $\Delta\phi = \omega s/c$  is related to the difference in optical path lengths  $s$  between the two arms of the interferometer, which accounts for a three dimensional sample. Ignoring the frequency dependence of the modal coefficients and performing the integration in Eq. (69) gives

$$B_{het} = 2P\sqrt{f_R f_s} \left( \sum_{j=1}^N \overline{a_j} b_j \right) \Gamma(s) \quad (0.70)$$

where  $\Gamma(s) = \int_{\omega} S(\omega) \exp(i\omega s/c) d\omega$  is the mutual coherence function of the light. If it is now allowed for the scattered light to originate from  $M$  independent regions of the sample with different path length differences between the regions and reference, Eq. (0.70) becomes

$$B_{het} = 2P\sqrt{f_R f_s} \left( \sum_{j=1}^N \overline{a_j} b_j \right) \left( \frac{1}{M} \sum_{k=1}^M \Gamma(s_k) \right). \quad (0.71)$$

Finally, recognizing that the degree of coherence may be related to the mutual coherence function through the expression [64]

$$\gamma(s) = \frac{\Gamma(s)}{\sqrt{(f_r P)(f_s P)}} \quad (0.72)$$

and normalizing by the square of the total power in the reference and signal beams gives

$$B_{het} = \frac{2f_R f_s}{(f_R + f_s)^2} \left( \sum_{j=1}^N \overline{a_j} b_j \right) \left( \frac{1}{M} \sum_{k=1}^M \gamma(s_k) \right). \quad (73)$$

This significant result is a refinement on Eq. (0.62) since it accounts for the distribution of the energy across the fiber's modes in both the reference and the signal light. It also takes into account the finite coherence length of the source light through Eq. (0.72). From Eq.'s (0.65) and (0.67), and the fact that the degree of coherence takes a maximum value of one, it's clear that

$$B_{het} \leq \beta_{het}. \quad (0.74)$$

Therefore, the contrast in the heterodyne component of the intensity ACF given by Eq. (0.61) will not exceed the case for fully coherent light. However, the amount of power that is sensed will be increased, which leads to the tradeoff between contrast and signal-to-noise ratio previously mentioned.

### DLS Measurements of Non-ergodic Materials

In a DLS experiment, it is often wished to recover the ISF, defined in Eq. (42), from  $g^{(2)}(\tau)$ . In a real experiment, the time averaged intensity autocorrelation is measured. This is defined by

$$g_T^{(2)}(\tau) \equiv \langle I(t+\tau)I(t) \rangle_T \quad (75)$$

where the subscript  $T$  denotes the time, not ensemble, average. Typically, it is assumed that the medium is ergodic, which means  $g_T^{(2)}(\tau) = g^{(2)}(\tau)$ , or that the time and ensemble averages are equal. If this is true, one can recover the medium's ISF from the time averaged intensity fluctuations.

Some microscopic properties of materials are not ergodic, however. Non-ergodicities in a material are understood to arise from the restricted motion of the individual microscopic pieces of the material due to their environment [79,153]. This “caging” or “jamming” effect on the particles often leads to subdiffusion, such as that which describes the motion of fluorescent molecules within cells [153].

If a material is not ergodic, then the measured field ACF alone will not allow one to determine the ISF. More measurements must instead be taken by scanning over the sample such that one can explore more of the particles' phase space. Instead of scanning the sample, speckles may be recorded at different scattering vectors  $q$  and combined after the measurement to retrieve the ISF instead [79]. Another alternative is to measure both the homodyne and heterodyne DLS signals with one setup [154]. Doing so retrieves the four-point susceptibility of the medium,  $\chi_4$ , which describes the spatial variability of the temporal dynamics. Still more alternatives involve

two-cell and multi-speckle techniques [80,155]. In two-cell DWS, an ergodic medium is placed after the non-ergodic one to effectively mix the light from various interaction volumes. Multi-speckle DWS is simply an extension of the work described in [79] but extended to multiply scattering samples.

While it is clear that many techniques exist to characterize non-ergodic media, they all involve an increase in the complexity of the setup to record more information. This simple fact must be kept in mind when measuring materials with complex spatio-temporal dynamics.

## **APPENDIX B: TRACER PARTICLE MICRORHEOLOGY USING DYNAMIC LIGHT SCATTERING**

### Measuring the Viscoelasticity of Complex Fluids

Complex fluids comprise a range of materials that find applications in biopharmaceuticals, cosmetics, food, and many industrial products and processes [156]. These fluids typically exhibit deviations from Newtonian behavior. (If a fluid is Newtonian it means that the shear stress in a plane through the fluid is linear with the strain rate.) Just a few examples of complex fluids are dense colloidal suspensions, gelatin, and human blood.

Viscoelasticity is a common property used to describe the behavior of a complex fluid [156]. This description is useful because it is a macroscopic one that classifies different materials independently of their microscopic makeup. Other than simply classifying a material, the viscoelastic parameters of a fluid serve an important role for sensing changes in the microscopic dynamics, such as the response of a cell to some drug or the clotting of blood [157,158]. Particles diffusing in a viscoelastic fluid are subdiffusive, meaning that the MSD takes a power law exponent of  $\alpha < 1$ , which is easily measured with LC-DLS.

### *The Viscoelastic Moduli*

First the parameters that describe a viscoelastic medium must be defined. Consider a piece of material like that depicted in Figure 39. A harmonic shear force  $F(\omega)$  is applied to one side of the material, which causes this side to expand in length from  $L_0$  to  $\Delta L_0$ .

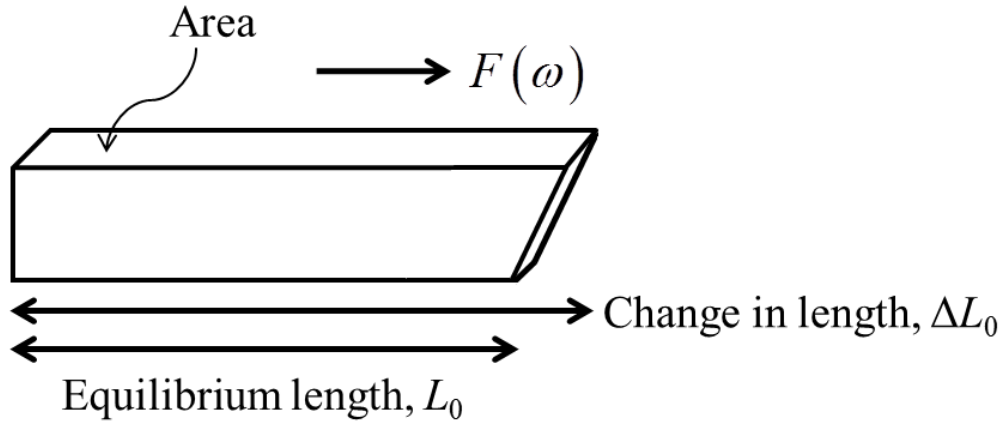


**Figure 39** A piece of material undergoes a shear stress  $F(\omega)$ , which causes a strain, or change in length of  $\Delta L_0$ .

The viscoelastic moduli relate the shear stress,  $\sigma$ , to the strain,  $\varepsilon$ , of the fluid. For a harmonic strain  $\varepsilon = \varepsilon_0 \sin(\omega t)$ , the stress in the material takes the form  $\sigma = \sigma_0 \sin(\omega t + \delta)$ , with  $\delta$  representing the phase delay between the strain and stress. From these relationships, the definition of the (linear) viscoelastic moduli are defined as

$$\begin{aligned} G'(\omega) &= \frac{\sigma_0}{\varepsilon_0} \cos(\delta) \\ G''(\omega) &= \frac{\sigma_0}{\varepsilon_0} \sin(\delta) \\ G^*(\omega) &= G'(\omega) + iG''(\omega). \end{aligned} \tag{76}$$

The storage (or elastic) modulus,  $G'(\omega)$ , represents the portion of the stress that's in-phase with the strain. Intuitively, it represents the amount of energy stored in the material as it's sheared. The loss modulus,  $G''(\omega)$ , is in quadrature with the applied strain and describes the energy dissipation by the fluid. The dynamic viscosity is related to the viscoelastic modulus through the expression



$$\eta^* = \frac{G^*}{i\omega} \quad (77)$$

and at zero frequency represents the viscosity that is usually used to describe a fluid [156].

### *Thermal Motion of Particles in a Complex Fluid*

The viscoelastic parameters of a fluid may be determined by the thermal motion of tracer particles suspended in it. Consider a single, microscopic particle embedded in the fluid and excited by thermal (i.e. random) forces. The equation of motion—in this case known as a generalized Langevin equation—is

$$m \frac{dv(t)}{dt} = \xi(t) - \int_0^t \gamma(t-t') v(t') dt' \quad (78)$$

where  $m$  is the particle's mass and  $v(t)$  is the velocity [26].  $\gamma(t)$  represents a viscoelastic memory function that takes into account both the viscosity and energy stored by the fluid. For a particle in a purely viscous fluid such as water,  $\gamma(t) = \gamma_0 \delta(t)$  and Eq. (78) simplifies to its more recognizable and simpler form.  $\xi(t)$  denotes the random thermal forces experienced by the particle and is described by the fluctuation-dissipation theorem [48]. The presence of a memory function  $\gamma(t)$  in Eq. (78) that is not delta-correlated modifies the behavior of  $\xi(t)$  such that  $\langle \xi(t+\Delta t) \xi(t) \rangle = k_B T \gamma(\Delta t)$  where  $k_B$  is Boltzmann's constant,  $T$  is the absolute temperature, and  $\langle \dots \rangle$  denotes an ensemble average [26].

The particle MSD is obtained from this expression as follows. Taking the unilateral Laplace transform of Eq. (78) produces [129]

$$ms\tilde{v}(s)-m\tilde{v}(0)=\tilde{\xi}(s)-\tilde{\gamma}(s)\tilde{v}(s). \quad (79)$$

Here, a tilde ( $\sim$ ) over a quantity represents its Laplace transform and  $s$  is the Laplace frequency.

Multiplication of Eq. (79) by  $\tilde{v}(0)$  and ensemble averaging results in

$$ms\langle\tilde{v}(s)\tilde{v}(0)\rangle-m\langle\tilde{v}^2(0)\rangle=\langle\tilde{\xi}(s)\tilde{v}(0)\rangle-\tilde{\gamma}(s)\langle\tilde{v}(s)\tilde{v}(0)\rangle. \quad (80)$$

It can be shown that  $\langle\tilde{\xi}(s)\tilde{v}(0)\rangle=0$  [18]. Furthermore the equipartition of energy theorem states that  $m\langle\tilde{v}^2(0)\rangle=3k_B T$  for a particle in three dimensions [132]. Making these substitutions and rearranging Eq. (80) gives

$$[ms+\tilde{\gamma}(s)]\langle\tilde{v}(s)\tilde{v}(0)\rangle=3k_B T. \quad (81)$$

The final step is to link the velocity autocorrelation function to the particle's MSD. In the time domain, the particle's MSD is related to the velocity autocorrelation function by [18]

$$\langle\Delta R^2(t)\rangle=2\int_{x=0}^t\int_{y=0}^x\langle v(y)v(0)\rangle dydx. \quad (82)$$

The unilateral Laplace transform of this expression is

$$\langle\Delta\tilde{R}^2(s)\rangle=\frac{2}{s^2}\langle\tilde{v}(s)\tilde{v}(0)\rangle. \quad (83)$$

Substituting Eq. (83) into Equation (81) and rearranging produces

$$\langle\Delta\tilde{R}^2(s)\rangle=\frac{6k_B T}{s^2[ms+\tilde{\gamma}(s)]}. \quad (84)$$

This result, which was obtained by Mason and Weitz [26] links the MSD to the memory function  $\tilde{\gamma}(s)$ . A LC-DLS measurement, which by nature measures the tracers' MSD (c.f. Eq. (22)), thus provides enough information to infer  $\tilde{\gamma}(s)$ . The last step is to link  $\tilde{\gamma}(s)$  to the viscoelastic moduli and is described next.

### *Examples of Viscoelastic Measurements using LC-DLS*

Mason [90] used Eq. (84) to show that the complex viscoelastic modulus was related to the particle MSD in the Fourier domain according to

$$\begin{aligned} G'(\omega) &= |G^*(\omega)| \cos(\pi\theta(\omega)/2) \\ G''(\omega) &= |G^*(\omega)| \sin(\pi\theta(\omega)/2) \\ |G^*(\omega)| &\approx \frac{k_B T}{\pi r \langle \Delta R^2(1/\omega) \rangle \Gamma[1+\theta(\omega)]} \end{aligned} \quad (85)$$

with  $\theta$  being equivalent to the log-log slope of the MSD in the time domain and  $r$  the particle radius. Since the MSD may be determined the PSD of scattered intensity fluctuations by Eq. (23), then Eq. (85) may be used in conjunction with this measurement to give  $G^*(\omega)$ .

Figure 40 shows the result of determining the moduli from the PSD of intensity fluctuations from a 4% solution of 100,000 molecular weight PEO in water. The low frequency scaling is typical of standard viscoelastic moduli [128]. The moduli were obtained in the same manner as Ref. [128]. More complex behaviors of  $G'(\omega)$  and  $G''(\omega)$  are expected for fluids whose microscopic details vary with macroscopic parameters, such as temperature and pressure.

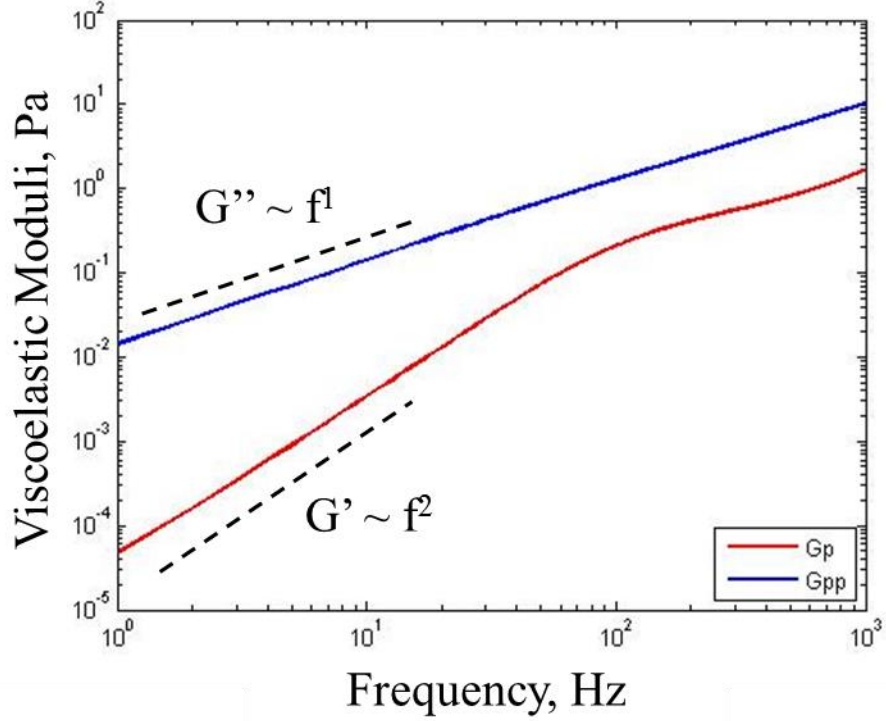


**Figure 40** Viscoelastic moduli calculated for a 4% solution of 100,000 molecular weight PEO in water. The low frequency scaling is denoted by the dashed lines and is expected from theory.

### *Tracer Particle Inertia*

Eq. (84) is the mean-squared displacement of an independent particle undergoing Brownian motion in the Laplace domain. Repeated here, it is

$$\langle \Delta \tilde{R}^2(s) \rangle = \frac{6k_B T}{s^2 [ms + \tilde{\gamma}(s)]} \quad (0.86)$$

where  $k_B$  is Boltzmann's constant,  $T$  is the absolute temperature,  $m$  is the particle's mass, and  $\tilde{\gamma}(s)$  is the memory function that describes the viscoelastic properties of the material. Eq. (0.86) reduces to the Stokes-Einstein relation when the particle's mass is negligible. This is more easily seen in the Fourier domain by letting  $s = j\omega$  and writing the complex memory function as a sum

of its real and imaginary parts,  $\tilde{\gamma} = \gamma' + j\gamma''$ . After multiplying and dividing by the fraction's complex conjugate, the following results:

$$\langle \Delta \tilde{R}^2(j\omega) \rangle = \left( \frac{6k_B T}{\omega^2} \right) \frac{\gamma' - j(m\omega + \gamma'')}{(\gamma')^2 + (m\omega + \gamma'')^2}. \quad (0.87)$$

The inertial term  $m\omega$  may be neglected from the denominator when either  $\gamma'$  or  $\gamma''$  are much greater than  $m\omega$ . In the numerator, the term must be small enough that its removal from the equation causes a negligible change in the angle of the phasor that represents the mean-squared displacement.

The following example is a useful tool for deciding when the particle's inertia is negligible to the expression for the mean-squared displacement. For a suspension of spheres in a purely viscous fluid,  $\gamma'' = 0$  and  $\gamma' = 6\pi\eta r$ , with  $\eta$  representing the fluid viscosity and  $r$  the sphere radius. Assuming that the particle has a uniform density  $\rho$ , then by Eq. (0.87) and the relation between mass and density, the particle inertia may be neglected so long as the following condition is satisfied:

$$r^2\omega < \frac{9\eta}{2\rho}. \quad (0.88)$$

Inequality (0.88) is depicted on a log-log scale in Figure 41 for polystyrene spheres in water. The black solid line represents the curve  $r^2\omega = 0.1(9\eta/2\rho)$ , with the factor of 0.1 being arbitrarily chosen. For points  $(r, \omega)$  below this line, the sphere inertia may be neglected from Eq. (0.86).

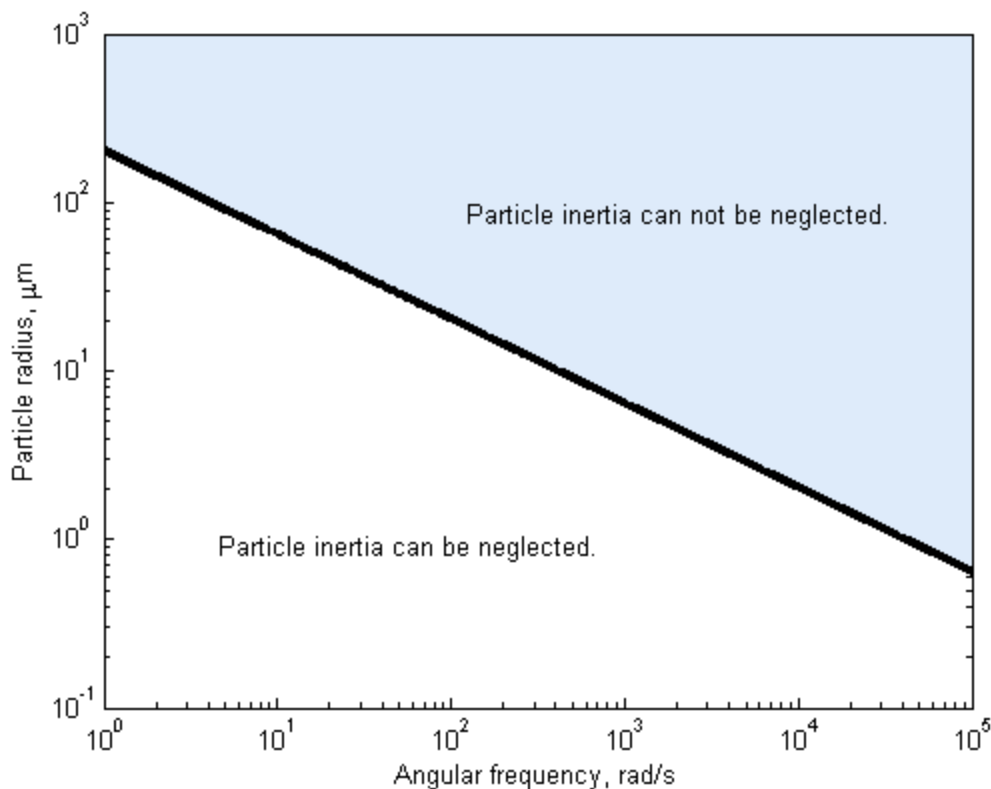


**Figure 41** A plot describing for what frequencies and masses inertia may be ignored in a suspension of polystyrene spheres in water. The shaded region denotes the combinations of radius and frequency for which the inertial term in the expression for the mean-squared displacement may not be neglected for precise modeling.

Figure 41 must be used only as a rough rule of thumb since the velocity ACF of the particle is in fact heavy-tailed [159,160]. This means that inertial effects may last a few orders of magnitude longer than the characteristic time of decay of the ACF.

## **APPENDIX C: DIFFERENCE IMAGING AND VARIANCE-TIME PLOTS**

### Determining a Preferred Direction of Motion using Difference Imaging

The following provides details about the calculation of the variance-time plots, the decay times of their autocorrelations, and the numerical simulations that validated our analysis.

#### *Variance-Time Plots*

Let  $I(i, j; t)$  represent the intensity of the real, grayscale image of a pixel in the  $i$ 'th row and  $j$ 'th column at a time  $t$ . The real images were first converted to the double datatype in Matlab. Following this, the difference images were then calculated according to

$$D(i, j; t; \Delta t) = I(i, j; t + \Delta t) - I(i, j; t) \quad (89)$$

where  $\Delta t$  is a fixed time interval (ten minutes in this work). After subtraction, the values for the pixel intensities were rescaled onto the range [0 255]. Before rescaling, a difference of 0 would denote no change in the intensity between the two images. After rescaling, this occurred at a value of 127, halfway between the minimum and maximum values of the images' bit depths.

The variance of the intensity values of each row and column of the difference images was calculated according to the main text. This operation is presented pictorially in Figure 42. The calculated variance values for the rows and columns were stacked vertically to form a single column matrix at that particular time. A series of  $K$  real images produced  $2(K-1)$  single column matrices; the factor 2 is present because the operation occurs over both rows and columns, while there are  $K-1$  difference images calculated from  $K$  real images. The columns were then grouped horizontally to form two variance-time (VT) plots—one for the rows and one for the columns. The horizontal axis of the VT plots denotes the time lag.



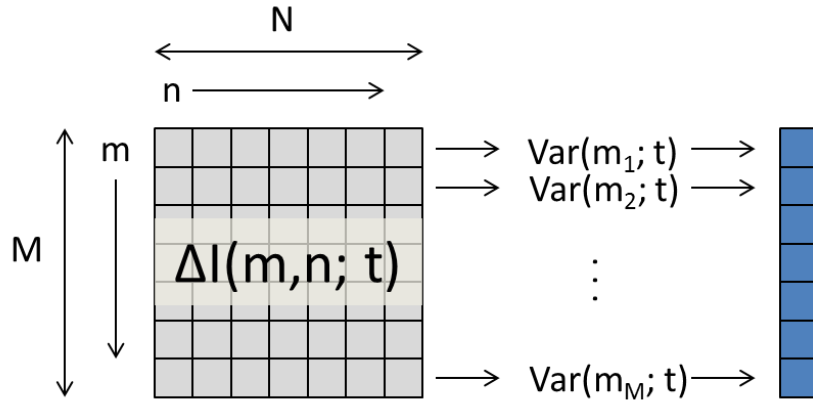


**Figure 42** This picture represents the calculation of the variance for each row of a single difference image. The value of the variance for each row is placed into a single pixel and these pixels are stacked to form a single column matrix for the particular time  $t$ .

Figure 43 displays two VT plots calculated from the difference images of Schwann cells on a narrow portion of a tapered fiber. The time evolution is plotted across the horizontal axis whereas the row or column coordinate is plotted along the vertical axis, respectively. Colors encode the value of the variance—red is high and blue is low. Intuitively, the variance calculated across the rows displays features with much more persistence in time than the variance calculated across the columns. As noted in the main text, this structure indicates a preferential motion of the cells along the rows, rather than the columns. A way to quantify this structure is given in the next section.

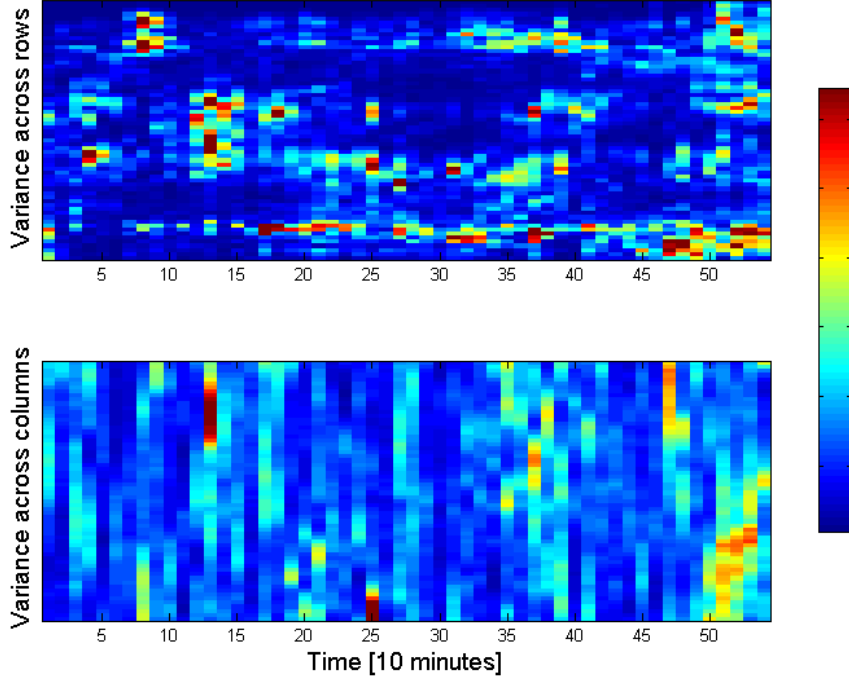


**Figure 43** VT plots calculated across the rows (top) and columns (bottom) of a difference image. The time of the latest image used to calculate a particular difference image is marked along the x-axis. The persistence of features along the x-axis in the VT plots for the rows indicates a preference for the cells to move in this direction.

### *Autocorrelations of VT Plots*

To determine a degree of horizontal structure, and consequently a preferred direction of motion of the cells from the VT plots, I computed their horizontal autocorrelation. The autocorrelation of the VT plots in the horizontal direction is given by

$$A(\tau) = \left( \frac{T}{T-\tau} \right) \frac{\sum_{t=1}^{T-\tau} \sum_{i=1}^M [V(i,t) - \bar{V}(i)] [V(i,t+\tau) - \bar{V}(i)]}{\sum_{t=1}^T \sum_{i=1}^M [V(i,t) - \bar{V}(i)]^2}, \quad \tau = 0, 1, \dots, T-1 \quad (90)$$

where  $T$  is the total number of columns in the VT plot,  $i$  represents the vertical coordinate of the VT plot,  $V(i,t)$  is the value of the VT map in the  $i$ 'th pixel and time  $t$ , and  $\bar{V}_i$  is the average

variance calculated across the  $i$ 'th row. By first averaging over the rows, I eliminate distortions in the apparent size of the cells near the edge of fiber that are caused by its curvature; for every cell moving away from the fiber's axis, there is, on the average, one moving towards it.

Figure 44 displays the autocorrelation of the VT plots at each fiber radius for (a) the rows and (b) the columns. The decay time of the autocorrelations, defined as the time at which the curves reach a value of 0.5, is useful indicator for determining the degree of “horizontal” structure in the VT maps.

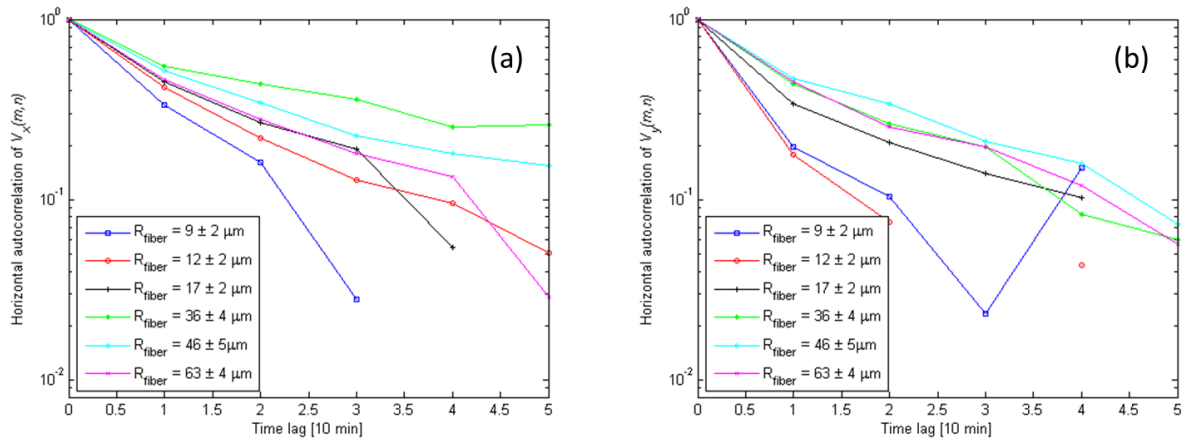


**Figure 44** Horizontal autocorrelations of the VT maps along the a) rows and b) columns.

### *Decay Times of the Autocorrelation Curves*

Figure 45 is a plot of the decay times calculated from the curves in Figure 44. Intuitively, they represent the amount of time required for the VT plots to become random; a longer decay time means the cells are preferentially moving in that direction as opposed to the other. The behavior of the data points with time is explained below in the section on the simulations and is the evidence for our conclusions. The decay times were calculated by finding the line connecting

the first two data points. From this line the time at which its value reached 0.5 was marked as the decay time. When the decay times have become equal, the motion has become isotropic.

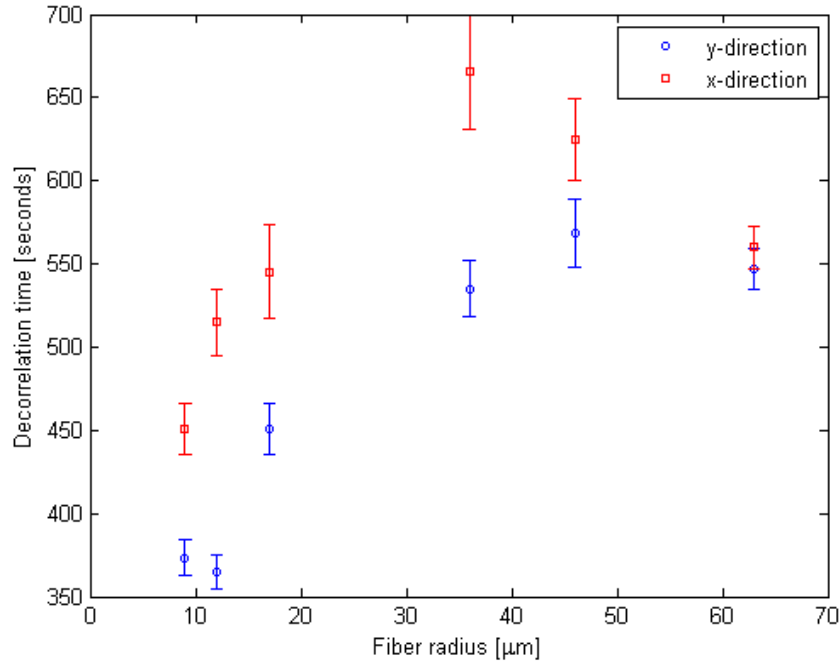


**Figure 45** Decay time of the autocorrelations of the VT plots vs. fiber radius. “x-direction” refers to the autocorrelation of the VT plots of the rows and “y-direction” to the VT maps of the columns. The overlapping data points at a fiber radius of 63  $\mu\text{m}$  indicate that the statistics of the cells’ motions are the same in both the x- and y-directions. Error bars represent the standard errors of the decorrelation times.

#### *Determination of the Errorbars*

The errorbars in Figure 45 were determined in part by the formula

$$\sigma_{A_{x,y}}(\tau) = \sqrt{\frac{n - \tau}{n(n + 2)}} \quad (91)$$

where  $A_{x,y}$  represents the autocorrelation in the x or y direction,  $\tau$  is an integer denoting the lag time, and  $n$  is the number of points in the time series. Eq. (91) is the standard deviation of the points of an autocorrelation of a zero-mean process whose errors are independently and

identically distributed. The last two conditions were checked in the simulations that follow and the first condition, that the VT plots were zero mean, was ensured by subtracting the mean of a row or column of a VT plot from that corresponding row or column. The errors found from Eq. (91) were used in determining the errors in the decay time of the autocorrelation curves in Figure 44, which appear in Figure 45.

The decay times were calculated by fitting a line to the first two data points of the autocorrelation curves. The point at which the fitted line reached a value of 0.5 was marked as the decorrelation time. Its error was determined by the error in the slope of the line due to the uncertainty in the autocorrelation data. The error in the slope,  $m$ , is given by

$$\Delta m = \sqrt{\sigma_{A_{x,y}}^2(0) + \sigma_{A_{x,y}}^2(\tau)} \quad (92)$$

with  $\sigma_{A_{x,y}}^2(\tau)$  defined above. The error in the decay time was

$$\Delta \tau = \Delta m \left( \frac{\tau}{m} \right) / \sqrt{B} \quad (93)$$

Here,  $B$  represents the number of rows or columns that were included in the averaged autocorrelation curves in Figure 44 divided by the average pixel size of a cell.

### *Simulations of Brownian Cells*

Single cell tracking could not have been implemented in our raw images due to the geometry and optical properties of the fiber. For this reason, I validated my technique with a numerical simulation of motile cells. Beyond validation, the simulations also helped to determine

the relation between the decorrelation times of the VT plots and some of the parameters governing the motion of the cells.

Briefly, a set number of cells were assigned a random starting location on a grid. Each cell was then independently assigned random trajectories along the x- and y-directions following a standard normal distribution multiplied by a factor  $k$ , where  $k$  represents the root-mean-square (RMS) step size of the cell. The cells' sizes could also be set independently along the x- and y-directions. The cells' centers-of-mass were then translated along their randomly assigned trajectories. An image marking their location and a new trajectory for each cell was generated at each iteration of the simulation loop. The difference images were calculated at each step as detailed above.

Figure 46 displays the decorrelation times for the VT plots along the x- and y-directions of the difference images from the simulations. The RMS displacement of the cells along the y-direction was varied, keeping the RMS displacement along the x-direction fixed at 10 pixels. The cells were a square 3x3 pixels in size. 20 cells were randomly assigned starting locations on a 256x256 pixel grid and 256 loops of the simulation were run.

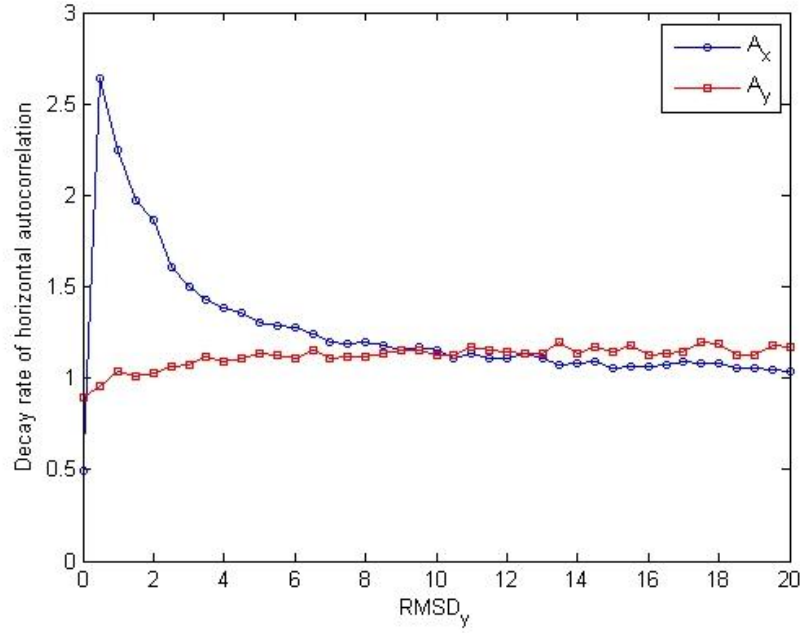


**Figure 46** Decorrelation times of the VT plots for images generated by simulated Brownian cells. The RMS displacement along the x-direction was fixed at 10 pixels per loop iteration. The RMS displacement along the y-direction was varied from 0 to 20 pixels/iteration.

The behavior of Figure 46 reveals several key things for interpreting the behavior of the VT plots. For one, the decorrelation times are equal once the RMS step sizes in the two independent directions are equal ( $\text{RMSD}_x = \text{RMSD}_y = 10$  in this case). Second, the decorrelation time along the x-direction displays a pronounced peak when the RMS step size along the y-direction is roughly half the width of the cell. This behavior was observed for a wide variety of cell sizes, shapes, and RMS displacements within the simulations. Finally, while not shown explicitly by Figure 46 alone, the width of the peak of the  $A_x$  curve in Figure 46 is governed by shape anisotropy of the cells in the simulation, i.e. the ratio of their widths to their heights.

### *Determination of the RMS displacement of the cells*

The maximum RMS displacement of  $45 \pm 2 \text{ } \mu\text{m}$  per hour along each independent direction given in the main text was determined by noting that the maximum decorrelation times observed in the simulations occurred when the RMS step size was roughly one half of the average linear size of the cells and the motion was isotropic. Measurements on a large number (~70) different Schwann cells produced an average linear size of  $15.0 \pm 0.7 \text{ } \mu\text{m}$ . Thus, the maximum RMS step size is  $7.5 \pm 0.7 \text{ } \mu\text{m}$  per ten minutes, or  $45 \pm 2 \text{ } \mu\text{m}$  per hour for isotropic motion. The motion of the cells became isotropic as indicated by the two data points at the largest fiber radius in Figure 45. The RMS displacement along the fiber's axis was assumed not to change as the radius increased.



## **APPENDIX D: DETERMINATION OF A DISORDERED PHOTONIC CRYSTAL'S DENSITY OF STATES**

### The Density of States for Ordered and Disordered Photonic Crystals

The density of states (DOS) is a measure of the number of modes that may propagate inside a photonic crystal. More precisely, it counts the number of directions that a plane wave of a given frequency may propagate without being reflected back out of the crystal. A bandgap is a range of wavelengths for which no directions of propagation are allowed; any plane wave incident on the crystal from outside with one of these wavelengths is completely reflected. A pseudogap is a range of wavelengths with an anomalously low, but not zero, number of propagation directions. A measure of what “anomalously low” means may be obtained by comparing a DOS curve to the expected parabolic scaling of the DOS with the frequency of light [2]. Regions where the DOS lay below this curve are pseudogaps.

Localized modes are not included in the density of states because they do not propagate. Coupling between propagating modes and localized modes in a pseudogap is responsible for the scale-dependent diffusion of light observed in disordered photonic crystals [9,63,109,110].

For disordered crystals, a DOS was computed by taking an unweighted average of the DOS curves obtained from the same crystal structure with various input parameters, such as unit cell size. Any correlation in bandgaps or pseudogaps in the individual, simulated structures will appear in the average DOS curves and are labeled as gaps for these disordered structures.

### The Brillouin-Zone Representation of an FCC Lattice

The photonic crystals that were investigated, in the absence of disorder, were intended to have a face-centered cubic (FCC) lattice of air spheres in an amorphous silicon background. This type of structure is known as an inverse opal. Two unit cells of an inverse opal are sketched in

Figure 47.  $a$  is the lattice constant,  $r$  is the radius of the air spheres, and  $R$  is the radius of the silicon spheres.

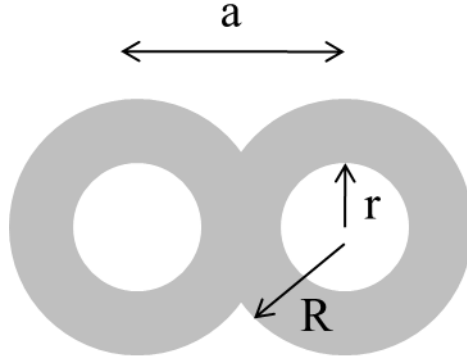


**Figure 47** An illustration of the relevant parameters that describe the photonic crystal explored in the text.  $a$  is the lattice constant,  $r$  is the radius of the air spheres, and  $R$  is the radius of the silicon spheres.

The Brillouin zone representation of a crystal is a useful way to describe the arrangement of the objects in the crystal and will aid in computing the DOS. To simplify and generalize the wording, the objects that are arranged in the crystal are the centers of the silicon/air spheres. Fundamentally, the first Brillouin zone describes a unit cell in the Fourier transform of the crystalline lattice.

The first Brillouin zone consists of all the points in a volume that must be specified to unambiguously identify the crystalline lattice. Once these locations are specified, all the other points in the reciprocal lattice may be obtained from symmetry arguments and knowledge of the lattice constant. The first Brillouin zone of an FCC lattice is pictured in Figure 48.

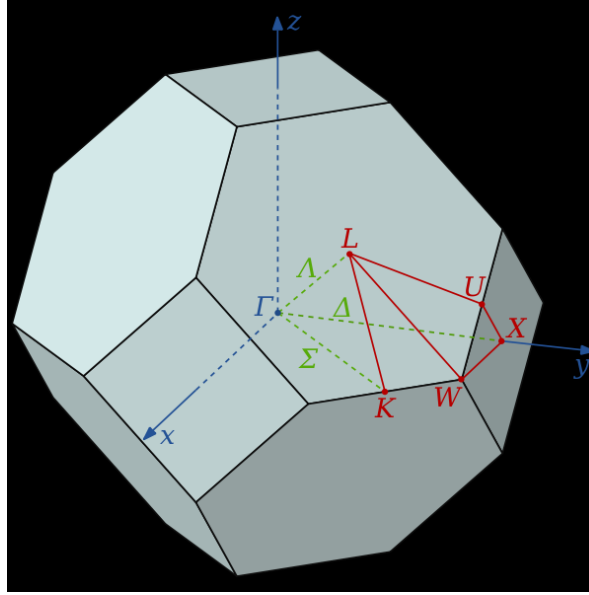


**Figure 48** (Image credit: Wikipedia) The first Brillouin zone of an FCC lattice. Points within the volume that are bounded by the gray planes lie within the zone. Roman letters are used to denote special crystallographic vertices on the zone boundary and Greek letters denote special directions in reciprocal space.  $\Gamma$  denotes the origin of reciprocal space.

The reciprocal lattice vectors serve as a convenient basis for describing the points in the Brillouin zone. The reciprocal lattice vectors of a FCC crystal are given by

$$\begin{aligned}\mathbf{b}_1 &= \frac{2\pi}{a}(\hat{\mathbf{x}} + \hat{\mathbf{y}} - \hat{\mathbf{z}}) \\ \mathbf{b}_2 &= \frac{2\pi}{a}(-\hat{\mathbf{x}} + \hat{\mathbf{y}} + \hat{\mathbf{z}}) \\ \mathbf{b}_3 &= \frac{2\pi}{a}(\hat{\mathbf{x}} - \hat{\mathbf{y}} + \hat{\mathbf{z}})\end{aligned}\tag{94}$$

and are also the basis vectors of a real-space body-centered cubic (BCC) lattice. (In other words, the 3D Fourier transform of an FCC lattice is a BCC lattice.)

### *Determining the Density of States using the First Brillouin Zone*

Points within the first Brillouin zone of an FCC reciprocal lattice may be numerically generated by randomly selecting points within a cube of length  $2\pi/a$  with one corner at the origin and all other points in the octant defined by positive or zero coordinate values. All points that lie above the plane  $x + y + z = 1.5(2\pi/a)$  are removed from this list since they do not lie within the first Brillouin zone. Schematically, these points lie in one eighth of the volume illustrated in Figure 48. These points are then transformed to the basis of reciprocal lattice vectors using the matrix

$$\frac{2\pi}{a} \begin{pmatrix} 0.5 & 0.5 & 0 \\ 0 & 0.5 & 0.5 \\ 0.5 & 0 & 0.5 \end{pmatrix}. \quad (95)$$

The corresponding frequency of an electromagnetic plane wave traveling in the direction defined by any one of these numerically-generated points is obtained by eigenvalue solvers such as MIT's Photonic Bands [63]. These frequencies are denoted by  $\omega(\mathbf{k})$  and depend on the structure of the photonic crystal and its material properties.

The expression for the DOS in a photonic crystal is given by

$$\text{DOS}(\omega) = \sum_{\mathbf{k}, \text{1BZ}} \delta[\omega - \omega(\mathbf{k})]. \quad (96)$$

The DOS is essentially a histogram of the number of plane waves propagating in arbitrary directions with frequency  $\omega$ . The more plane waves that propagate with a given frequency, the higher the DOS for that frequency of light.

### *Density of States in the Observed Photonic Crystal*

The DOS curve in Figure 22 is an average over 13 different DOS corresponding to slightly different inverse opal parameters. The parameters are the refractive index of silicon ( $n$ ), the ratio of the air sphere radius to the lattice constant ( $r/a$ ) and the ratio of the silicon sphere radius to the lattice constant ( $R/a$ ). They were chosen at random and are realistic for this particular photonic crystal design. These parameters are listed in Table 1.

**Table 1** List of parameter values used for the DOS calculation.

Refractive index, $n$	Air sphere radius, $r/a$	Silicon sphere radius, $R/a$
3.4	0.360	0.390
3.6	0.360	0.390
3.6	0.370	0.400
3.6	0.370	0.410
3.6	0.380	0.410
3.4	0.365	0.390
3.6	0.365	0.390
3.6	0.365	0.410
3.6	0.375	0.400
3.4	0.360	0.400
3.6	0.360	0.400
3.6	0.355	0.400
3.6	0.365	0.390

The point of averaging over the DOS for these different structures was to approximate the DOS in a disordered photonic crystal. The bandgap in many of these structures contributed to the pseudogap in Figure 22, and it was this pseudogap that was responsible for the observed scaling effects.

## **APPENDIX E: THEORY OF DEGENERATE IMAGE MIXING AND SPARSE RECONSTRUCTION**



### Theory of Degenerate Image Mixing

Degenerate image mixing refers to the process of encoding images such that they cannot be decoded by traditional means (i.e. with a linear algorithm) when they are superposed. The reason for doing so typically involves an advantage in the measurement process. In this case, images were reconstructed by capturing fewer mixed images than the number of reconstructed ones.

Here this type of mixing was realized by 1) encoding different regions from a scene onto different polarization states, 2) imaging these regions through a polarization analyzer and onto a CCD such that each of the comprising images filled the entire area of the sensor, 3) calculating the Stokes parameters of the resulting mixed image on the CCD, and 4) computing the original scenes. It is important to note that the scene is illuminated with incoherent light so that the images corresponding to different regions are superposed in intensity. Additionally, the scene is assumed to be unpolarized. The proposed scheme for degenerate image multiplexing and demultiplexing is illustrated in Figure 23.

The theory that follows was originally presented in Ref. [120].

#### *Polarization Encoding and Multiplexing*

Let  $\mathbf{x} = (x_1, x_2, \dots, x_N)^T$  represent the values of the intensity in a scene that is partitioned into  $N$  sections. These partitions can be superposed in intensity according to a mixing matrix  $\mathbf{A}$  such that

$$\begin{pmatrix} y_1 \\ y_2 \\ \vdots \\ y_M \end{pmatrix} = \begin{pmatrix} A_{1,1} & A_{1,2} & \cdots & A_{1,N} \\ A_{2,1} & A_{2,2} & \cdots & A_{2,N} \\ \vdots & \vdots & \ddots & \vdots \\ A_{M,1} & A_{M,2} & \cdots & A_{M,N} \end{pmatrix} \begin{pmatrix} x_1 \\ x_2 \\ \vdots \\ x_N \end{pmatrix} \quad (97)$$

The columns of the matrix  $\mathbf{A}$  contain the Stokes parameters that represent the polarization state that each image is encoded onto. By the linearity of Stokes vectors, it follows that the vector  $\mathbf{y} = (y_1, \dots, y_M)^T$  then contains the Stokes parameters of the superposed image, which can be measured using any number of polarimetric techniques [114]. Further, let the components  $\{x_1, x_2, \dots, x_N\}$  and  $\{y_1, \dots, y_N\}$  of  $\mathbf{x}$  and  $\mathbf{y}$  be sectioned into two dimensional arrays of pixels with indexes  $(i, j) \in (1, \dots, L_1) \times (1, \dots, L_2)$  with  $L_1$  and  $L_2$  representing the number of pixels along each dimension. In other words,  $x_n(i, j)$  and  $y_n(i, j)$  are images. Eq. (1) can then be further refined such that it becomes a point-wise operation, i.e.  $\mathbf{y}(i, j) = \mathbf{A}(i, j)\mathbf{x}(i, j)$ .

Given the  $M$  measured Stokes parameters, one may wish to reconstruct the original images contained in the vector  $\mathbf{x}$ . So long as  $M \geq N$ , the reconstruction can be accomplished by means of a linear algorithm such as Gaussian elimination. However, if  $M < N$ , as is the case for the system proposed herein, Eq. (97) becomes an underdetermined system of equations and must be solved by other means. This case is especially pertinent to polarization multiplexing schemes because at most four independent measurements can be made.

### *Transformation to a Sparse Basis*

In the underdetermined case, linear algorithms cannot reconstruct the original images contained in  $\mathbf{x}$  from a given set of measured Stokes parameters because for any solution  $\hat{\mathbf{x}}$  to Eq.

(1),  $\hat{\mathbf{x}} + \mathbf{N}\mathbf{b}$  is also a solution where  $\mathbf{N}$  is the null space of  $\mathbf{A}$  and  $\mathbf{b}$  is an arbitrary vector. To estimate the inputs in this case, additional assumptions must be made on the nature of the image sources. One powerful assumption is that the source images are sparse, either in the image domain or in a conveniently selected representation. An image is said to be sparse when it contains regions of zero or nearly zero intensity more than might be expected from its variance. Such a signal has a probability density function or distribution of intensity values with a sharp peak at zero and fat tails.

Sparsity in the image domain exists only for a limited class of images, such as those that contain a few discrete objects against a uniform background. However, most images can be transformed into a domain such that only a small number of the transform coefficients are of appreciable magnitude. For example, smooth images are sparse in the 2D-Fourier domain. A large class of real-life images can be considered piece-wise smooth, resulting in sparse representations in wavelet dictionaries. An even larger class of images that contain chirps or textures can be sparsified with wavelet packets representations. Theoretically, for any class of images a sparse basis exists and can be found using adaptive learning algorithms such as the *basis pursuit* [116].

The image mixing problem represented by Eq. (97) can be sparsified in the following manner. Each image source is vectorized by reshaping the  $L = L_1 \times L_2$  pixels into a single column vector,  $\mathbf{x}_q$ , with the subscript  $q = 1, 2, \dots, N$  denoting the image source. Each  $\mathbf{x}_q$  represents one element of the vector  $\mathbf{x}$ , i.e.  $\mathbf{x}_q \in \mathbf{x}$ . The vectorized image sources  $\mathbf{x}_q$  can be represented in terms

of a sparse basis of  $L \times 1$  vectors  $\{\boldsymbol{\Phi}_i\}_{i=1}^L$ . Using the  $L \times L$  basis matrix  $\boldsymbol{\Phi}$ , the columns of which are the vectors  $\{\boldsymbol{\Phi}_i\}_{i=1}^L$ , this is written as

$$\begin{aligned}\mathbf{x}_q &= \boldsymbol{\Phi} \mathbf{c}_q \\ \mathbf{c}_q &= \boldsymbol{\Phi}^T \mathbf{x}_q\end{aligned}\tag{97}$$

where the column vector  $\mathbf{c}_q$  contains the transform coefficients and  $\boldsymbol{\Phi}^T$  denotes the Hermitian matrix transpose of  $\boldsymbol{\Phi}$ . The vector  $\mathbf{y}$  that contains the measured Stokes parameters can also be transformed via

$$\begin{aligned}\mathbf{y}_q &= \boldsymbol{\Phi} \mathbf{d}_q \\ \mathbf{d}_q &= \boldsymbol{\Phi}^T \mathbf{y}_q.\end{aligned}\tag{98}$$

Here  $\mathbf{d}_q$  contains the transform coefficients of  $\mathbf{y}_q$ . By applying the sparsifying transform represented by  $\boldsymbol{\Phi}$  to both sides in Eq. (97), one obtains an underdetermined separation problem in the sparse representation domain:

$$\mathbf{d} = \mathbf{A} \mathbf{c}.\tag{99}$$

Strictly speaking, Eq. (99) is only true for a position independent mixing matrix, i.e.  $\mathbf{A}(i, j) = \mathbf{A}$ . The stated problem can be solved by finding the best estimate  $\hat{\mathbf{c}}$  to Eq. (99), followed by a transformation of  $\hat{\mathbf{c}}$  back into the image domain.

### *Image Reconstruction*

Assuming  $K$ -sparsity in the transform domain represented by  $\boldsymbol{\Phi}$ , i.e. only  $K \ll L$  of the transform coefficients are nonzero, it can be shown that the solution to the underdetermined

problem from Eq. (99) in the absence of noise can be expressed as a minimum  $\ell_1$  reconstruction algorithm according to

$$\hat{\mathbf{c}}_k = \arg \min \|\hat{\mathbf{c}}_k\|_1, \text{ subject to } \mathbf{d}_k = \mathbf{A}\mathbf{c}_k \quad (100)$$

for  $k=1, \dots, K$ . The  $\ell_p$ -norm  $\|\mathbf{v}\|_p$  of a  $D$ -dimensional vector  $\mathbf{v}$  is defined as  $\|\mathbf{v}\|_p \equiv \left( \sum_{i=1}^D |v_i|^p \right)^{1/p}$ .

The  $\ell_1$  reconstruction to the problem defined in Eq. (100) is a convex optimization that conveniently reduces to a linear program of complexity  $O(N^3)$  [118]. The solution can be justified either geometrically [161] or probabilistically as a maximum posterior probability (MAP) problem with Laplacian priors [162].

To handle noise, the  $\ell_1$  reconstruction problem in Eq. (100) can be replaced with an  $\ell_1 - \ell_2$  problem:

$$\hat{\mathbf{c}}_k = \arg \min \|\mathbf{c}_k\|_1, \text{ subject to } \|\mathbf{d}_k - \mathbf{A}\mathbf{c}_k\|_2 \leq \varepsilon \quad (101)$$

where  $\varepsilon$  accounts for the noise. As this problem is known to be NP-hard, approximation algorithms are often considered. An overview of image processing based on  $\ell_1 - \ell_2$  optimization can be found in [163]. In this work, the noise was neglected and therefore  $\ell_1$  reconstruction approach captured in Eq. (100) was employed. All results were obtained using the L1-MAGIC collection of MATLAB® routines for solving convex optimization problems [115].

## **APPENDIX F: OPTICALLY-CONTROLLED ACTIVE MEDIA**

### Realizing an Optically-Controlled Active Medium

The optically-controlled active medium is depicted in Figure 49. Light from a collimated laser beam is brought to a focus on the surface of a colloidal suspension of polystyrene microspheres with concentrations on the order of 1% by weight. The suspension is held in a well (3 mm in diameter and 5 mm deep) that was drilled into an aluminum block (the linear dimension of the block is about 10 cm), which serves as a heat sink and whose walls reflect the light back into the sample. A multi-mode fiber collects the light scattered by the spheres, which is detected by a photodetector and fed into a spectrum analyzer.

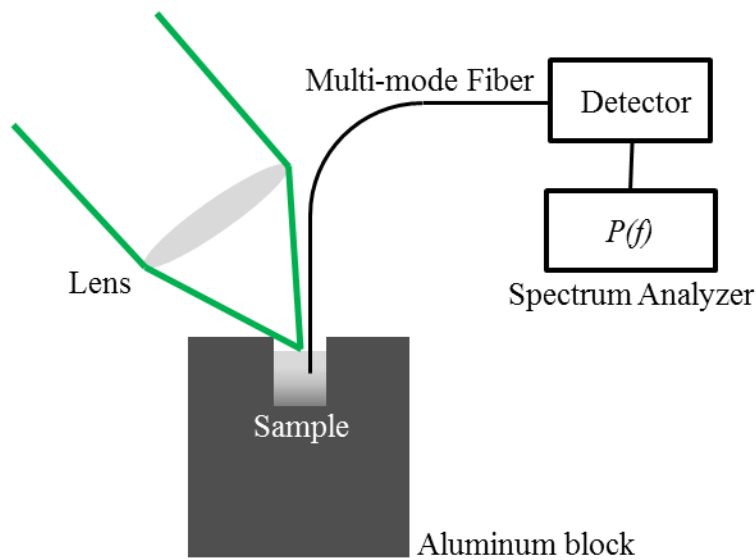


**Figure 49** The setup for an optically-controlled active medium. Collimated light from a 532 nm laser beam of variable power is focused by a lens into the suspension of polystyrene spheres in water. Typical concentrations of spheres are of the order of 1% by weight. The multiply scattered intensity fluctuations are picked up by a detector and their power spectrum is recorded.

If the suspension is sufficiently concentrated, then only multiply scattered light will enter the fiber. The randomization of the light is further increased by scattering off of the rough walls of the well. The intensity fluctuations of the scattered light measured by the fiber in this case will

be exponentially correlated, like in Eq. (22), but with a decay time possessing an additional factor of  $\bar{s}/\ell^*$ , where  $\bar{s}$  is the average path length a photon takes before entering the fiber [25]

$$g^{(2)}(\tau) \approx 1 + \beta \exp \left[ - \left( k^2 \langle \Delta R(\tau)^2 \rangle \bar{s} / \ell^* \right) \tau \right]. \quad (102)$$

Here, the wavenumber in the medium is  $k$ .

It is important to note that only one other effect, that of hydrodynamic coupling between the fluid and spheres, is capable of decreasing the slope beyond a value of -2; however, the characteristic frequency for hydrodynamic effects is  $f_h = \eta / r^2 \rho_f \approx 100 \text{ kHz}$ , a full order of magnitude beyond the onset of the first observation of the steep log-log slope [159].

The total force on the particle in the randomized field may be calculated using the Minkowski stress tensor. For dielectric microspheres, this approach results in an expression for the force that goes as [164]

$$\mathbf{F} = -\frac{1}{2} \varepsilon_0 \varepsilon \int_{\Omega} |\mathbf{f}|^2 \hat{\mathbf{r}} d\Omega + \frac{2\pi}{k} \varepsilon_0 \varepsilon \sum_{m=1}^M \hat{\mathbf{k}}_m \text{Im} [\mathbf{f} \cdot \mathbf{E}_m^*]. \quad (103)$$

The optical force on the microsphere is the sum of two components: the conservative force is given by the first term on the right hand side of Eq. (103) as an integral of the magnitude squared of the normalized scattering amplitude  $\mathbf{f}$  over a  $4\pi$  solid angle.  $\mathbf{f}$  is obtained by a Mie theory calculation [16]. The second component is the radiation pressure which is given by the sum over plane waves with directions  $\hat{\mathbf{k}}_m$  and incident fields  $\mathbf{E}_m^*$ .

The equation of motion for this particle—including the optical force from Eq. (103)—is

$$m \frac{d\mathbf{v}}{dt} = -m\gamma \mathbf{v} + \hat{\xi} + \hat{\mathbf{F}} \quad (104)$$



where  $\mathbf{v}$  is the particle's velocity,  $\gamma$  is the inertial relaxation rate (which depends on the fluid's viscosity), and  $\hat{\xi}$  is the zero mean random noise due to the collisions of the fluid molecules with the particle. Assuming that the noise in any direction is independent from any other direction, the autocorrelation function of this noise is given by the fluctuation-dissipation theorem as  $\langle \hat{\xi}(t') \hat{\xi}(t) \rangle = 2mk_B T \gamma \delta(t' - t)$ . Note that the units work out correctly when the delta function carries units of inverse seconds.

Solving Eq. (104) with the use of Eq. (103) and the time-dependent speckle field obtained in a mean field results in the velocity of the particle as a function time, from which its position and statistical moments of its displacement may be inferred.

### Diffusion of Particles in a 3D Speckle: Analytics

The Brownian motion of a particle may be characterized by the moments of the displacement. If the particles are spherical and the three dimensional speckle is fully-developed [152], there is no preferred direction to its motion and it suffices to study only one spatial dimension. The displacement is obtained from the equation of motion

$$m\dot{v} = -\gamma mv + \hat{\xi}(t) + \hat{F}(t) \quad (105)$$

with the quantities retaining the same meaning as in Eq. (104). In the overdamped regime, for times long compared to  $\gamma^{-1}$ , the left hand side of Eq. (105) may be set to zero:

$$0 = -\gamma mv + \hat{\xi}(t) + \hat{F}(t). \quad (106)$$

The thermal noise follows the fluctuation-dissipation theorem  $\langle \xi(t')\xi(t) \rangle = 2mk_B T \gamma \delta(t' - t)$  and is of zero mean.

Suppose now that the force  $\hat{F}(t)$  is zero mean and is described by a correlation function  $\Gamma(t - t')$

$$\begin{aligned}\langle \hat{F}(t) \rangle &= 0 \\ \langle \hat{F}(t)\hat{F}(t') \rangle &= F_0^2 \Gamma(t - t').\end{aligned}\tag{107}$$

Then, rewriting Eq. (106) in terms of the particle's position  $\dot{x} = v$  and integrating gives

$$x(t) = \frac{1}{m\gamma} \int_{t_0}^t [\hat{\xi}(t') + \hat{F}(t')] dt'. \tag{108}$$

The variance of the position  $\text{var}[x(t)] = \langle [x(t) - \langle x(t) \rangle]^2 \rangle$  may be calculated by setting

$x(0) = \langle x(t) \rangle = 0$ . Then, the variance becomes equivalent to the mean square displacement

$$\langle x^2(t) \rangle = \frac{1}{(m\gamma)^2} \int_{t_0}^t \int_{t_0}^t [\langle \hat{\xi}(t')\hat{\xi}(t'') \rangle + \langle \hat{F}(t')\hat{F}(t'') \rangle] dt' dt''. \tag{109}$$

Of course, Eq. (109) was derived assuming that  $\hat{\xi}(t)$  and  $\hat{F}(t)$  are uncorrelated. Finally, Eq. (109) may be simplified using the fluctuation-dissipation theorem for the Brownian noise and Eq. (107)

$$\langle x^2(t) \rangle = \frac{2k_B T}{m\gamma} t + \left( \frac{F_0}{m\gamma} \right)^2 \int_{t_0}^t \int_{t_0}^t \Gamma(t' - t'') dt' dt''. \tag{110}$$

Eq. (110) gives the mean squared displacement of the particle as a function of time and the ACF of the random optical force  $\hat{F}(t)$ . If the ACF of  $\hat{F}(t)$  is Gaussian with characteristic time  $\tau_F$ , the limiting forms of the MSD are

$$\begin{aligned}\langle x^2 \rangle &= \frac{2k_B T}{m\gamma} t + \left( \frac{F_0}{m\gamma} \right)^2 t^2, \quad t \ll \tau_F \\ \langle x^2 \rangle &= \frac{2k_B T}{m\gamma} t + \sqrt{2\pi} \left( \frac{F_0}{m\gamma} \right)^2 \tau_F t, \quad t \ll \tau_F\end{aligned}\quad (111)$$

For times well before  $\tau_F$ , the MSD grows quadratically with time, i.e. it is superdiffusive. For times much longer than  $\tau_F$ , the MSD grows linearly, but with a diffusion coefficient that's larger by an additive term of  $\sqrt{2\pi} (F_0/m\gamma)^2 \tau_F$ . This is because the Gaussian assumption for the ACF is not heavy-tailed. If it followed a power law, then the particle may remain superdiffusive for all time [130].

The transition region between the short and long time behaviors of the MSD may be better quantified by higher order moments of the displacement [85,165]. The moments, denoted as  $q$ , go as

$$\left\langle \left| r(t+\tau) - r(t) \right|^q \right\rangle \sim t^{\lambda(q)} \quad (112)$$

where the exponent  $\lambda(q)$  is a function of the moment. For regular Brownian motion,  $\lambda(q) = q/2$  and for ballistic motion  $\lambda(q) = q$ . A nonlinear dependence on  $q$  is indicative of several other types of transport phenomena, including Levy flights [166].

## Diffusion of Particles in a 3D Speckle: Numerics

### *Brownian Motion*

Euler's method may be used to obtain a numeric formula for the Langevin equation, Eq. (105) [167,168]:

$$v(t + \Delta t) - v(t) = -\gamma v(t) \Delta t + F(t) \Delta t / m + \sqrt{6Dt} X(t). \quad (113)$$

The length of each time step is  $\Delta t$  and the coefficient  $X$  is a normally distributed random variable. Note also that Eq. (113) is one dimensional but suffices for the stated purposes since each dimension is independent of the others.

To simulate Eq. (113), time is first discretized into  $N = 2^n$  steps of length  $\Delta t$ , where  $n$  is a positive integer.  $\Delta t$  is chosen such that it is much smaller than the inertial relaxation time of the particle, or  $\Delta t \ll \gamma^{-1}$ , to avoid numerical errors. Assuming that the particle is effectively a sphere, the drag coefficient is determined by

$$\begin{aligned} \gamma &= \frac{\zeta}{m} \\ \zeta &= 6\pi\eta r \end{aligned} \quad (114)$$

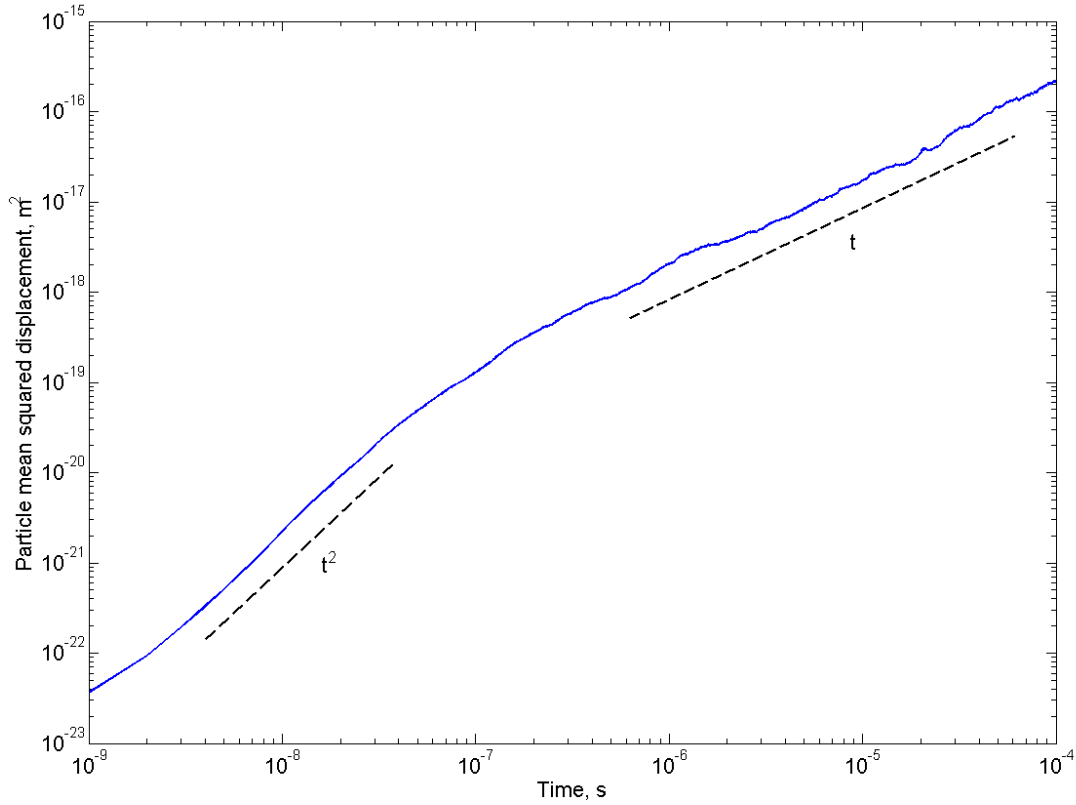
with  $\eta$  the fluid's viscosity and  $r$  the particle's hydrodynamic radius. The velocity of the particle is determined at each time step after the calculation of the optical force,  $\mathbf{F}$ . Its position may be determined at each step by multiplying the velocity by  $\Delta t$ .

Figure 50 is a plot of the averaged mean squared displacement (MSD) for 200 particles obtained from the velocity data with  $F$  set to zero. The particle is assumed spherical with a radius of  $0.25 \mu\text{m}$  and a density of  $1.05 \text{ g/cm}^3$ . The temperature of the simulation was set at  $300 \text{ K}$ . For

this particle, the inertial relaxation time as calculated from Eq. (114) is  $\gamma^{-1} \approx 20 \text{ ns}$ . This time marks the transition from ballistic to diffusive motion, the latter of the two scaling linearly with time according to the well-known expression

$$\langle \Delta R^2(t) \rangle = 2dDt \quad (115)$$

with  $d$  representing the number of dimensions and  $D$  the diffusion coefficient.



**Figure 50** The mean squared displacement (MSD) of a particle undergoing Brownian motion vs. time. The plot was generated using the above algorithm and the results were averaged over 200 individual particle trajectories. Other simulation parameters include the particle's hydrodynamic radius ( $0.25 \mu\text{m}$ ), the particle density ( $1.05 \text{ g/cm}^3$ ), and the temperature ( $300 \text{ K}$ ). Note the transition from ballistic to diffusive motion around the relaxation time,  $\gamma^{-1} \approx 20 \text{ ns}$ .

### Generating a Spatiotemporal Volume Speckle Field

In some circumstances the field responsible for the optical force  $\mathbf{F}$  may be left as independent of the particle's position and allowed to vary according to some pre-defined statistical measure. One such example is a single particle in a highly multiply-scattering medium. The steps involved for modeling this situation would go as follows:

1. calculate a realization of the field (with pre-determined speckle sizes and time correlation functions);
2. determine the force on the particle and move it accordingly;
3. update the field by one time step;
4. repeat steps 2 and 3 while tracking the particle's locations.

While particle diffusion in a three-dimensional, space-dependent random potential has been studied with some detail [54,55,57], there have been no works to the author's knowledge that concern an additional time-dependence of the optical potential. The following simulations are therefore the first such study of this phenomenon.

### *Generating a Space- and Time-Dependent Volume Speckle Field*

A fully-developed volume speckle field is simulated as a superposition of plane waves with directions that are uniformly sampled from the unit sphere and phases for the polarization components that are uniformly sampled from the range  $[0, 2\pi)$ .  $N$  vectors that uniformly sample the unit sphere are generated by creating  $N$  3-vectors whose elements are normally distributed. Each vector is then normalized to its magnitude.

Next, the polarization of each plane wave is generated. With reference to Figure 51, the electric field vector is placed normal to the k-vector of a particular plane wave with a random orientation in the x'-y' plane. The k-vector and the field vector are transformed to the lab frame (x-y-z coordinate axes) with the transformation matrix

$$\mathbf{R} \equiv \begin{pmatrix} \cos(\phi) & \sin(\phi) & 0 \\ -\sin(\phi) & \cos(\phi) & 0 \\ 0 & 0 & 1 \end{pmatrix} \begin{pmatrix} \cos(\theta) & 0 & -\sin(\theta) \\ 0 & 1 & 0 \\ \sin(\theta) & 0 & \cos(\theta) \end{pmatrix} \quad (116)$$

where  $\phi$  and  $\theta$  are the azimuth and zenith angles, respectively, of the k-vector in the lab frame.

The total field is a sum over all the  $N$  randomly generated plane waves and is expressed as

$$\mathbf{E}(\mathbf{r}, t) = \mathbf{R} \sum_{j=1}^N \begin{pmatrix} E_{x,j} e^{i\hat{\phi}_{x,j}(t)} \\ E_{y,j} e^{i\hat{\phi}_{y,j}(t)} \\ 0 \end{pmatrix} e^{i\mathbf{k}_j \cdot \mathbf{r}}. \quad (117)$$

In this expression,  $E_{x,j}^2 + E_{y,j}^2$  is a constant for all plane waves and the phases  $\hat{\phi}_{x,j}(t)$  and  $\hat{\phi}_{y,j}(t)$  are independent, zero-mean Gaussian random variables with a standard deviation of  $\pi$  and a Gaussian autocorrelation function. The matrix  $\mathbf{R}$  rotates each plane wave into the lab frame's coordinate system, which effectively randomizes the polarization of the field.

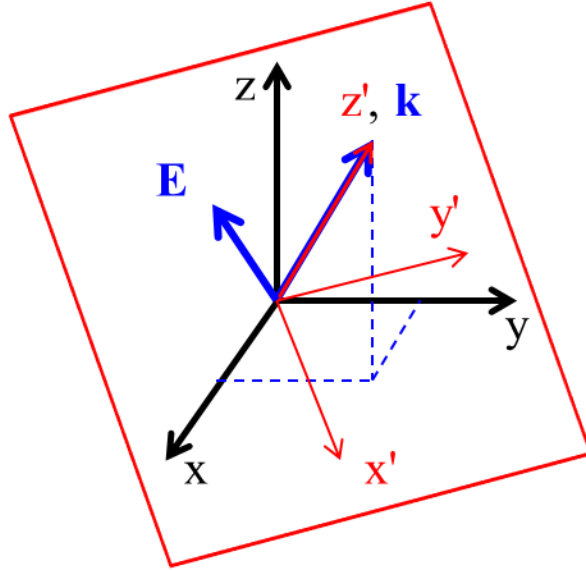


**Figure 51** Lab frame (x-y-z coordinate axes) and the frame of a single plane wave (x'-y'-z' axes) whose k-vector lies along the z' axis. The red outlined plane is normal to the z' axis and contains the electric field vector **E**

The field and intensity generated in such a manner must satisfy some conditions to be valid. For fully-developed, unpolarized speckle in one dimension, the histogram of intensities follows a negative exponential distribution

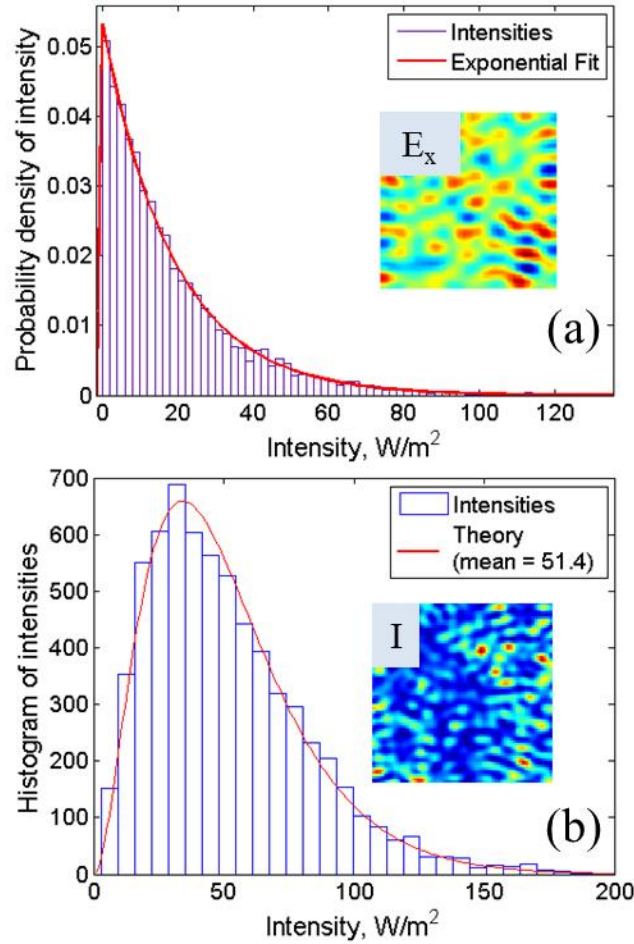
$$p(I) = \frac{1}{\bar{I}} \exp\left(-\frac{I}{\bar{I}}\right) \quad (118)$$

with  $\bar{I}$  representing the average intensity [152]. In three dimensions, fully-developed and polarized speckle may be understood as the incoherent superposition of three volume speckle fields of equal average intensity. The distribution of intensities  $I_s$  for this case follows the form [152]

$$p(I_s) = 13.5 \frac{I_s^2}{\bar{I}^3} \exp\left(-\frac{3I_s}{\bar{I}}\right). \quad (119)$$

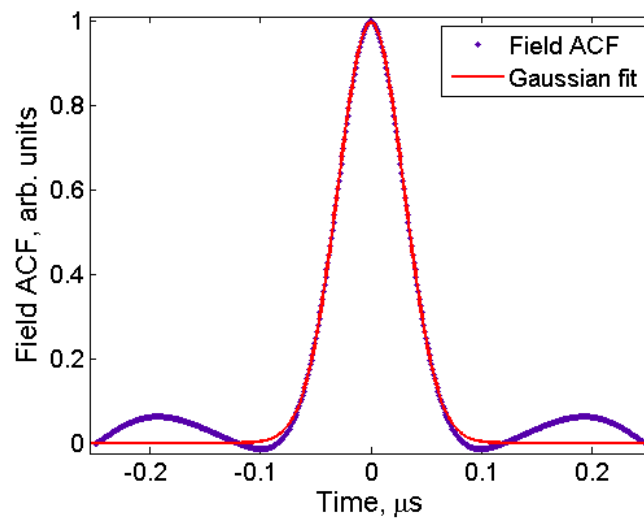


Figure 52 displays the simulated intensity distributions for 50 randomly superposed plane waves that were generated through the above algorithm. The insets are a) the real part of the x-component of the field and b) the total intensities on the x-y plane. The intensities were recorded on a rectangular grid with unit cells spaced by 50 nm and extending 4  $\mu\text{m}$  in each direction. The wavelength was 532 nm. The good agreement with the theory is an indication that the generated fields follow the correct spatial statistics for fully-developed speckle.



**Figure 52** a) Probability distribution function for the intensity of the x-polarized component of the simulated speckle field in the x-y plane. Inset: the real part of x-component of the field. b) Histogram of intensities which take all electric field directions into account. Inset: The intensity distribution within the x-y plane. Solid lines represent a fit to Eq. (118) and a plot of Eq. (119), respectively. The value for the mean intensity in (b) is the mean of the data.

The field must also satisfy a predetermined temporal autocorrelation function. From the same simulation just described, the temporal autocorrelation of the x-component of the electric field—derived from the superposition of all the plane waves—for every point in the simulated plane was calculated and then averaged over all the points. The simulation ran from 1 nanosecond to 10 microseconds at 1 nanosecond time steps. All other parameter values previously mentioned were retained for this test. The phase of each polarization component was sampled from a signal exhibiting a Gaussian autocorrelation function with a characteristic time of 0.1 microseconds. These components were rotated into the lab frame and summed over all plane waves to find the total electric field. Figure 53 displays the ACF for the x-component of the total field. A fit of the ACF to a Gaussian function produced a characteristic time of approximately 0.03 microseconds. Importantly, the shape of the field ACF is the same as the ACF of each phase component.



**Figure 53** The temporal autocorrelation of the x-component calculated from the simulation. The phases of the 50 plane waves comprising the field varied randomly in time according to a Gaussian-shaped ACF with a characteristic time of 0.1  $\mu\text{s}$ . The fit has a characteristic time of 0.03  $\mu\text{s}$ .

The plane waves from this process are used to find the force on each particle in the simulation according to Eq. (103). After each time step, the particle is translated in this field, the field is updated by changing the phase according to the pre-generated random signal, and the new force is calculated.

## **APPENDIX G: DERIVATION OF THE DIPOLE INTERACTION FORCE**

After substituting Eq. (35) into Eq. (36) to obtain the force on the second dipole, three different types of correlation functions related to the incident field must be evaluated:  $\langle |E_u(\mathbf{r})|^2 \rangle_\gamma$ ,  $\langle E_u^*(\mathbf{r}) E_u(\mathbf{r}_2) \rangle_\gamma$ , and  $\langle E_u(\mathbf{r}_1) \partial E_u^*(\mathbf{r}_2) / \partial x \rangle_\gamma$ , where  $u = x, y, z$ . The first type is just the average intensity of the incident Gaussian field, or  $\frac{1}{3} \langle I \rangle$ , the factor of a third being present because it is a correlation of only one field component along three orthogonal directions. The second type is closely related to the degree of spatial coherence of the field, since it is a two-point field correlation. In rewriting this correlation function as an analytical expression, the techniques in Ref.'s [169,170] were used to split it into two expressions, one for the correlation function parallel to the line joining the dipoles and one perpendicular to it:

$$\begin{aligned} \mu_{parallel}(\xi) &= 3 \frac{\sin \xi - \xi \cos \xi}{\xi^3} \\ \mu_{perpendicular}(\xi) &= \frac{3}{2} \left( \frac{\sin \xi}{\xi} - \frac{\sin \xi - \xi \cos \xi}{\xi^3} \right) \end{aligned} \quad (120)$$

The remaining correlation function looks like  $\langle E_u(\mathbf{r}_1) \partial E_u^*(\mathbf{r}_2) / \partial x \rangle_\gamma$  and is the correlation of the field at one point with its derivative at another point along the x-axis. Using the same approach as in Ref. [169], the correlation function is rewritten as

$$v_{u(x)}(R) = \frac{-i}{\langle E^2 \rangle} \left\langle \left( E_u \cdot E_u^* \right) \frac{k_x}{k} \exp(i\mathbf{k}\mathbf{r}) \right\rangle \quad (121)$$

with

$$\begin{aligned}
v_{x(x)} &= -3 \frac{\left[ 3kR \cos(kR) + \left( (kR)^2 - 3 \right) \sin(kR) \right]}{(kR)^4} \\
v_{y(x)} = v_{z(x)} &= -3 \frac{kR \left[ (kR)^2 - 3 \right] \cos(kR) + \left[ 3 - 2(kR)^2 \right] \sin(kR)}{2(kR)^4}.
\end{aligned} \tag{122}$$

Finally, combining all three analytical expressions for the correlation functions results in the ensemble averaged force between the dipoles:

$$\begin{aligned}
\langle F_x(R) \rangle &= \frac{1}{6} \langle I \rangle \left\{ -k \operatorname{Re} \left( \frac{G_x^* \alpha^{*2}}{1 - (G_x^* \alpha^*)^2} \right) v_{x(x)}(R) \right. \\
&\quad + |\alpha|^2 \operatorname{Re} \left( \frac{\partial G_x}{\partial R} \right) \frac{\left[ \mu_x(R) (1 + |G_x \alpha|^2) + 2 \operatorname{Re}(G_x \alpha) \right]}{|1 - G_x^2 \alpha^2|^2} \\
&\quad - 2k \operatorname{Re} \left( \frac{G_y^* \alpha^{*2}}{1 - (G_y^* \alpha^*)^2} \right) v_{y(x)}(R) \\
&\quad \left. + |\alpha^2| \operatorname{Re} \left( \frac{\partial G_y}{\partial R} \right) \frac{2 \left[ \mu_y(R) (1 + |G_y \alpha|^2) + 2 \operatorname{Re}(G_y \alpha) \right]}{|1 - G_y^2 \alpha^2|^2} \right\}.
\end{aligned} \tag{123}$$

In this equation,  $G_x = 2 \exp(ikR)(ikR - 1)/R^3$  and  $G_y = G_z = \exp(ikR)(k^2 R^2 + ikR + 1)/R^3$  are the two eigenvalues of the Greens function for this geometry. Importantly, this force *is not* zero. That is, there is a force between dipolar particles that does not average out.

Eq. **Error! Reference source not found.** can be simplified for dielectric and nonabsorbing particles such that  $|G_x \alpha| \ll 1$ ,  $|G_y \alpha| \ll 1$ , and  $\operatorname{Im} \alpha \ll \operatorname{Re} \alpha$ . In this case, the force is

$$\begin{aligned}
\langle F_x(R) \rangle &\approx \frac{1}{6} \langle I \rangle \alpha^2 k^4 f(kR) \\
f(\xi) &= \frac{3 \left[ \xi (18 - 8\xi^2 + \xi^4) \cos(2\xi) + (-9 + 16\xi^2 - 3\xi^4) \sin(2\xi) \right]}{\xi^7}.
\end{aligned} \tag{124}$$

## LIST OF PUBLICATIONS

1. Sergey Sukhov, **K. M. Douglass**, and A. Dogariu, “Dipole-dipole interaction in random electromagnetic fields,” *Opt. Lett.*, 38, 2385 (2013).
2. **K. M. Douglass**, Sergey Sukhov, and A. Dogariu, “Superdiffusion in optically-controlled active media,” *Nature Photon.* 6, 834 (2012).
3. **K. M. Douglass**, N. A. Sparrow, M. Bott, C. Fernandez-Valle, and A. Dogariu, “Measuring anisotropic cell motility on curved substrates,” *J. Biophoton.* 6, 387 (2013).
4. **K. M. Douglass**, S. John, T. Suezaki, G. A. Ozin, and A. Dogariu, "Anomalous flow of light near a photonic crystal pseudogap," *Optics Express* 19, 25320–25327 (2011).
5. **K. M. Douglass**, J. Ellis, C. Toma, A. Mahalanobis, and A. Dogariu, "Expanding the field of view by polarization multiplexing," *Applied Optics* **49**, H40–H46 (2010).
6. **K. M. Douglass** and A. Dogariu, "Measuring diffusion coefficients independently of boundary conditions," *Opt. Lett.* **34**, 3379–3381 (2009).
7. J. Broky, **K. M. Douglass**, J. Ellis, and A. Dogariu, “Fluctuations of scattered waves: going beyond the ensemble average,” *Optics Express* **17**, 10466-10471 (2009).



## LIST OF PRESENTATIONS

1. **K. M. Douglass**, S. Sukhov, and A. Dogariu, “Forces in Random Electromagnetic Fields,” in CLEO: 2013, OSA Technical Digest (online) (Optical Society of America, 2013), paper QTh4A.3.
2. **K. M. Douglass**, S. Sukhov, and A. Dogariu, “Optically-Controlled Active Media: Superdiffusion in Random Fields,” in Frontiers in Optics (FiO)/Laser Science (LS) (Optical Society of America, Washington, DC, 2012) paper FTh3D7.
3. **K. M. Douglass**, A. Fears, L. Denney, and A. Dogariu, “Passive Optical Measurements of Local Viscoelastic Properties of Pluronics Systems,” in Biological and Pharmaceutical Complex Fluids, (Engineering Conferences International, New York, NY, 2012).
4. **K. M. Douglass**, L. Denney, C. Toma, and A. Dogariu, “Real-time optical monitoring of blood viscoelasticity,” in Biological and Pharmaceutical Complex Fluids,” (Engineering Conferences International, New York, NY, 2012).
5. K. Kasunic, M. Bagnell, J. D'Archangel, A. W. Dillard, **K. M. Douglass**, M. S. Mills, D. Ott, V. Relina, B. Webb, “Research-centric project-based learning of optomechanical design,” in Optics and Photonics, (SPIE, Bellingham, WA, 2012), paper 8481-10.
6. **K. M. Douglass**, N. A. Sparrow, M. Bott, C. Fernandez-Valle, and A. Dogariu, “Measuring anisotropic cell motility on curved substrates,” in Frontiers in Optics (FiO)/Laser Science (LS) (Optical Society of America, Washington, DC, 2011), poster JTua23.
7. **K. M. Douglass**, T. Suezaki, G. A. Ozin, S. John, and A. Dogariu, “Reflection of Subdiffusive Light from 3-D Disordered Photonic Crystals,” in Quantum Electronics and

- Laser Science Conference, OSA Technical Digest (CD) (Optical Society of America, 2010), paper QME3.
8. **K. M. Douglass**, G. Biener, S. Sukhov, and A. Dogariu, “Rotational Stochastic Resonance,” in Quantum Electronics and Laser Science Conference, OSA Technical Digest (CD), (Optical Society of America, 2010), paper QMC5.
  9. **K. M. Douglass**, T. Kohlgraf-Owens, J. Ellis, C. Toma, A. Mahalanobis, and A. Dogariu, “Expanded Field of View Using Polarization Multiplexing,” in Computational Optical Sensing and Imaging, OSA Technical Digest (CD) (Optical Society of America, 2009), paper CWA5.
  10. J. Broky, J. Ellis, **K. Douglass**, and A. Dogariu, “Statistical Fluctuations: Going Beyond the Ensemble Average,” in Frontiers in Optics, OSA Technical Digest (CD) (Optical Society of America, 2008), paper FWV5.

## LIST OF REFERENCES

1. A. Ishimaru, *Wave Propagation and Scattering in Random Media* (John Wiley & Sons, 1999).
2. P. Sheng, *Introduction to Wave Scattering, Localization and Mesoscopic Phenomena* (Springer, 2006).
3. P. W. Anderson, "More Is Different," *Science* **177**, 393–396 (1972).
4. S. Bader, "Emergent Physics at the Mesoscale," *APS News* **21**, 8 (2012).
5. D. H. Boal, *Mechanics of the Cell* (Cambridge University Press, 2002).
6. K. Kaneko, *Life: An Introduction to Complex Systems Biology*, 1st ed. (Springer, 2006).
7. P. Hänggi and F. Marchesoni, "Artificial Brownian motors: Controlling transport on the nanoscale," *Rev. Mod. Phys.* **81**, 387–442 (2009).
8. T. A. Witten, "Insights from soft condensed matter," *Rev. Mod. Phys.* **71**, S367–S373 (1999).
9. S. John, "Strong localization of photons in certain disordered dielectric superlattices," *Phys. Rev. Lett.* **58**, 2486–2489 (1987).
10. "Quasicrystals—The Silver Jubilee," *Philosophical Magazine* **88**, 1879–1882 (2008).
11. N. Engheta and R. W. Ziolkowski, *Metamaterials: Physics and Engineering Explorations* (John Wiley & Sons, 2006).
12. L. P. Faucheux, L. S. Bourdieu, P. D. Kaplan, and A. J. Libchaber, "Optical Thermal Ratchet," *Phys. Rev. Lett.* **74**, 1504–1507 (1995).
13. D. G. Grier, "A revolution in optical manipulation," *Nature* **424**, 810–816 (2003).

14. A. Apostol, D. Haefner, and A. Dogariu, "Near-field characterization of effective optical interfaces," *Phys. Rev. E* **74**, 066603 (2006).
15. D. Haefner, S. Sukhov, and A. Dogariu, "Scale-dependent anisotropic polarizability in mesoscopic structures," *Phys. Rev. E* **81**, 016609 (2010).
16. C. F. Bohren and D. R. Huffman, *Absorption and Scattering of Light by Small Particles* (Wiley-VCH, 1998).
17. A. Dogariu, J. Uozumi, and T. Asakura, "Enhancement Factor in the Light Backscattered by Fractal Aggregated Media," *Optical Review* **3**, 71–82 (1996).
18. B. J. Berne and R. Pecora, *Dynamic Light Scattering*, Dover Ed (Dover Publications Inc., 2003).
19. D. Huang, E. A. Swanson, C. P. Lin, J. S. Schuman, W. G. Stinson, W. Chang, M. R. Hee, T. Flotte, K. Gregory, C. A. Puliafito, and A. Et, "Optical Coherence Tomography," *Science* **254**, 1178–1181 (1991).
20. M. Minsky, "Microscopy apparatus," U.S. patent 3013467 (December 19, 1961).
21. E. Baleine and A. Dogariu, "Variable Coherence Scattering Microscopy," *Phys. Rev. Lett.* **95**, 193904 (2005).
22. E. Betzig, G. H. Patterson, R. Sougrat, O. W. Lindwasser, S. Olenych, J. S. Bonifacino, M. W. Davidson, J. Lippincott-Schwartz, and H. F. Hess, "Imaging Intracellular Fluorescent Proteins at Nanometer Resolution," *Science* **313**, 1642–1645 (2006).
23. M. J. Rust, M. Bates, and X. Zhuang, "Sub-diffraction-limit imaging by stochastic optical reconstruction microscopy (STORM)," *Nature Methods* **3**, 793–796 (2006).

24. G. Maret and P. E. Wolf, "Multiple light scattering from disordered media. The effect of brownian motion of scatterers," *Zeitschrift für Physik B Condensed Matter* **65**, 409–413 (1987).
25. D. J. Pine, D. A. Weitz, P. M. Chaikin, and E. Herbolzheimer, "Diffusing wave spectroscopy," *Phys. Rev. Lett.* **60**, 1134–1137 (1988).
26. T. G. Mason and D. A. Weitz, "Optical Measurements of Frequency-Dependent Linear Viscoelastic Moduli of Complex Fluids," *Phys. Rev. Lett.* **74**, 1250–1253 (1995).
27. R. Cerbino and V. Trappe, "Differential Dynamic Microscopy: Probing Wave Vector Dependent Dynamics with a Microscope," *Phys. Rev. Lett.* **100**, 188102 (2008).
28. T. J. Kippenberg and K. J. Vahala, "Cavity Optomechanics: Back-Action at the Mesoscale," *Science* **321**, 1172–1176 (2008).
29. M. C. W. van Rossum and T. M. Nieuwenhuizen, "Multiple scattering of classical waves: microscopy, mesoscopy, and diffusion," *Rev. Mod. Phys.* **71**, 313–371 (1999).
30. A. Mogilner and G. Oster, "Cell motility driven by actin polymerization," *Biophysical Journal* **71**, 3030–3045 (1996).
31. D. Selmeczi, S. Mosler, P. H. Hagedorn, N. B. Larsen, and H. Flyvbjerg, "Cell Motility as Persistent Random Motion: Theories from Experiments," *Biophysical Journal* **89**, 912–931 (2005).
32. R. Loudon, *The Quantum Theory of Light*, 2nd ed. (Oxford University Press, USA, 1983).
33. K.-C. Kwan, X. Zhang, Z.-Q. Zhang, and C. T. Chan, "Effects due to disorder on photonic crystal-based waveguides," *Applied Physics Letters* **82**, 4414 –4416 (2003).

34. C. L[[oacute]]pez, "Anderson localization of light: A little disorder is just right," *Nature Physics* **4**, 755–756 (2008).
35. J. D. Jackson, *Classical Electrodynamics Third Edition*, 3rd ed. (Wiley, 1998).
36. P. N. Prasad, *Introduction to Biophotonics*, 1st ed. (Wiley-Interscience, 2003).
37. A. Ashkin, "Acceleration and Trapping of Particles by Radiation Pressure," *Phys. Rev. Lett.* **24**, 156–159 (1970).
38. K. C. Neuman and S. M. Block, "Optical trapping," *Rev Sci Instrum* **75**, 2787–2809 (2004).
39. A. Ashkin, J. M. Dziedzic, J. E. Bjorkholm, and S. Chu, "Observation of a single-beam gradient force optical trap for dielectric particles," *Opt. Lett.* **11**, 288–290 (1986).
40. J. Durnin, J. J. Miceli, and J. H. Eberly, "Diffraction-free beams," *Phys. Rev. Lett.* **58**, 1499–1501 (1987).
41. G. A. Siviloglou, J. Broky, A. Dogariu, and D. N. Christodoulides, "Observation of Accelerating Airy Beams," *Phys. Rev. Lett.* **99**, 213901 (2007).
42. K. Dholakia, P. Reece, and M. Gu, "Optical micromanipulation," *Chemical Society Reviews* **37**, 42 (2008).
43. N. B. Simpson, K. Dholakia, L. Allen, and M. J. Padgett, "Mechanical equivalence of spin and orbital angular momentum of light: an optical spanner," *Opt. Lett.* **22**, 52–54 (1997).
44. R. Bowman, "iTweezers," <http://itunes.apple.com/us/app/itweezers/id456952257?mt=8>.
45. M. M. Burns, J.-M. Fournier, and J. A. Golovchenko, "Optical binding," *Phys. Rev. Lett.* **63**, 1233–1236 (1989).

46. Y. Roichman, D. G. Grier, and G. Zaslavsky, "Anomalous collective dynamics in optically driven colloidal rings," *Phys. Rev. E* **75**, 020401 (2007).
47. L. Bruno, V. Levi, M. Brunstein, and M. A. Despósito, "Transition to superdiffusive behavior in intracellular actin-based transport mediated by molecular motors," *Phys. Rev. E* **80**, 011912 (2009).
48. R. Kubo, "The fluctuation-dissipation theorem," *Reports on Progress in Physics* **29**, 255–284 (1966).
49. L. F. Cugliandolo, "The effective temperature," *Journal of Physics A: Mathematical and Theoretical* **44**, 483001 (2011).
50. J. Schwarz-Linek, C. Valeriani, A. Cacciuto, M. E. Cates, D. Marenduzzo, A. N. Morozov, and W. C. K. Poon, "Phase Separation and Rotor Self-Assembly in Active Particle Suspensions," *PNAS* **109**, 4052–4057 (2012).
51. L. Angelani, C. Maggi, M. L. Bernardini, A. Rizzo, and R. Di Leonardo, "Effective Interactions between Colloidal Particles Suspended in a Bath of Swimming Cells," *Phys. Rev. Lett.* **107**, 138302 (2011).
52. H.-R. Jiang, N. Yoshinaga, and M. Sano, "Active Motion of a Janus Particle by Self-Thermophoresis in a Defocused Laser Beam," *Phys. Rev. Lett.* **105**, 268302 (2010).
53. V. Démery and D. S. Dean, "Perturbative path-integral study of active- and passive-tracer diffusion in fluctuating fields," *Phys. Rev. E* **84**, 011148 (2011).
54. R. D. L. Hanes, C. Dalle-Ferrier, M. Schmiedeberg, M. C. Jenkins, and S. U. Egelhaaf, "Colloids in one dimensional random energy landscapes," *Soft Matter* **8**, 2714–2723 (2012).

55. A. H. Romero and J. M. Sancho, "Brownian motion in short range random potentials," *Phys. Rev. E* **58**, 2833–2837 (1998).
56. N. Pottier, "Aging properties of an anomalously diffusing particule," *Physica A: Statistical Mechanics and its Applications* **317**, 371–382 (2003).
57. F. Jendrzejewski, A. Bernard, K. Müller, P. Cheinet, V. Josse, M. Piraud, L. Pezzé, L. Sanchez-Palencia, A. Aspect, and P. Bouyer, "Three-dimensional localization of ultracold atoms in an optical disordered potential," *Nature Physics* **8**, 398–403 (2012).
58. E. J. Chaisson, *Cosmic Evolution: The Rise of Complexity in Nature* (Harvard University Press, 2002).
59. B. B. Mandelbrot, *The Fractal Geometry of Nature*, First Edition (W. H. Freeman and Company, 1982).
60. G. Popescu and A. Dogariu, "Optical path-length spectroscopy of wave propagation in random media," *Opt. Lett.* **24**, 442–444 (1999).
61. W. J. Brown, J. W. Pyhtila, N. G. Terry, K. J. Chalut, T. A. D'Amico, T. A. Sporn, J. V. Obando, and A. V. Wax, "Review and Recent Development of Angle-Resolved Low-Coherence Interferometry for Detection of Precancerous Cells in Human Esophageal Epithelium," *IEEE Journal of Selected Topics in Quantum Electronics* **14**, 88–97 (2008).
62. D. A. Boas, K. K. Bizheva, and A. M. Siegel, "Using dynamic low-coherence interferometry to image Brownian motion within highly scattering media," *Opt. Lett.* **23**, 319–321 (1998).
63. S. G. Johnson, J. D. Joannopoulos, and M. Soljačić, "MIT Photonic Bands: Manual," (2003).



64. E. Wolf, *Introduction to the Theory of Coherence and Polarization of Light*, 1st ed. (Cambridge University Press, 2007).
65. M. Born and E. Wolf, *Principles of Optics: Electromagnetic Theory of Propagation, Interference and Diffraction of Light* (Cambridge University Press, 1999).
66. B. J. Tromberg, N. Shah, R. Lanning, A. Cerussi, J. Espinoza, T. Pham, L. Svaasand, and J. Butler, "Non-Invasive In Vivo Characterization of Breast Tumors Using Photon Migration Spectroscopy," *Neoplasia* (New York, N.Y.) **2**, 26 (2000).
67. M. S. Patterson, B. Chance, and B. C. Wilson, "Time resolved reflectance and transmittance for the non-invasive measurement of tissue optical properties," *Appl. Opt.* **28**, 2331–2336 (1989).
68. R. Aronson, "Boundary conditions for diffusion of light," *J. Opt. Soc. Am. A* **12**, 2532–2539 (1995).
69. R. C. Haskell, L. O. Svaasand, T. Tsay, T. Feng, M. S. McAdams, and B. J. Tromberg, "Boundary conditions for the diffusion equation in radiative transfer," *JOSA A* **11**, 2727–2741 (1994).
70. G. Popescu, C. Mujat, and A. Dogariu, "Evidence of scattering anisotropy effects on boundary conditions of the diffusion equation," *Phys. Rev. E* **61**, 4523–4529 (2000).
71. J. X. Zhu, D. J. Pine, and D. A. Weitz, "Internal reflection of diffusive light in random media," *Phys. Rev. A* **44**, 3948–3959 (1991).
72. K. M. Douglass and A. Dogariu, "Measuring diffusion coefficients independently of boundary conditions," *Opt. Lett.* **34**, 3379–3381 (2009).

73. F. Liu, K. M. Yoo, and R. R. Alfano, "Should the photon flux or the photon density be used to describe the temporal profiles of scattered ultrashort laser pulses in random media?," *Opt. Lett.* **18**, 432–434 (1993).
74. N. Ducros, A. da Silva, J.-M. Dinten, and F. Peyrin, "Approximations of the measurable quantity in diffuse optical problems: theoretical analysis of model deviations," *J. Opt. Soc. Am. A* **25**, 1174–1180 (2008).
75. T. Svensson, R. Savo, E. Alerstam, K. Vynck, M. Burreli, and D. S. Wiersma, "Exploiting breakdown of the similarity relation for diffuse light transport: simultaneous retrieval of scattering anisotropy and diffusion constant," *arXiv:1211.6690* (2012).
76. R. Pecora, *Dynamic Light Scattering: Applications of Photon Correlation Spectroscopy* (Springer, 1985).
77. G. Popescu and A. Dogariu, "Dynamic light scattering in localized coherence volumes," *Opt. Lett.* **26**, 551–553 (2001).
78. P.-A. Lemieux and D. J. Durian, "Investigating non-Gaussian scattering processes by using nth-order intensity correlation functions," *J. Opt. Soc. Am. A* **16**, 1651–1664 (1999).
79. J. G. H. Joosten, "Dynamic light scattering by non-ergodic media," in *Application of Scattering Methods to the Dynamics of Polymer Systems*, B. Ewen, E. W. Fischer, and G. Fytas, eds., *Progress in Colloid & Polymer Science* No. 91 (Steinkopff, 1993), pp. 149–152.
80. F. Scheffold, S. E. Skipetrov, S. Romer, and P. Schurtenberger, "Diffusing-wave spectroscopy of nonergodic media," *Phys. Rev. E* **63**, 061404 (2001).

81. S. W. Provencher, "CONTIN: A general purpose constrained regularization program for inverting noisy linear algebraic and integral equations," *Computer Physics Communications* **27**, 229–242 (1982).
82. G. C. Fletcher and J. I. Harnett, "Photon Correlation Spectroscopy Using Optical Heterodyne Detection," *Aust. J. Phys.* **34**, 575–584 (1981).
83. J. C. Crocker, "Measurement of the hydrodynamic corrections to the Brownian motion of two colloidal spheres," *The Journal of Chemical Physics* **106**, 2837–2840 (1997).
84. T. Franosch, M. Grimm, M. Belushkin, F. M. Mor, G. Foffi, L. Forró, and S. Jeney, "Resonances arising from hydrodynamic memory in Brownian motion," *Nature* **478**, 85–88 (2011).
85. R. Ferrari, A. J. Manfroi, and W. R. Young, "Strongly and weakly self-similar diffusion," *Physica D: Nonlinear Phenomena* **154**, 111–137 (2001).
86. G. Popescu, A. Dogariu, and R. Rajagopalan, "Spatially resolved microrheology using localized coherence volumes," *Phys. Rev. E* **65**, 041504 (2002).
87. X. Zhou, X. Wu, H. Wang, C. Liu, and Z. Zhu, "Phase diagram of the Pluronic L64–H<sub>2</sub>O micellar system from mechanical spectroscopy," *Phys. Rev. E* **83**, 041801 (2011).
88. C. J. Kloxin and J. H. van Zanten, "Microviscoelasticity of adhesive hard sphere dispersions: Tracer particle microrheology of aqueous Pluronic L64 solutions," *The Journal of Chemical Physics* **131**, 134904–134904–10 (2009).
89. S. A. Tanner, S. Amin, C. J. Kloxin, and J. H. van Zanten, "Microviscoelasticity of soft repulsive sphere dispersions: Tracer particle microrheology of triblock copolymer micellar

- liquids and soft crystals," *The Journal of Chemical Physics* **134**, 174903–174903–10 (2011).
90. T. G. Mason, "Estimating the viscoelastic moduli of complex fluids using the generalized Stokes–Einstein equation," *Rheologica Acta* **39**, 371–378 (2000).
  91. A. M. Robertson, A. Sequeira, and M. V. Kameneva, "Hemorheology," in *Hemodynamical Flows: Modeling, Analysis And Simulation*, Oberwolfach Seminars (Birkhäuser, 2008), Vol. 37, pp. 63–120.
  92. A. K. Dunn, H. Bolay, M. A. Moskowitz, and D. A. Boas, "Dynamic Imaging of Cerebral Blood Flow Using Laser Speckle," *Journal of Cerebral Blood Flow & Metabolism* **21**, 195–201 (2001).
  93. P. A. Janmey and C. A. McCulloch, "Cell Mechanics: Integrating Cell Responses to Mechanical Stimuli," *Annual Review of Biomedical Engineering* **9**, 1–34 (2007).
  94. S. R. Heidemann and D. Wirtz, "Towards a regional approach to cell mechanics," *Trends in Cell Biology* **14**, 160–166 (2004).
  95. R. J. Petrie, A. D. Doyle, and K. M. Yamada, "Random versus directionally persistent cell migration," *Nature Reviews Molecular Cell Biology* **10**, 538–549 (2009).
  96. B. Pan, K. Qian, H. Xie, and A. Asundi, "Two-dimensional digital image correlation for in-plane displacement and strain measurement: a review," *Measurement Science and Technology* **20**, 062001 (2009).
  97. L. G. Wilson, V. A. Martinez, J. Schwarz-Linek, J. Tailleur, G. Bryant, P. N. Pusey, and W. C. K. Poon, "Differential Dynamic Microscopy of Bacterial Motility," *Phys. Rev. Lett.* **106**, 018101 (2011).

98. Z. Ahmed, S. Underwood, and R. A. Brown, "Low concentrations of fibrinogen increase cell migration speed on fibronectin/fibrinogen composite cables," *Cell Motility and the Cytoskeleton* **46**, 6–16 (2000).
99. C. L. Gatto, B. J. Walker, and S. Lambert, "Asymmetric ERM activation at the Schwann cell process tip is required in Axon-Associated motility," *Journal of Cellular Physiology* **210**, 122–132 (2007).
100. T. M. Svitkina, Y. A. Rovensky, A. D. Bershadsky, and J. M. Vasiliev, "Transverse pattern of microfilament bundles induced in epitheliocytes by cylindrical substrata," *J Cell Sci* **108**, 735–745 (1995).
101. E. M. Levina, L. V. Domnina, Y. A. Rovensky, and J. M. Vasiliev, "Cylindrical Substratum Induces Different Patterns of Actin Microfilament Bundles in Nontransformed and in ras-Transformed Epitheliocytes," *Experimental Cell Research* **229**, 159–165 (1996).
102. Y. Y. Biton and S. A. Safran, "The cellular response to curvature-induced stress," *Physical Biology* **6**, 046010 (2009).
103. J. A. Sanz-Herrera, P. Moreo, J. M. García-Aznar, and M. Doblaré, "On the effect of substrate curvature on cell mechanics," *Biomaterials* **30**, 6674–6686 (2009).
104. J. E. Bear, T. M. Svitkina, M. Krause, D. A. Schafer, J. J. Loureiro, G. A. Strasser, I. V. Maly, O. Y. Chaga, J. A. Cooper, G. G. Borisy, and F. B. Gertler, "Antagonism between Ena/VASP Proteins and Actin Filament Capping Regulates Fibroblast Motility," *Cell* **109**, 509–521 (2002).

105. L. Chen, M. Iijima, M. Tang, M. A. Landree, Y. E. Huang, Y. Xiong, P. A. Iglesias, and P. N. Devreotes, "PLA2 and PI3K/PTEN Pathways Act in Parallel to Mediate Chemotaxis," *Developmental Cell* **12**, 603–614 (2007).
106. Y. Kuga and A. Ishimaru, "Retroreflectance from a dense distribution of spherical particles," *Journal of the Optical Society of America A* **1**, 831–835 (1984).
107. S. Feng, C. Kane, P. A. Lee, and A. D. Stone, "Correlations and Fluctuations of Coherent Wave Transmission through Disordered Media," *Phys. Rev. Lett.* **61**, 834–837 (1988).
108. P. W. Anderson, "Absence of Diffusion in Certain Random Lattices," *Phys. Rev.* **109**, 1492–1505 (1958).
109. S. John, "Electromagnetic Absorption in a Disordered Medium near a Photon Mobility Edge," *Phys. Rev. Lett.* **53**, 2169–2172 (1984).
110. C. Toninelli, E. Vekris, G. A. Ozin, S. John, and D. S. Wiersma, "Exceptional Reduction of the Diffusion Constant in Partially Disordered Photonic Crystals," *Phys. Rev. Lett.* **101**, 123901 (2008).
111. E. Abrahams, P. W. Anderson, D. C. Licciardello, and T. V. Ramakrishnan, "Scaling Theory of Localization: Absence of Quantum Diffusion in Two Dimensions," *Phys. Rev. Lett.* **42**, 673–676 (1979).
112. V. Micó, J. Garcà, C. Ferreira, D. Sylman, and Z. Zalevsky, "Spatial information transmission using axial temporal coherence coding," *Optics Letters* **32**, 736–738 (2007).
113. D. Sylman, Z. Zalevsky, V. Micó, and J. García, "Super-resolved Imaging based upon spatial depolarization of light," *Journal of Physics: Conference Series* **206**, 012008 (2010).
114. E. Collett, *Polarized Light: Fundamentals and Applications*, 1st ed. (CRC Press, 1992).

115. E. Candès and J. Romberg, *11-Magic* (2005).
116. S. S. Chen, D. L. Donoho, and M. A. Saunders, "Atomic Decomposition by Basis Pursuit," *SIAM Review* **43**, 129–159 (2001).
117. S. G. Mallat, *A Wavelet Tour of Signal Processing: The Sparse Way* (Academic Press, 2009).
118. E. J. Candes, J. Romberg, and T. Tao, "Robust uncertainty principles: exact signal reconstruction from highly incomplete frequency information," *Information Theory, IEEE Transactions on* **52**, 489 – 509 (2006).
119. E. J. Candès, J. K. Romberg, and T. Tao, "Stable signal recovery from incomplete and inaccurate measurements," *Communications on Pure and Applied Mathematics* **59**, 1207–1223 (2006).
120. K. M. Douglass, J. Ellis, C. Toma, A. Mahalanobis, and A. Dogariu, "Expanding the field of view by polarization multiplexing," *Applied Optics* **49**, H40–H46 (2010).
121. J. R. Howse, R. A. L. Jones, A. J. Ryan, T. Gough, R. Vafabakhsh, and R. Golestanian, "Self-Motile Colloidal Particles: From Directed Propulsion to Random Walk," *Phys. Rev. Lett.* **99**, 048102 (2007).
122. A. Baskaran and M. C. Marchetti, "Statistical mechanics and hydrodynamics of bacterial suspensions," *Proc Natl Acad Sci U S A* **106**, 15567–15572 (2009).
123. Y. Gambin, R. Lopez-Esparza, M. Reffay, E. Sieracki, N. S. Gov, M. Genest, R. S. Hodges, and W. Urbach, "Lateral mobility of proteins in liquid membranes revisited," *Proc Natl Acad Sci U S A* **103**, 2098–2102 (2006).
124. B. I. Shraiman and E. D. Siggia, "Scalar turbulence," *Nature* **405**, 639–646 (2000).

125. G. L. Eyink and K. R. Sreenivasan, "Onsager and the theory of hydrodynamic turbulence," *Rev. Mod. Phys.* **78**, 87–135 (2006).
126. P. E. Cladis and P. Palffy-muhoray, *Spatio-temporal Patterns In Nonequilibrium Complex Systems* (Westview Press, 1995).
127. Y. L. Klimontovich and Y. L. Klimontovich, "Kinetic Theory of Active Media," in *Statistical Theory of Open Systems*, P. Blanchard, P. Busch, B. Coecke, D. Duerr, R. Frigg, C. A. Fuchs, G. Ghirardi, D. Giulini, G. Jaeger, C. Kiefer, K. Landsman, C. Maes, H. Nicolai, V. Petkov, A. Merwe, R. Verch, R. Werner, and C. Wüthrich, eds., *Fundamental Theories of Physics* (Springer Netherlands, 1995), Vol. 67, pp. 361–386.
128. I. S. Sohn, R. Rajagopalan, and A. Dogariu, "Spatially resolved microrheology through a liquid/liquid interface," *Journal of Colloid and Interface Science* **269**, 503–513 (2004).
129. E. W. Kamen and B. S. Heck, *Fundamentals of Signals and Systems Using the Web and MATLAB* (Pearson Prentice Hall, 2007).
130. M. A. Despósito, "Superdiffusion induced by a long-correlated external random force," *Phys. Rev. E* **84**, 061114 (2011).
131. P. M. Chaikin and T. C. Lubensky, *Principles of Condensed Matter Physics*, Reprint (Cambridge University Press, 2000).
132. D. V. Schroeder, *An Introduction to Thermal Physics*, 1st ed. (Addison Wesley, 1999).
133. K. M. Douglass, S. Sukhov, and A. Dogariu, "Superdiffusion in optically controlled active media," *Nat Photon* **6**, 834–837 (2012).



134. S. Skipetrov, S. Chesnokov, S. Zakharov, M. Kazaryan, and V. Shcheglov, "Ponderomotive action of light in the problem of multiple scattering of light in a randomly inhomogeneous medium," *JETP Letters* **67**, 635–639 (1998).
135. B. J. Ackerson, "Correlations for interacting Brownian particles," *The Journal of Chemical Physics* **64**, 242–246 (1976).
136. D. G. Grier and S. H. Behrens, "Interactions in Colloidal Suspensions," in *Electrostatic Effects in Soft Matter and Biophysics*, C. Holm, P. Kékicheff, and R. Podgornik, eds. (Springer Netherlands, 2001), pp. 87–116.
137. S. Sukhov, K. M. Douglass, and A. Dogariu, "Dipole-dipole interaction in random electromagnetic fields," arXiv:1304.6625 (2013).
138. M. Mazilu, A. Rudhall, E. M. Wright, and K. Dholakia, "An interacting dipole model to explore broadband transverse optical binding," *J. Phys.: Condens. Matter* **24**, 464117 (2012).
139. K. Dholakia and P. Zemánek, "Colloquium: Grippled by light: Optical binding," *Rev. Mod. Phys.* **82**, 1767–1791 (2010).
140. A. Jonáš and P. Zemánek, "Light at work: The use of optical forces for particle manipulation, sorting, and analysis," *ELECTROPHORESIS* **29**, 4813–4851 (2008).
141. F. Depasse and J.-M. Vigoureux, "Optical binding force between two Rayleigh particles," *J. Phys. D: Appl. Phys.* **27**, 914 (1994).
142. P. C. Chaumet and M. Nieto-Vesperinas, "Time-averaged total force on a dipolar sphere in an electromagnetic field," *Opt. Lett.* **25**, 1065–1067 (2000).

143. S. A. Tatarkova, A. E. Carruthers, and K. Dholakia, "One-Dimensional Optically Bound Arrays of Microscopic Particles," *Phys. Rev. Lett.* **89**, 283901 (2002).
144. D. Haefner, S. Sukhov, and A. Dogariu, "Conservative and Nonconservative Torques in Optical Binding," *Phys. Rev. Lett.* **103**, 173602 (2009).
145. J. Ellis and A. Dogariu, "Optical Polarimetry of Random Fields," *Phys. Rev. Lett.* **95**, 203905 (2005).
146. J. M. Ziman, *Models of Disorder: The Theoretical Physics of Homogeneously Disordered Systems* (Cambridge University Press, 1979).
147. R. T. Káradóttir and J. H. Stockley, "Deconstructing myelination: it all comes down to size," *Nature Methods* **9**, 883–884 (2012).
148. A. N. Rubinov, "Physical grounds for biological effect of laser radiation," *Journal of Physics D: Applied Physics* **36**, 2317–2330 (2003).
149. R. H. W. Funk, T. Monsees, and N. Ozkucur, "Electromagnetic effects - From cell biology to medicine," *Prog Histochem Cytochem* **43**, 177–264 (2009).
150. G. Bao and S. Suresh, "Cell and molecular mechanics of biological materials," *Nature Materials* **2**, 715–725 (2003).
151. J.-P. Hansen and I. R. McDonald, *Theory of Simple Liquids, Third Edition*, 3rd ed. (Academic Press, 2006).
152. J. W. Goodman, *Speckle Phenomena in Optics*, 1st ed. (Roberts and Company Publishers, 2006).
153. E. Barkai, Y. Garini, and R. Metzler, "Strange kinetics of single molecules in living cells," *Physics Today* **65**, 29–35 (2012).

154. C. Maggi, R. Di Leonardo, G. Ruocco, and J. C. Dyre, "Measurement of the Four-Point Susceptibility of an Out-of-Equilibrium Colloidal Solution of Nanoparticles Using Time-Resolved Light Scattering," *Phys. Rev. Lett.* **109**, 097401 (2012).
155. V. Viasnoff, F. Lequeux, and D. J. Pine, "Multispeckle diffusing-wave spectroscopy: A tool to study slow relaxation and time-dependent dynamics," *Review of Scientific Instruments* **73**, 2336–2344 (2002).
156. R. G. Larson, *The Structure and Rheology of Complex Fluids* (Oxford University Press, USA, 1998).
157. H. J. Klose, E. Volger, H. Brechtelsbauer, L. Heinich, and H. Schmid-Schönbein, "Microrheology and light transmission of blood," *Pflügers Archiv European Journal of Physiology* **333**, 126–139 (1972).
158. S. Yamada, D. Wirtz, and S. C. Kuo, "Mechanics of Living Cells Measured by Laser Tracking Microrheology," *Biophysical Journal* **78**, 1736–1747 (2000).
159. R. Huang, I. Chavez, K. M. Taute, B. Lukić, S. Jeney, M. G. Raizen, and E.-L. Florin, "Direct observation of the full transition from ballistic to diffusive Brownian motion in a liquid," *Nature Physics* **7**, 576–580 (2011).
160. D. A. Weitz, D. J. Pine, P. N. Pusey, and R. J. A. Tough, "Nondiffusive Brownian motion studied by diffusing-wave spectroscopy," *Phys. Rev. Lett.* **63**, 1747–1750 (1989).
161. R. G. Baraniuk, "Compressive Sensing [Lecture Notes]," *IEEE Signal Processing Magazine* **24**, 118–121 (2007).
162. M. Zibulevsky and B. A. Pearlmutter, "Blind Source Separation by Sparse Decomposition in a Signal Dictionary," *Neural Computation* **13**, 863–882 (2001).

163. M. Zibulevsky and M. Elad, "L1-L2 Optimization in Signal and Image Processing," *IEEE Signal Processing Magazine* **27**, 76–88 (2010).
164. S. Sukhov and A. Dogariu, "Negative Nonconservative Forces: Optical “Tractor Beams” for Arbitrary Objects," *Phys. Rev. Lett.* **107**, 203602 (2011).
165. K. Jaqaman, H. Kuwata, N. Touret, R. Collins, W. S. Trimble, G. Danuser, and S. Grinstein, "Cytoskeletal Control of CD36 Diffusion Promotes Its Receptor and Signaling Function," *Cell* **146**, 593–606 (2011).
166. J. Klafter, M. F. Shlesinger, and G. Zumofen, "Beyond Brownian Motion," *Physics Today* **49**, 33–39 (1996).
167. R. F. Fox, "Numerical Simulations of Stochastic Differential Equations," *J. Stat. Phys.* **54**, 1353–1366 (1989).
168. K. Lü and J.-D. Bao, "Numerical simulation of generalized Langevin equation with arbitrary correlated noise," *Phys. Rev. E* **72**, 067701 (2005).
169. B. Eckhardt, U. Dörr, U. Kuhl, and H.-J. Stöckmann, "Correlations of electromagnetic fields in chaotic cavities," *EPL* **46**, 134 (1999).
170. M. V. Berry, "Regular and irregular semiclassical wavefunctions," *J. Phys. A: Math. Gen.* **10**, 2083 (1977).